ISTANBUL TECHNICAL UNIVERSITY ★ GRADUATE SCHOOL

INVESTIGATION OF THE DAMPING EFFECTIVENESS OF PARTICLE DAMPER INTEGRATED STRUCTURES DESIGN PRODUCED BY LASER POWDER BED FUSION UNDER DIFFERENT BOUNDARY CONDITIONS

M.Sc. THESIS

Birol ÖZÇEVİK

Department of Mechanical Engineering

Machine Dynamics, Vibration and Acoustics Programme

MAY 2023

ISTANBUL TECHNICAL UNIVERSITY ★ GRADUATE SCHOOL

INVESTIGATION OF THE DAMPING EFFECTIVENESS OF PARTICLE DAMPER INTEGRATED STRUCTURES DESIGN PRODUCED BY LASER POWDER BED FUSION UNDER DIFFERENT BOUNDARY CONDITIONS

M.Sc. THESIS

Birol ÖZÇEVİK
(503191405)

Department of Mechanical Engineering

Machine Dynamics, Vibration and Acoustics Programme

Thesis Advisor: Assoc. Prof. Dr. Emrecan SÖYLEMEZ

MAY 2023

İSTANBUL TEKNİK ÜNİVERSİTESİ ★ LİSANSÜSTÜ EĞİTİM ENSTİTÜSÜ

LAZERLE TOZ YATAĞINDA FÜZYON İLE ÜRETİLMİŞ PARÇACIK SÖNÜMLEYİCİ ENTEGRELİ YAPILARIN TASARIMLARININ SÖNÜM ETKİNLİĞİNİN FARKLI SINIR KOŞULLARI ALTINDA İNCELENMESİ

YÜKSEK LİSANS TEZİ

Birol ÖZÇEVİK
(503191405)

Makina Mühendisliği Anabilim Dalı

Makina Dinamiği, Titreşim ve Akustik Programı

Tez Danışmanı: Doç. Dr. Emrecan SÖYLEMEZ

MAYIS 2023

Birol ÖZÇEVİK, a M.Sc. student of İTU Graduate School with student ID 503191405, successfully defended the thesis entitled "INVESTIGATION OF THE DAMPING EFFECTIVENESS OF PARTICLE DAMPER INTEGRATED STRUCTURES DESIGN PRODUCED BY LASER POWDER BED FUSION UNDER DIFFERENT BOUNDARY CONDITIONS", which he prepared after fulfilling the requirements specified in the associated legislations, before the jury whose signatures are below.

Thesis Advisor : **Assoc. Prof. Dr. Emrecan SÖYLEMEZ** ....
İstanbul Technical University

Jury Members : **Prof. Dr. İlker Murat KOÇ** ....
Istanbul Technical University

Assoc. Prof. Dr. Bekir Bediz ....
Sabanci University

Date of Submission : 27 April 2023
Date of Defense : 24 May 2023

To my family,

FOREWORD

This project would not have been possible without the support and contributions of several individuals, whose dedication and expertise have been invaluable. To begin with, I would like to thank my thesis advisor, Assoc. Prof. Dr. Emrecan SÖYLEMEZ, whose guidance and mentorship have been instrumental throughout this journey. His expertise and feedbacks have shaped every aspect of this thesis.

I also extend my thanks to Assoc. Prof. Dr. Bekir BEDİZ, whose guidance and advices make all the journey easy. His constructive feedback and advice have helped me to refine my research questions, analyze my data, and develop my arguments. His insights and feedback on the technical aspects of my work have been invaluable, and his contributions have helped me to produce a more rigorous and well-supported thesis.

In addition, I would like to acknowledge my dear colleague Dr. Uğur ŞİMŞEK, whose expertise and contribution has been indispensable to this project. It would have been impossible for me to complete this project without his contribution, guidance and support throughout the process.

Finally, I am grateful for the unrelenting support and encouragement of my dear family and friends, whose unwavering support have sustained me throughout this journey. Their love and encouragement have been a constant reminder of the importance of perseverance and dedication in achieving one's goals.

May 2023

Birol ÖZÇEVİK
Mechanical Engineer

TABLE OF CONTENTS

Page

ABBREVIATIONS

3D	: 3 Dimensional
AM	: Additive Manufacturing
CAD	: Computer Aided Design
DEM	: Discrete Element Method
DOE	: Design of Experiments
DOF	: Degree of Freedom
EDM	: Electrical Discharge Machine
FEA	: Finite Element Analysis
FEM	: Finite Element Method
FFT	: Fast Fourier Transform
FRF	: Frequency Response Function
ID	: Impact Damper
IN718	: Inconel 718
LPBF	: Laser Powder Bed Fusion
MDOF	: Multi Degree Of Freedom
MUID	: Multi Unit Impact Damper
MUPD	: Multi Unit Particle Damper
PD	: Particle Damper
PS	: Partikül Sönümleyici
RFP	: Rational Fraction Polynomial
RMS	: Root Mean Square
RSS	: Root Sum Square
TMD	: Tuned Mass Damper

SYMBOLS

cm	: Cantimeter
g	: Gram
Hz	: Hertz
m	: Meter
mm	: Milimeter
N	: Newton
ω	: Frequency

LIST OF TABLES

Page

LIST OF FIGURES

Page

INVESTIGATION OF THE DAMPING EFFECTIVENESS OF PARTICLE DAMPER INTEGRATED STRUCTURES DESIGN PRODUCED BY LASER POWDER BED FUSION UNDER DIFFERENT BOUNDARY CONDITIONS

SUMMARY

Particle damper (PD) technology has been increasingly adopted as a passive damping mechanism in structures to minimize vibrations and improve their performance. This technology is particularly advantageous due to its design simplicity, low cost, and applicability in harsh conditions, making it an attractive alternative to traditional damping techniques.

The production of structures with integrated PDs using additive manufacturing, particularly the Laser Powder Bed Fusion (LPBF) process, has become increasingly studied in recent times. This approach eliminates the need for external dampers to be implemented into the structure, simplifying the design process and reducing costs. However, in order to fully utilize the potential of PDs, a deeper understanding of their dynamic behavior is required.

To this end, a study is conducted to investigate the impacts of integrated PDs on the dynamic behavior of additively manufactured structures. The study examined 16 different cases of integrated PDs with different sizes, numbers, and positions on the structure. For example, PDs with different total volumes were designed and located at various positions in the structure to understand the size and position impact on the dynamic behavior at the first and second modes of the structure.

Hammer impact tests were performed on the additively manufactured samples to calculate the frequency response functions (FRFs). The modal parameters such as the natural frequency and damping ratio were obtained using the rational fraction polynomial (RFP) method. According to the findings, the damping performance of the parts was improved up to 10 times by using body-integrated PDs compared to the fully fused specimen.

It was also observed that the effectiveness of body-integrated PDs depend significantly on the volume and spatial location. For instance, damping was generally increased when the volume fraction was increased. This increase in volume fraction also reduced the total weight of the specimens by up to 60 g. Moreover, the damping performance significantly increased for a specific mode if the PDs were located around the maximum displacement regions.

Another design group was created to investigate the boundary conditions. The samples in this group were tested with both free-free and fixed-free boundary conditions. According to the results, although higher results were obtained for the fixed-free boundary conditions for the first mode, it was revealed that there are many parameters to be investigated such as mode shapes and system dampings.

The findings of this study are of great significance to the manufacturing industry as they provide insights into the potential benefits of using integrated PDs in structures. With the ability to reduce vibrations and improve performance, structures

incorporating PDs can be designed to fulfill the particular requirements of various industries such as aerospace, automotive, and civil engineering.

Additionally, the study highlights the potential of additive manufacturing to produce structures with integrated PDs. With the flexibility of the powder bed fusion process, designers can easily incorporate PDs into their designs, without the need for external dampers. This approach not only simplifies the design process but also reduces costs, making it an attractive alternative to traditional damping techniques.

It is worth noting that while the results of this study are promising, additional researches are required to fully understand the dynamic behavior of structures with integrated PDs. Future studies should focus on optimizing the size, shape, and location of PDs to achieve maximum damping performance. Moreover, research is required to investigate the effectiveness of integrated PDs on other modes of the structure, as well as on structures subjected to different loads and operating conditions.

In conclusion, the use of particle damper technology in structures has the potential to improve their performance and reduce vibrations. By incorporating PDs into structures using additive manufacturing, designers can achieve greater design flexibility and reduce costs. However, further research is needed to fully realize the potential of this technology and optimize the design of structures with integrated PDs.

LAZERLE TOZ YATAĞINDA FÜZYON İLE ÜRETİLMİŞ PARÇACIK SÖNÜMLEYİCİ ENTEGRELİ YAPILARIN TASARIMLARININ SÖNÜM ETKİNLİĞİNİN FARKLI SINIR KOŞULLARI ALTINDA İNCELENMESİ

ÖZET

Parçacık sönümleyici teknolojisi, titreşimleri en aza indirmek ve yapı performanslarını artırmak için kullanılan ve giderek yaygınlaşan bir sönümleme mekanizmasıdır. Temel çalışma prensibi, parçacıkların çıkamayacakları bir hacime hapsedildikten sonra entegre edildikleri yapıdan veya ortamdan gelen dinamik yüklerin etkisiyle oluşacak hareketleri, parçacıkların birbiri arasında veya içinde bulundukları hacmin limitleyici unsurları ile parçacıklar arasında oluşan etkileşimle kinetik enerjinin soğurulup, başta sürtünme kaynaklı ısı enerjisi olmak üzere diğer enerji türlerine dönüştürülmesi şeklindedir. Dışarıdan bir güç kaynağına ihtiyaç duymadığından pasif çalışma yöntemine sahip bu teknoloji, tasarım basitliği, düşük maliyeti ve zorlu koşullarda uygulanabilirliği gibi nedenlerle geleneksel sönümleme tekniklerine üstünlük kurabilmekte ve bu da onu geleneksel sönümleme tekniklerine çekici bir alternatif haline getirmektedir.

Son yıllarda, entegre parçacık sönümleyicilere sahip yapılar üretmek için eklemeli imalatın, özellikle de toz yatağı füzyon prosesinin kullanımına artan bir ilgi vardır. Bunun sebebi, ek bir üretim sürecine ihtiyaç duyulmaksızın, yalnız doğru tasarım sürecini işleterek gövdeye entegre parçacık sönümleyicilerin olduğu yapıların üretilebilme imkanıdır. Söz konusu toz yataklı eklemeli imalat yöntemlerinde hâlihazırda üretimde kullanılmak üzere bulunan tozun sönümleyicilik işlevini yerine getirecek olan parçacıklar olarak da kullanılabilmesi bu metotların parçacık sönümleyici (PS) entegreli yapı üretiminde avantajlı kılmaktadır. Bu yaklaşım, yapıya uygulanacak harici damperlere olan ihtiyacı ortadan kaldırarak tasarım sürecini ve tasarlanan yapıları basitleştirir ve maliyetleri düşürür. Ayrıca gövdeye entegre parçacık sönümleyicilerin kullanımı, uygun bir tasarımla ek kütleye ihtiyaç bırakmayabileceğinden havacılık gibi ağırlığın kritik olduğu endüstrilerde avantaj sağlama potansiyeline sahiptir. Bununla birlikte, parçacık sönümleyicilerin belirtilen potansiyelinden tam olarak yararlanmak için dinamik davranışlarının daha derinden anlaşılması gerekir.

Bu çalışma, toz yataklı lazer füzyon yöntemi ile üretilmiş yapıların dinamik davranışna, yapı gövdesine entegre parçacık sönümleyicilerin tasarım parametrelerinin etkilerini araştırmak için yapılmıştır. Bu maksatla çalışmada yapı üzerinde farklı boyut, sayı ve konumlara sahip gövdeye entegre parçacık sönümleyiciler içeren 16 farklı numune üzerinde inceleme yapılmıştır. Bu numuneler parça içinde belli hacimlerde kaynaşmamış tozlar bırakılarak tasarlanmış ve üretilmiştir. Ayrıca bir adet tamamen ergimiş ve birleşmiş tozlardan oluşan (PS içermeyen) numune de karşılaştırmalı analizler için imal edilmiştir. Söz konusu yapıların ilk iki modu ve bu modlardaki sönüm davranışları gözlemlenmiştir. Bu doğrultuda boyut ve konumun yapının birinci ve ikinci modlarındaki dinamik davranış üzerindeki etkisini anlamak için farklı toplam hacimlere sahip parçacık sönümleyiciler

tasarlanmış ve yapının çeşitli konumlarına yerleştirilmiştir. Ana yapının boyutları sabit tutulurken parçacık sönümleyiciler için konum, boyut ve aynı hacim için gövdeye entegre PS sayısı değişken parametreler olarak belirlenip tasarımlar yapılmış ve ilk iki moddaki sönümleme etkileri kaydedilmiştir.

Sönümleme etkileri, sönüm oranı ile gösterilmiştir ve sönüm oranları frekans yanıt fonksiyonları (FRF) çıkarılarak her iki mod için hesaplanmıştır. FRF'ler, eklemeli olarak üretilmiş numuneler üzerinde yapılan modal testler sonucunda elde edilmiştir. Test yöntemi olarak çekiç testi seçilmiş ve serbest – serbest sınır koşullarıyla test gerçekleştirilmiştir. Bu sınır koşullarını sağlayabilmek için numuneler zemin tepkisini en aza indirebilmek için iki süngerin üzerine ve olabilecek en küçük alan (bu test için yaklaşık 6 mm^2) süngerlere temas ettirilecek surette konumlandırılmıştır. İvmeölçer numunelerin zemine bakan yüzünde ve bu yüzeyin orta noktasında konumlandırılmış ve kablo hareketinden etkilenmemesi için kablo belirli bir konumdan sonra sabitlenmiştir. Numunelerin üstte kalan yüzeylerine 12 noktadan çekiç ile en az 5'er kez olacak şekilde vuruş yapılmış ve her bir nokta için FRF'ler elde edilmiştir. Bu FRF'lerin tümünden doğal frekanslar elde edilmiş ve rasyonel kesir polinomu (RFP) yöntemi kullanılarak sönüm oranları hesaplanmıştır. Bu verilerin ortalaması alınarak nihai sonuç elde edilmiştir. Sonuçlar, PS içeren numunelerin sönümleme performansının, tamamen kaynaşmış (PS içermeyen) numuneye kıyasla 10 kata kadar artırıldığını göstermiştir.

Numunelere entegre parçacık sönümleyicilerin etkinliğinin, hacim ve uzamsal konuma önemli ölçüde bağlı olduğu gözlemlenmiştir. Örneğin, hacim fraksiyonu (PS hacminin yapının toplam dış hacmine oranı) artırıldığında sönümleme genellikle artırılmıştır. Kaynaşmamış tozların yoğunluğu, kaynaşmış olanlara kıyasla çok daha düşük olduğundan, hacim fraksiyonundaki bu artış aynı zamanda numunelerin toplam kütlelerinde 60 g'a varan azalmalara da neden olmuştur. Ayrıca, parçacık sönümleyiciler maksimum yer değiştirme bölgelerinin etrafına yerleştirildiyse, belirli bir mod için sönümleme performansında önemli ölçüde artış gözlemlenmiştir. Bu numunelerin tamamında serbest – serbest sınır koşulları için ilk mod eğilme mod şekline, ikinci mod ise burulma mod şekline sahiptir. İlk modda maksimum yer değiştirme noktası yine aynı sınır koşulları için parçanın orta bölgeleri iken ikinci modda uçların yer değiştirmesi daha fazladır. Dolayısıyla bu durum her bir mod şekli için farklılık gösterebilmektedir ve ilk modda merkeze, ikinci modda ise uçlara yerleştirilmiş parçacık sönümleyicilerin daha etkin çalıştıkları gözlemlenmiştir.

Bir diğer tasarım grubu da sınır koşullarını incelemek adına oluşturulmuştur. Bu gruptaki numuneler hem serbest – serbest, hem de bağlı – serbest sınır koşulları ile test edilmiştir. Sonuçlara göre bağlı – serbest sınır koşullarında ilk mod için daha yüksek sonuçlar gelse de mod şekilleri, sistem sönümleri gibi incelenmesi gereken pek çok parametre olduğu ortaya konmuştur.

Bu çalışmanın bulguları, yapılarda entegre parçacık sönümleyicilerin kullanılmasının potansiyel faydalarına ilişkin içgörü sağladığı için çeşitli endüstri kolları için büyük önem taşımaktadır. Titreşimleri azaltma ve yapı performansını artırma vaadiyle, parçacık sönümleyicileri içeren yapılar, havacılık, otomotiv ve inşaat mühendisliği gibi çeşitli endüstrilerin özel ihtiyaçlarını karşılamak üzere tasarlanabilir sonucuna varılmaktadır. Ek olarak, çalışma, eklemeli imalatın entegre parçacık sönümleyicilere sahip yapılar üretme potansiyelini vurgulamaktadır. Toz yatağı füzyon prosesinin esnekliği ile tasarımcılar, harici sönümleyicilere ihtiyaç duyulmayan, parçacık sönümleyicilerin yapı tasarımlarına kolayca dahil edildiği dizaynlar çıkartabilirler.

Bu yaklaşım sadece tasarım sürecini basitleştirmekle kalmaz, aynı zamanda maliyetleri düşürür ve parçacık sönümleyicileri geleneksel sönümleme tekniklerine kıyasla çekici bir alternatif haline getirir.

Her ne kadar parçacık sönümleyicilerin kullanımı eskiden beri var olsa da, gövdeye entegre parçacık sönümleyicilerin kullanımı görece yeni bir konudur. Gerek bu çalışmanın, gerekse bu alanda yapılan diğer çalışmaların sonuçları umut verici olsa da, yapıya entegre parçacık sönümleyicilere sahip yapıların dinamik davranışını kapsamlıca anlamak için daha fazla çalışmaya gereksinim olduğu belirtilmelidir. Gelecekteki çalışmalar, maksimum sönümleme performansı elde etmek için parçacık söümleyicilerin boyutunu, şeklini ve konumunu optimize etmeye odaklanmalıdır. Bu çalışmaların uygun optimizasyon metotları geliştirmek üzere bu çalışmada olduğu gibi basit numuneler üzerinden ilerletilmesi gerektiği gibi karmaşık geometriye sahip parçalar üzerinde de doğrulamaların yapılması gerekmektedir. Ayrıca, yapıya entegre parçacık sönümleyicilerin yapının çeşitli modları üzerindeki etkilerinin yanı sıra farklı yüklere ve çalışma koşullarına maruz kalan yapılar üzerindeki etkilerini araştırmak için araştırmalara ihtiyaç vardır. Karmaşık geometrili parçaların mod şekilleri bilinen geometrilere göre daha kompleks olduğundan, doğru optimizasyonla kritik modlarda etkin çalışacak sönümleyicilerin entegrasyonu oldukça mühimdir.

Sonuç olarak, yapılarda parçacık sönümleyici teknolojisinin kullanılması, performanslarını iyileştirme ve titreşimleri azaltma potansiyeline sahiptir. Ayrıca ek ağırlıklardan kurtulma ve hatta kütlede azalma vaad etmektedir. Tasarımcılar, parçacık sönümleyicileri eklemeli imalatla üretilecek yapılara uygun biçimde dahil ederek daha etkin bir tasarım elde edebilir ve maliyetleri azaltabilir. Ancak, bu teknolojinin potansiyelini tam olarak gerçeklemek ve yapıya entegre parçacık sönümleyicilere sahip yapıların tasarımını optimize etmek için çalışılması gereken pek çok konu mevcuttur.

1. INTRODUCTION

Vibration is a mechanical oscillation that plays a significant role in human life. The process of hearing involves the vibration of the eardrum and related mechanisms, while speech is produced by the vibration of the tongue and vocal cords. This is because the creation of sound and the perception of sound through hearing both rely on the concept of vibration. It is also utilized in construction to remove voids in concrete or to drill through a hard surface with a percussion drill. Many musical instruments, particularly those with strings, require vibration to produce their intended sound. However, vibration can also be an unwanted and destructive phenomenon for numerous mechanical systems. Vibrations in an aircraft fuselage can lead to high-cycle fatigue and consequent defects such as cracks. Vibrations caused by earthquakes could be the reason to failures in buildings, and mechanical connections can also loosen due to vibration [1, 2].

In summary, vibration is a phenomenon that can impact the structural integrity of designs, and even the characteristics of the vibration itself can be a deciding factor. While there are scenarios where vibration is advantageous as mentioned above, minimizing vibration and its harmful effects is typically a priority. Controlling and conducting tests and analyses for vibration, whether it is a desirable state for a system or not, is crucial in terms of engineering. To control and reduce the negative effects of vibration, dampers are used. Examples of the traditional dampers are given in following pharagraphs. [1–3].

Viscous dampers use a silicone-based fluid in a cylinder to absorb energy from the piston – fluid interaction. This damper type can reduce vibrations induced by strong wind and earthquakes. However, the temperature range for their usage is limited to -40 to 70°C due to changes in viscosity. Viscoelastic dampers, on the other hand, stretch an elastomer along with metal components to dissipate mechanical energy by transforming it into heat. The effectiveness of this type of damper is influenced by various factors, such as ambient temperature and loading frequency. Friction dampers consist of multiple steel plates that move against each other and dissipate energy through friction between these surfaces. Tuned Mass Dampers (TMDs) are mechanical devices that are installed at certain locations within a structure as a passive control system to minimize the magnitude of vibrations generated by powerful lateral forces. Yielding dampers absorb energy by allowing yielding or plastic deformation to occur in a specific region. Finally, magnetic dampers use magnetic fields to generate damping forces and help reduce vibration in structures. They are highly responsive and effective in controlling vibration, with using electromagnetic induction [3].

Moreover, the choice of the appropriate damper type is depend on the modal characteristics and the damping requirements of the specific system. Viscous dampers, for example, are commonly used in buildings and bridges to reduce wind-induced vibrations, while yielding dampers are preferred in seismic regions to absorb the energy of earthquake-induced vibrations. Magnetic dampers, on the other hand, are effective in controlling vibrations in high-speed machinery and equipment. Regardless of the type of damper used, their main purpose is to dissipate the energy of vibrations and reduce their amplitude to acceptable levels [3].

In this study, another type of damper was investigated which is particle damper (PD). In recent years, there has been a growing interest in PD technology as an effective passive damping mechanism to reduce vibrations in structures. They work by absorbing energy generated by the interaction of particle-particle and particle-cell walls, resulting from friction and collisions. This energy absorption leads to a reduction in the amplitude of vibrations and improves the dynamic response.

Particle dampers (PDs) provide numerous benefits such as simple design, low cost [4–7], long component life [4], excellent performance at high temperatures and oil-contaminated conditions [5, 8–11], and broadband damping [12–16] compared to their conventional counterparts. Due to these advantages, PDs are used in diverse fields such as in medical, energy, automotive, and aerospace industries [17].

To utilize the full potential of PDs, it is important to understand their dynamic behavior. The performance of PDs is influenced by various factors, including the size, number, and position of them. Researchers have conducted numerous studies to understand the impact of these factors on the damping performance of PDs.

Particle dampers have found extensive application in a variety of fields to mitigate vibrations. For instance, they have been utilized to minimize vibrations in cutting tools, engine turbine systems of space shuttles, and antenna structures [14, 18, 19]. In addition to these applications, particle damping technology has demonstrated its effectiveness in controlling vibrations and noise in engineering [6, 20–24]. Furthermore, particle dampers have been explored for the purpose of reducing vibrations in medical instruments [25]. Despite the excellent effectiveness, the understanding of vibration reduction mechanism of PDs has been limited because of their highly nonlinear behaviour [26, 27]. As a result, a wide and optimal design methods for PDs is yet to be developed [16]. However, ongoing research has been conducted to better understand the fundamentals of particle damping technology and to build up advanced design methodologies to optimize its performance.

1.1 Types of Particle Dampers

Traditional PDs can be classified into four main types based on the number of cavities and particles within them. Figure 1.1 demonstrates types of the dampers which are the impact damper (ID), multi-unit impact damper (MUID), particle damper (PD), and multi-unit particle damper (MUPD) [5].

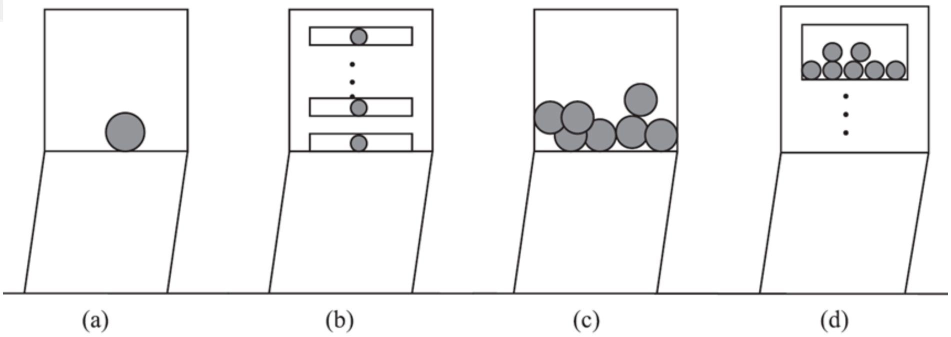

Figure 1.1 : The four types of traditional PDs are represented in a diagram as: (a) ID, (b) MUID, (c) PD, and (d) MUPD [5].

A single cavity damper type, ID, designed to absorb and dissipate energy generated by impacts. The multi-unit impact damper, on the other hand, comprises multiple impact dampers can be constructed in series or parallel to increase the damping effectiveness of them. [28–30]. The particle damper, which is also a single-unit damper, utilizes particles - such as steel balls or sand - to dampen vibrations. When subjected to vibration, the particles move within the cavities and cause frictional forces, which convert the vibration energy into heat. The multi-unit particle damper is similar to the MUID in that it consists of multiple particle dampers arranged in series or parallel to increase damping capacity [13]. The studies conducted on the mentioned types of PDs are exemplified in the following paragraphs.

Lieber and Jensen studied on the working principles of an acceleration damper, which is a type of ID consisting of a particle in a cavity [30]. One of the foundations of this study is that the efectiveness of the PD is related with the degree of freedom of the particle within its cavity. The theory provides formulas for more efficient design of the damper for particular applications and procedures [30]. They also validated their theory with experiments, and found that friction forces were detrimental to the damper's efficiency. The paper also discusses the potential applications of the IDs, such as fatigue, helicopter and aircraft vibration control. Finally, a methodology is proposed to calculate the impact of the damper [30].

Nayeri et al. studied the intricacies of enhancing the efficiency of particle dampers, which are affected by internal friction, momentum transfer, and nonlinearity [29]. Their research outlines feasible design methods to provide the best efficiency on damping of MUIDs under random excitation, with simulations conducted using up to 100 dampers [29]. The results indicate that MUIDs can optimize their performance by achieving a balance between reducing high vibrations over a wide range and decreasing attenuation to a certain degree across a broader range. The research employs simulations that mimic common earthquake ground motions, featuring both stationary and nonstationary excitations, to illustrate its methodology [29].

Papalou and Masri studied to investigate the performance of PDs in controlling vibrations in structures subjected to random wide-band excitation. It considers system parameters like mass, particle and cavity sizes, intensity, and excitation direction [13]. The study shows that well-designed PDs can succesfully decrease dynamic response of structures. By replacing the solid particle with numerous particles of equivalent mass, noise levels can be successfully reduced, and sensitivity to cavity size and excitation amplitude can be decreased [13]. The study discovered that smaller particle sizes decrease the impact of cavity size and excitation intensity, leading to an expansion of the optimal design, although response levels may be slightly higher. The study provides an analytical approach that utilizes the idea of an equivalent single particle damper which estimates the response of a primary structure subjected to random excitation. This solution assumes that the structure is equipped with a particle damper functioning within its optimal range. Experimental measurements are presented to validate the analytical solution [13].

Saeki conducted a study on the effectiveness of a MUPD in a system that vibrates horizontally [8]. The damper removes vibratory energy due to interaction of the particles. The study presented an analytical solution that accurately estimates the root-mean-square (RMS) response of the main system using the discrete element method (DEM) [8]. The performance of the PD was found to depend on the volume fraction and the number of PDs. Additionally, the highest RMS results of the main system's amplitude at the optial cavity radius were comparable for all the system parameters examined [8].

1.2 Additive Manufacturing of Particle Dampers

The ability to customize particle dampers (PDs) for specific applications is greatly expanded by the design freedom offered through additive manufacturing (AM) [12]. The design flexibility of AM can also be used to create PDs with multiple cavities of different sizes and shapes, which can improve their damping performance by increasing the amount of particle movement and energy dissipation [12]. The laser powder bed fusion (LPBF) process is the preferred AM process for PD functional integration because it allows leaving the powder particles inside the cavities without sintering during the part build as opposed to electron beam melting or binder jetting processes [12]. Furthermore, LPBF provides vast design flexibility by adjusting the size/geometry [12] and location [31] of unfused powder (referred to as cavity throughout the script). This flexibility is important for the application of PDs which have been already utilized in various fields such as civil engineering, the automotive industry, machine tools, helicopter blades, wind turbines, *etc.* for a long time [32]. Although the design flexibility of PDs provided by LPBF was a milestone for these applications, the impact of PD on the dynamic behavior of these structures requires to be fully comprehended to utilize its full potential [33, 34]. Overall, the combination of AM and advanced materials offers a range of possibilities for the development of PDs with customized damping performance for various applications. Ongoing research in this area is expected to lead to the creation of new and innovative PD designs that can significantly improve the performance and reliability of structures in a wide range of industries. The following sub-section provide detailed information on LPBF-manufactured structures that contain PDs, including insights from relevant studies.

1.2.1 Laser powder bed fusion

The LPBF process is a type of AM that has transformed the manufacturing industry by enabling the creation of complex components at a lower cost and with less labor. It allows for the production of complex shapes without the need for tooling or conventional manufacturing methods. It is crucial to comprehend the connection between operational parameters and the final properties of the component in the LPBF process. This technique involves spreading a layer of powder onto a bed, then utilizing high-intensity laser energy to selectively melt and fuse pre-determined regions of the powder, layer by layer, in accordance with CAD geometry. The term LPBF that describes the use of a laser energy as a heat source, the melting of powder, and the selective application of heat to specific parts of the powder bed as shown in Fig. 1.2 [35, 36].

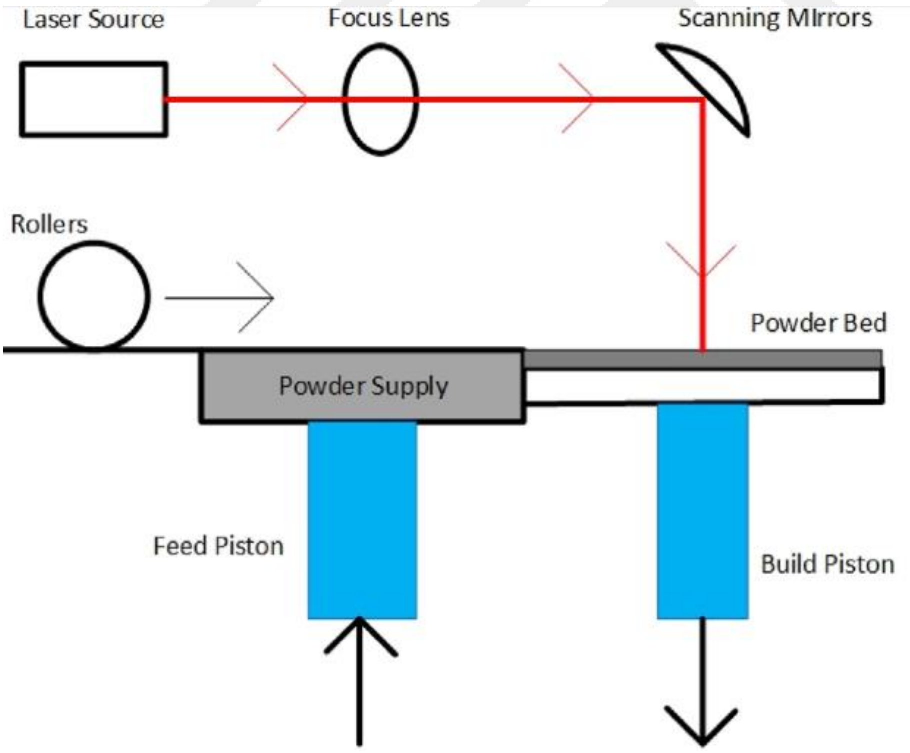

Figure 1.2 : The basic operational structure of a typical LPBF machine [35].

For most of the cases, powder discharge is a concern for design for LPBF. Wang and Xia discussed the challenges of closed voids in powder-based 3D printing and proposes a solution using topology optimization to create cavities/spaces automatically for powder discharge [37]. The primary stages of the suggested approach are optimization and extraction of topology, as well as cavity creation. The effectiveness of the created cavities is verified via experiments, and six standard structures with numerous enclosed empty spaces are examined to understand the usefulness of the approach [37]. On the other hand, this method brings advantage to produce PDs that are integrated with the main body. The reason for this is that the manufacturing technique permits the deliberate retention of existing powders for manufacturing in the body through proper design, which allows for the manufacturing of PDs.

Ehlers et al. utilized LPBF to manufacture specimens composed of AlSi10Mg in the shape of a beam. They evaluated the PD performance using curves generated for different specimens and design configurations [12]. Their study yielded valuable insights into the potential of particle damping for reducing unwanted vibrations in dynamic systems. The results demonstrated that particle-filled cavities can significantly increase damping, up to 20 times higher than fully-fused components[12]. The width and height of the cavity were found to have a greater impact on damping when compared the length. The researchers tested both horizontally and vertically manufactured specimens, and found that the vertical specimens had a higher packing density. Another finding from the research is the impact of force on damping curves, which take the shape of a hyperbola. These curves remain approximately constant for impacts over 100 N. In addition, the study found that frequency is another important factor affecting particle damping, and fully-fused specimens exhibit a hyperbolic damping curve when the impact frequency exceeds the natural frequency [12]. They suggest several areas for further research, including optimizing the location of specimens for free-free boundary conditions on the foam, subjecting the beams to heat treatment, and evaluating the longtime impact of PDs produced by AM. Additionally, the development of a surrogate model for particle damping could provide a better understanding of its potential applications [12]. The insights gained from this study may have implications for reducing unwanted vibrations in various fields, from vehicle engineering to civil engineering and space travel. Overall, the study contributes to a deeper understanding of particle damping and its potential applications for reducing unwanted vibrations in dynamic systems [12]. In another similar study by Ehlers and Lachmayer, they investigated the design of particle dampers produced by LPBF, including the effects of printing direction and the necessary design considerations [38].

In another study conducted by Ehlers et al. too, a method was developed for designing effect optimized components with high stiffness and high damping using particle damping [33]. This method was applied to a motorcycle triple clamp, which was topology optimized and extended by particle damping for vibration reduction. LPBF was utilized to integrate particle-filled cavities directly into the component [33]. Experimental studies indicated that particle damping can increase by a factor of more than 20. Simulative evaluations demonstrated the static strength of the material, and an expected damping increase of 3-5 times for several bending modes. The developed method provides a solution to the challenge of conflicting objectives faced by engineers when designing dynamically loaded structural components with unwanted vibrations [33]. Another prominent research group in this field is the group led by Emuakpor et al [31, 39–43]. Beam components with special internal designs that manufactured using LPBF can improve system damping [39]. They tested four Inconel 718 beams with unfused powder pockets using a shaker setup and found that these beams demonstrated up to 10 times more damping capability than a solid baseline beam [39]. Goldin and colleagues utilized LPBF to add unfused powder pockets into the design of a compressor blade to suppress vibrations and enhance robustness to high cycle fatigue [40]. The study employed various testing methods, such as computed tomography scans and structured light scan, to examine the dynamic behavior of the blade. The results showed that the blade had comparable endurance and damping capabilities to previous studies, and the remaining powder in the cavities did not have any significant impact on the measured mode shapes [40].

1.3 Numerical Modeling

Numerical modeling is utilized to understand the dynamic behavior of particle dampers. However, one of the main challenges is the nonlinearity in terms of dynamic behavior of PDs, which can make it difficult to accurately predict the effect of the dampers on the dynamic behavior of the structures they are applied to [44]. Nonlinear behavior can arise from various factors, such as changes in stiffness or fluctuations in particle packing density, which can make it challenging to model accurately [5, 44]. There are various approaches to address the issue.

1.3.1 Discrete element method

The discrete element method (DEM) is a computational approach used to study the mechanical behavior of discrete bodies. In order to model the movements of discrete bodies, DEM is utilized. This technique involves dividing the bodies into multiple discrete elements, which are governed by local interaction laws and Newton's equation of motion to describe their movements. This method is based on the assumption that allows for the forces impacted on each particle to be specified only by its interaction with neighbors at all times. As a result, this technique enables a detailed modeling of the behavior of whole system. Therefore, the forces acting on any particle at any given time are solely specified by its interactions with its adjacent particles [5]. For example, Quin at al. modeled the interaction between elements using spring forces in the linear elastic contact model which represented in Fig. 1.3 [45].

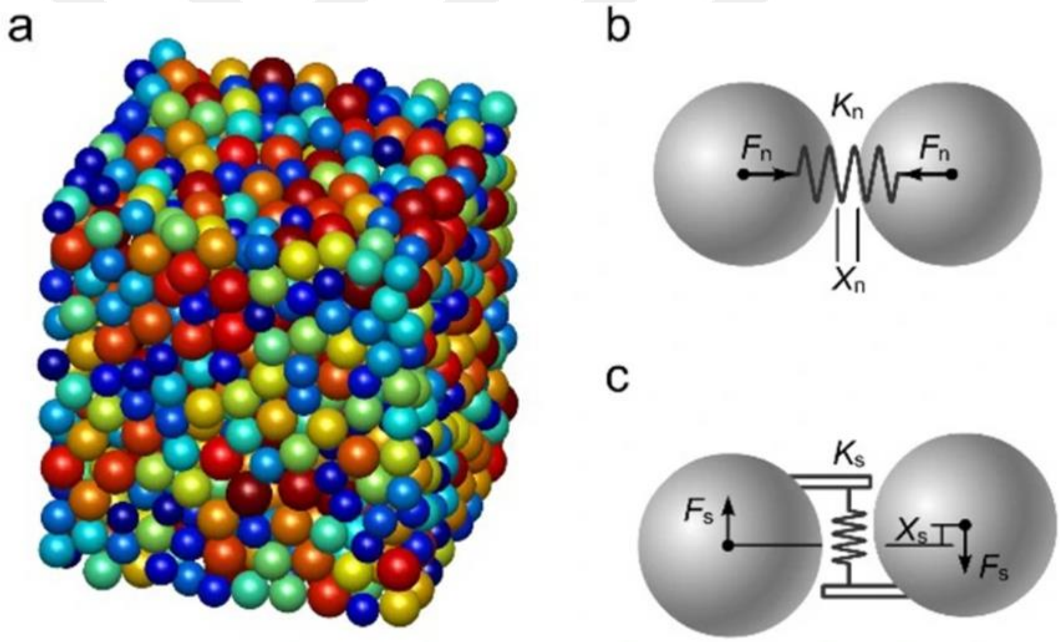

Figure 1.3 : The figure shows three components of a DEM model: (a) the model itself, (b) the normal spring force, and (c) the shear spring force [45].

In the figure above, rocks and soil are depicted as a collection of bonded components with distinct mechanical properties, represented using DEM [45]. The contact model between these elements was linear elastic, which considers the interaction to be driven by spring forces. In here, the normal force is represented with F_n and the normal deflection showed with X_n within two components are represented by a normal spring [45].

$$F_n = \begin{cases} K_n X_n, X_n < X_b \; intact\ bond\ (a) \\ K_n X_n, X_n < 0 \; broken\ bond\ (b) \\ 0, X_n \geq 0 \; broken\ bond\ (c) \end{cases} \tag{1.1}$$

X_b is required displacement to break bonds and K_n is normall stiffness in this equation [45]. X_n signifies the distance of displacement from a specified reference point, and it is utilized to determine the force acting between the individual elements. If the X_n exceeds X_b, the normal spring breaks, resulting in a tensile force of zero. there would be no F_n between components when the X_n is equal to or higher than zero if normal spring would break. However, even when the elements return to a compressive state, the force of repulsion remains active [45]. The simulation of the shear force (F_s) and shear deformation (X_s) within two components is accomplished using a tangential spring. The shear stiffness, denoted by K_s, and the relative displacement in shear, X_s, are both included in the equation below [45]:

$$F_s = K_s X_s \tag{1.2}$$

The tangential spring fails according to the Mohr-Coulomb criterion, where $F_{s_{max}}$ is the highest shear force and F_{s_0} represents the initial shear force within elements. When the $F_n = 0$, F_{s_0} is the highest shear force that represents the bond of model in Fig. 1.3 [45]. As the F_n value increases, the value of F_s also escalates. If the tangential force exceeds $F_{s_{max}}$, the tangential spring breaks and slip is began [45]. The friction force due to slip is equal to $-\mu_p \times F_n$ where μ_p is the friction coefficient between the inter-elements [45]. Fig. 1.4 illustrates the elastic clump model.

$$F_{s_{max}} = F_{s_0} - \mu_p F_n \tag{1.3}$$

By employing the Newton equation of motion and an iterative algorithm for time step, the elastic clump model can calculate the displacement of individual elements. The linear motion of each element is calculated based on force, acceleration, velocity, and displacement within a small step time. After the calculation, a new time step is initiated for its calculations. The simulation requires several million iterations, allowing for the computation of micromechanical behavior using computers [45].

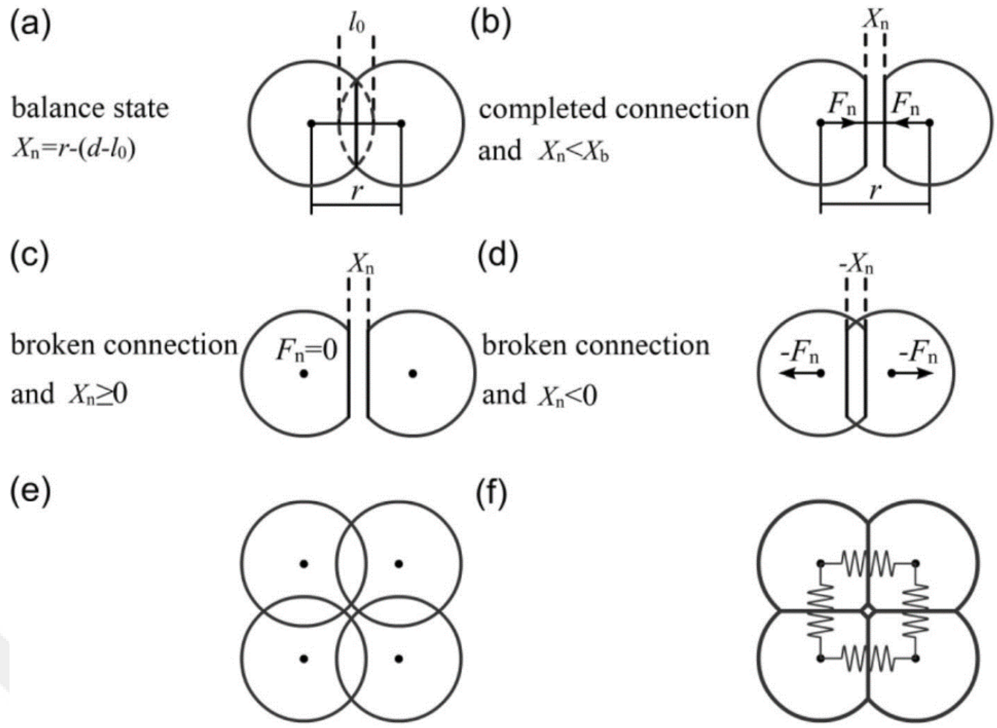

Figure 1.4 : The visual representation of the elastic clump model [45].

Researchers have proposed several contact force models to calculate normal and tangential contact forces, however, it is a common practice to use the linear contact model for the normal direction and the Coulomb friction model for the tangential direction [46]. The linear contact model states that the contact force corresponds to the penetration depth of the bodies in contact, while the Coulomb friction model assumes that the tangential force is corresponds to the normal force and the coefficient of friction between the contacting surfaces. These models provide a simple and efficient way to simulate the contact between particles and have been shown to produce accurate results in various applications, including the simulation of particle dampers [46].

Predicting the impact of PDs on the dynamic behavior of the parts is difficult due to the non-linear nature of PDs. Pourtavakoli et al. claim that the DEM is prevailing computational approaches for analyzing the dynamics of PDs by using unit cells of particle regions [47]. In this study, DEM is used for particle simulations using the to examine the impact of particle shape on the effectiveness of PDs. The DEM simulations use various models to define the interaction forces within particles, chosen based on the shape and material of the particles being simulated. Specifically, a viscoelastic interaction model is utilized to describe the normal contact force between particles [47]. The numerical experiments involve hundreds of complex particles, each with a mass equivalent to a 4 mm diameter steel sphere. These complex particles are made up of multiple spheres with diameters chosen to achieve the desired mass. The particles are initially deposited on the bottom of a PD under Earth's gravity, and subsequently subjected to shaking of the damper with a specified frequency and amplitude in a weightless environment [47]. The research calculates A_{damp}, which represents the energy dissipated by the damper for each cycle, based on the amplitude of the damper's movement. This calculation involves $F(t)$ total force applied by the particles on the cavity boundries of the PD in the motion direction and velocity $(\dot{x}(t))$ over one period ($T = 2\pi/\omega$) with a frequency of ω and A_{damp} [47].

$$x = A_{damp}\sin(\omega t) \tag{1.4}$$

Hence dissipated energy can be found [47]:

$$E_{diss} = \int_T \dot{x}(t)F(t) \tag{1.5}$$

Damping efficiency is related with E_{diss}/E_{max} . E_{max} can be found by $E_{max} = m \times v_{max}{}^2$ where m represent mass and v is velocity [47]. Thus:

$$E_{max} = 4mA_{damp}{}^2\omega^2 \tag{1.6}$$

As a result of damping efficiency calculations, they gave the graphich as in Fig. 1.5 [47].

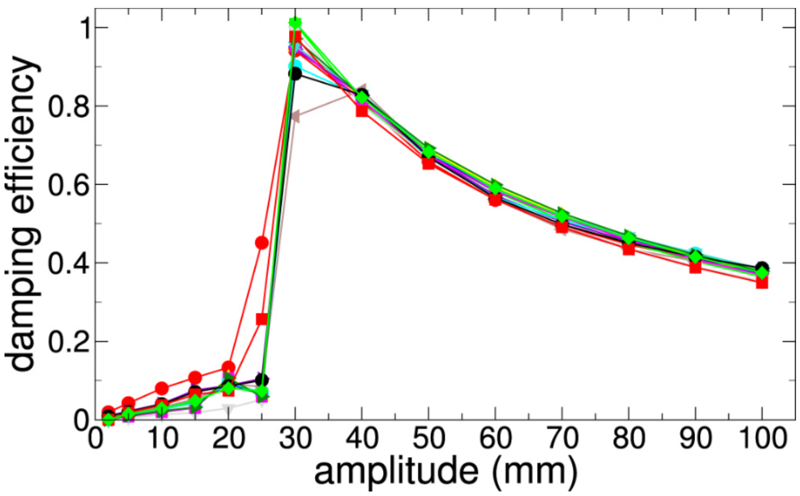

Figure 1.5 : The relationship between damping efficiency and oscillation amplitude [47].

Guo et al. mentioned that the DEM method is computationally expensive due to the need to analyze millions of particles, especially when dealing with unfused cavities although its benefits [44]. Saeki used the multi-unit particle damper method which is based on the linear combination of responses from multiple unit cells [8]. Yet, particle-based numerical simulations using the DEM are unable to investigate the numerous design parameters that have the highest impact on the damping, such as excitation level, cavity dimensions, and packing density [7, 9] which can only be investigated experimentally.

1.3.1.1 Discrete element method and finite element method coupling

Particle dampers are typically simulated using DEM while analyzing the primary body is generally carried out through finite element method (FEM) when both are used together in structures which have multi degree of freedom (MDOF) [5].

The couple of FEM and DEM were successfully applied to basic structures, laying the groundwork for its extension to more complex host structures. This approach involves the use of both FEM and DEM in combination, allowing for a more exhaustive analysis of the damping impact of PDs on MDOF structures. With this theoretical foundation, researchers and engineers can explore the potential of using FEM and DEM to improve the performance of PDs in more complex structural systems. By doing so, it may be possible to enhance the efficiency and effectiveness of particle dampers in mitigating noise and vibration in a variety of industrial applications [5].

Xia et al. used PD on brake system of a vehicle to manage its noise and vibration by calculating the damping effect resulting from the force due to interaction within the particles and the plate. They also suggest that incorporating the union of FEM and DEM is a natural trend in designing particle dampers for MDOF structures [48]. To begin, the researchers calculated the initial positions and velocities of the particles. Then, they used FEM to calculate the reaction of the plate to an impact in one time step [48]. Next, they evaluated the relationship between the particles and the plate. This involved calculating the forces due to interaction within particles-particles and between particles-plate. Using DEM, they then calculated the motion of the particles [48]. Finally, they calculated the response of the plate in subsequent time steps, taking into account both the excitation force and the contact force using FEM as shown in Fig. 1.6 [48].

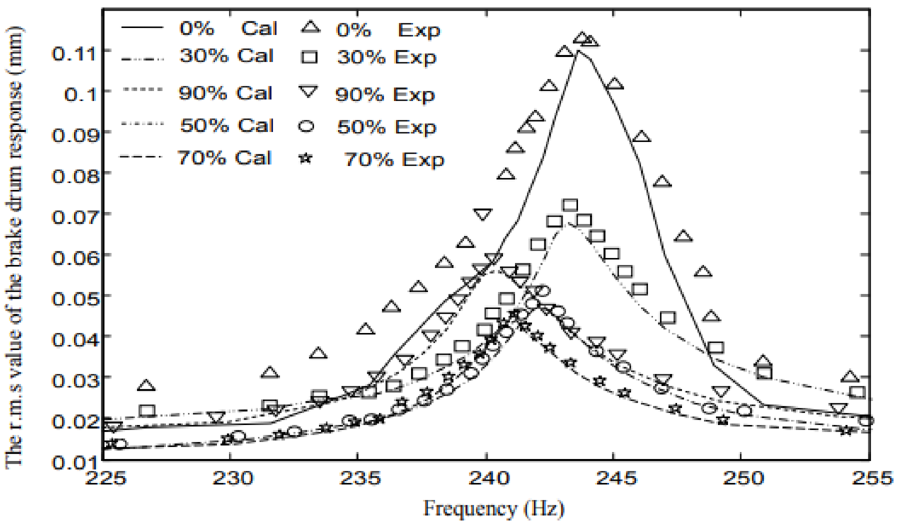

Figure 1.6 : Example comparison of experimental and calculated results for the first mode [48].

By combining FEM, DEM, and experimental results, researchers successfully examined the impact of particle damping. While some differences were observed between test, the results were consistent overall. The findings from the simulation suggest that particle dampers can significantly decrease vibration in brake drums. The performance of PD can be affected by various factors, such as the particle filling ratio, cylindrical cavity diameter, and number of cavities [48].

1.4 Experimental Method

Experimental research has been conducted by scholars to investigate the mechanism of PD. This has been done through various methods, such as studying the effects of gravity on impact dampers [49, 50], examining the dissipation of energy in impact particles [51], and analyzing the impact of strain gradient-induced shear friction [52]. Lastly, through the use of metal and ceramic particles, Hollkamp and Gordon discovered that the vibrational energy resulting from the vibration of primary body is able to be decreased through collisions among the particles [53]. The results of these experiments demonstrate that PDs are able to ensure substantial damping over a wide frequency range, and one possible way to achieve optimal damping is by using multiple particles as impact bodies, and considering the effects of friction, impact, and shear mechanisms [53].

The other way involves validating results and studying the damping effectiveness of different PDs in vary structures that are exposed to vibration due to external impacts.

Scholars have conducted experiments on vertical multiparticle impact dampers [54], particle dampers under centrifugal loads [55], and compared the damping effectiveness of PDs and MUPDs [56]. Simplified models of resilient bags and particle dampers have been established and validated by experiments [57]. Furthermore, there have been multiple experimental researches conducted to investigate the behavior of PDs under different levels of amplitude [58–60].

In the third aspect of PD research focuses on exploring how different design parameters impact the vibration decrease on a structure and how to apply this knowledge in practical engineering settings through parametric analysis. Studies have examined the effects of factors such as material, mass, and optimal clearance of the impact bodies on damping performance [61–64]. Design curves have been developed to forecast the damping properties of PDs, and various design parameters have been analyzed through testing, including particle type, placement, and packing ratio [65].

1.4.1 Review of experimental studies

Ehlers et al.'s experimental study provided valuable insights into the impact of different design parameters on the dynamics of manufactured parts with PDs [12]. Specifically, the study focused on the effects of excitation level, particle mass, packing density, and PD dimensions. By systematically varying these parameters, the researchers were able to identify the optimal combination of design factors that produced the desired damping effect. The researchers utilized a hammer impact test setup controlled by a step motor to provide similar impacts to the specimen. The specimen was positioned on foams to allow for free-free boundary conditions [12]. Figure 1.7 illustrates the test setup.

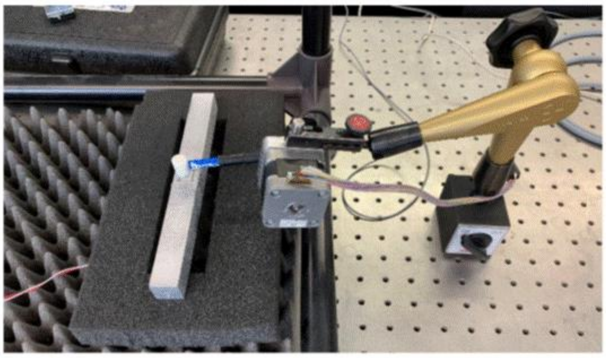

Figure 1.7 : A test setup where impulse hammer excitation was controlled by a motor was employed to assess the particle damping properties from study of Ehler at al. [12].

The findings of this study have important implications for the practical application of PDs in engineering. Further research in this area could help to refine our understanding of the factors that influence the performance of PDs and ultimately lead to more effective and efficient damping solutions for a wide range of engineering applications. [12, 38]. The investigation of PD on LPBF Al-Si-10Mg unconstrained beams involved a thorough experimental setup, where impulse hammer excitation was controlled by a motor.Through this experimental approach, Ehlers et al. were able to explore the influence of several design parameters, including PD dimensions, packing density, particle mass, and excitation level, on the dynamics of fabricated parts with PDs. This research is crucial in understanding the behavior of PDs in unconstrained beams and could provide valuable insights for the optimization of PD designs in various industrial applications. [12]. A notable decrease in vibration amplitudes by using PDs while achieving broadband damping of the first seven bending modes was revealed [12]. Ehlers et al. demonstrated that the damping behavior of the fabricated parts with PDs is dependent on the frequency of vibration and that damping is able to be improved up to 20 times. Additionally, they examined the sensitivity of damping to the excitation of force amplitudes and determined that the damping ratios remained consistent for impact force magnitudes above 100 N [12]. These findings are significant as they provide insight into the effectiveness of PDs in reducing vibration amplitudes across a broad frequency range and their robustness in varying force amplitudes. These results can be useful in the development of damping solutions for many applications, particularly in the manufacturing industry where usage of PDs can help mitigate vibration and improve product quality. [12]. However, as the force magnitude increases, the particles gain enough momentum to overcome stiction and start damping the vibrations effectively [13]. This leads to an increase in damping as the force magnitude increases. This finding highlights the importance of understanding the relationship between impact force magnitude and damping behavior in particle damping systems, and it could have significant implications for the design of effective damping systems in engineering applications. [13].

Emuakpor et al. investigated how the position of PDs affects damping effectiveness in IN718 beams manufactured through LPBF [41]. To conduct their study, the researchers utilized a shaker setup with a clamped-free boundary condition. The shaker allowed for controlled excitation, while damping behavior was measured using accelerometers [41]. Test setup is given in Fig. 1.8.

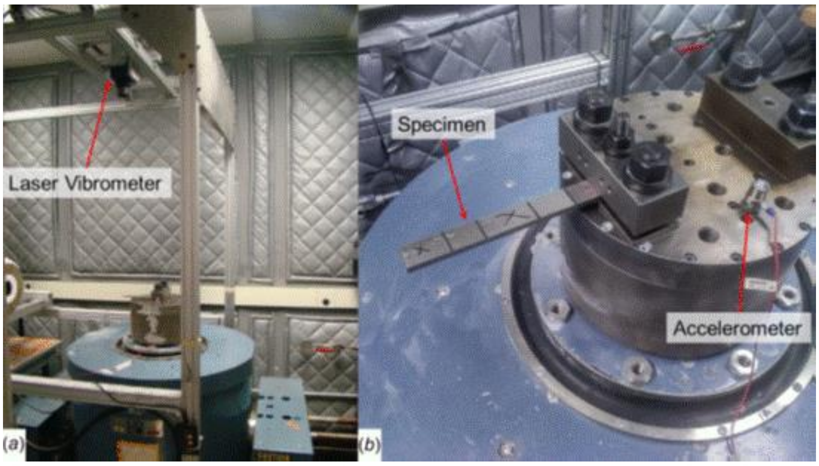

Figure 1.8 : The shaker test setup from study of Emuakpour at al. included a cantilever clamped beam, which is depicted in (a) as a full view and in (b) with three bolts attached to it [41].

The beams had a length of 120 mm, width of 10 mm, and height of 3 mm, with PDs placed at 20% and 80% of their length. The researchers measured damping using an electrodynamic shaker and observed that PDs located closer to the clamping point had a stronger damping effect, with the PD located at 80% of the beam's length showing the highest damping ratio [31, 39, 41–43]. Goldin et al. studied to explore how the number of PDs influences the damping behavior of LPBF-manufactured AISI 316L beams. The beams, which were 100 mm in length, 10 mm in width, and 3 mm in height, were equipped with PDs placed at the center. The number of PDs used in the study varied from one to three, and the damping behavior was measured using a laser vibrometer. The study's findings showed that an increase in the number of PDs led to a corresponding increase in the damping ratio. The greatest increase in damping ratio was observed between one and two PDs. [40]. The damping capability of four different beam configurations subjected to clamped-free boundary conditions was found to have significantly improved according to the results of modal tests. To conduct these tests, a fully-fused solid beam was compared with three other beams that had internal unfused powder volume modifications varying from 1% to 4% [31, 39].

The analysis concentrated on the initial three bending modes, and the results revealed that the altered beams exhibited up to 10 times greater damping capability than the fully-fused solid beam. The study findings indicate that modifying the internal unfused powder volume of LPBF-manufactured beams has the potential to significantly enhance their damping capabilities. [31, 39].

Unfused powder volume fraction was found to be effective for less than 4% on damping performance [39]. Knowing the threshold of volume fraction is crucial to building a mechanically very similar part to a fully dense version with optimal damping performance [39]. In a recent study, a compressor-like blade geometry was employed to demonstrate the validity of the unfused powder volume effective threshold [42]. This confirmed that the unfused cavities can be utilized to suppress the vibrations for complex structures even when the total unfused volume is less than 1%. Furthermore, it has been investigated that the damping performance of PDs becomes stable when millions of cycles are applied at high strain ranges to understand the sustainability of the damping performance. Even though a substantial drop in the damping with PD is observed, it is still two times higher than the damping performance of a fully dense version [42].

1.5 Thesis Outline

Although the fact that numerous studies have explored the effect of diverse design parameters, examples may include cavity location, number, and dimension on the damping performance of structures, to the best of the authors' knowledge, no single study has systematically compared and quantified the influence of these design parameters. Although some individual studies have investigated the impact of each of these design parameters separately, the lack of a comprehensive comparison limits the ability to understand their relative importance and to identify optimal design configurations. Therefore, a study that quantifies and compares the influence of these design parameters could provide valuable insights into how to optimize damping performance in various applications, such as aerospace, automotive, and civil engineering. The potential to optimize damping performance through design parameter alterations is crucial in various engineering applications. However, achieving optimal damping performance requires a deep understanding of the effect of each design parameter on the overall damping behavior of the structure. Therefore, the present study aims to provide valuable insights into the influence of key design parameters, for instance the volume of unfused powder, cavity number, and their positions, on particle damping performance. This study aims to contribute to the development of structures that have improved damping capabilities by quantifying the effect of these design parameters. The findings of this study could help engineers and designers to tailor the design parameters to specific applications and optimize the damping performance of various structures. Additionally, the insights gained from this study could contribute to the development of new materials and fabrication techniques that can improve damping performance, thereby opening up new avenues for research in the field of structural engineering. To accomplish the goal of quantifying the impact of the volume of unfused powder, cavity number, and their positions on particle damping performance, a systematic approach is necessary. Therefore, a design of experiment (DoE) is prepared, taking into account the aforementioned design parameters. This approach allows for the creation of a structured experimental plan that covers the possible variations of each design parameter, ensuring the most efficient use of the available resources and reducing the potential for errors.

To investigate the damping performance of the samples, sixteen specimens with PDs defined in the DoE and a fully-fused beam made of Inconel 718 were fabricated using LPBF. The use of LPBF provides a high level of control over the manufacturing process, enabling the production of samples with precise dimensions and geometries. Furthermore, the use of Inconel 718, a high-strength, corrosion-resistant superalloy, ensures that the results obtained from this study are applicable to a wide range of engineering applications. To evaluate the impact of the design parameters on particle damping performance, experimental modal analysis is performed using impulse excitation. This technique enables the measurement of the natural frequencies and damping ratios of the samples, providing a quantitative assessment of their damping performance. The impact of each design parameter on the damping performance is examined for each sample, and the results are compared with those of the fully-fused sample. This comparison enables the identification of the design configurations that exhibit the most significant improvements in damping performance, providing valuable insights into the optimal design of structures with enhanced damping capabilities.

To understan the vibration behavior of the printed samples, a quantitative evaluation method is necessary. Therefore, in addition to the modal analysis, the root sum square (RSS) method is identified as a key performance metric in this study. The RSS method is a widely used approach for analyzing vibration data and is particularly useful for characterizing the damping behavior of structures. By utilizing the RSS method, the damping performance of the specimens with unfused cavities can be accurately measured and compared with that of the fully-fused component. Furthermore, to for better understanding of the damping behavior of the specimens with unfused cavities, finite element analysis (FEA) is conducted to get the samples' mode shapes. These shapes obtained from FEA are then used to analyze the damping characteristic of the specimens. This approach enables a detailed analysis of the relation of the damping performance and the mode shapes of the specimens, providing valuable insights into the underlying mechanisms of particle damping. The results demonstrate that the integration of particle dampers can significantly improve the damping performance of structures, with up to 10 times improvement observed compared to a similar fully-fused component. These findings highlight the importance of considering the design parameters of particle dampers when developing structures with enhanced damping capabilities. Finally, the DoE approach employed in this study can be utilized as a guideline for estimating the damping behavior of beams with particle dampers. This approach enables the identification of the optimal design configurations for particle dampers, facilitating the development of structures with improved damping performance in a range of engineering applications.

2. MATERIALS AND METHODS

2.1 Design of Experiment (DoE)

To provide a comprehensive analysis of the effect of design parameters on damping, this study considered the impact of size, location, and number of the damper cavities. A design of experiment (DoE) was prepared to systematically vary these parameters, resulting in a total of 16 specimens with integrated PDs being additively manufactured. In addition to the 16 specimens with PDs, a fully-fused specimen was also included as the control specimen. The inclusion of this control specimen enabled a direct comparison between the damping performance of the fully-fused specimen and those with integrated PDs, providing a baseline for assessing the effectiveness of the PDs in enhancing damping performance. The use of a DoE approach enabled the investigation of the individual and combined effects of design parameters on damping behaviour. This study aimed to compare configurations for PDs by systematically varying these parameters in a methodical manner. PDs. Overall, this study highlighted the significance of taking PD design parameters into account to enhance the damping capabilities of structures. To achieve this goal, a wide design of experiment (DoE) and the inclusion of a fully-fused control specimen were used. The results demonstrated the crucial role of design parameters in determining damping performance.

To ensure consistency across all specimens, the external dimensions of the specimens were maintained at 148 mm × 60 mm × 10 mm. The PDs were designed to have a constant thickness of 6 mm and a width of 40 mm, centered in both directions. Lengths of PDs were varied to create a feasible study design that would allow for a comprehensive investigation of the damping effects on mode shapes. Purpose was conducting a Design of Experiment (DoE) study exploring the relationship between mode shapes and damping performance. The length of PDs were chosen as 20 mm, 40 mm, and 80 mm. The dimensions and locations of the PDs in all specimens are shown in Fig. 2.1. In addition to the length of the PDs, their thickness and location on the specimen are also important factors that can influence the damping performance. By controlling these variables, the DoE study can systematically evaluate how different damping mechanisms affect the mode shapes of the specimens. For example, the thickness of the PDs can be adjusted to control the level of damping, with thicker PDs generally providing greater damping. On the other hand, in this study the rest of the dimensions were kept constant for PDs except lenght.

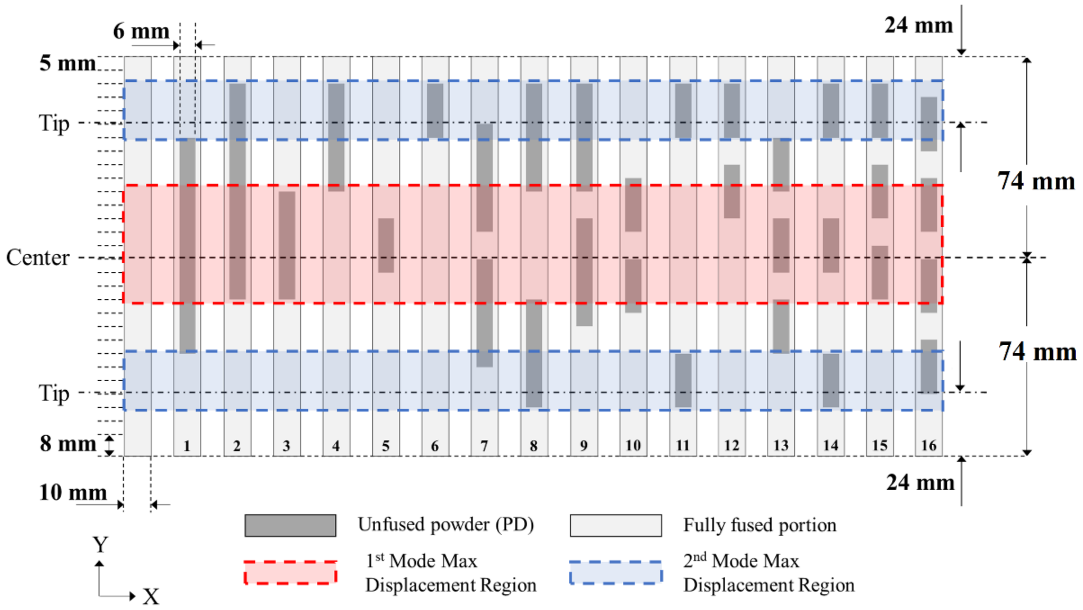

Figure 2.1 : Schematic side view of specimens. Geometric center and tips of specimen showed with dashed line. The region of maximum displacement due to the first mode is shown with the red rectangle, and the maximum displacement regions due to the second mode are shown with the blue rectangles.

The study also explored the effects of varying the location and number of PDs on damping performance. Fig. 2.1 provides a visualization of the different PD configurations used in this study. The number of PDs, their size, and their location were changed to understand the individual and combined effects of these parameters on damping. By placing the PDs in different locations, the study planned to investigate how damping affects different regions of the specimen, and how this impacts the overall mode shapes.

This study aimed to be an experimental reference for optimizing the most effective PD configurations for enhancing damping performance in additively manufactured structures. Overall, the dimensions of the PDs, as well as their placement on the specimen, play a critical role in the DoE study, allowing researchers to systematically investigate the relationship between damping and mode shapes in a controlled and meaningful way.

The specimens were grouped to determine the impacts of the cavity length, location, and the number of PDs on the damping performance. Definitions of the grouping for the LEN, LOC, and NOD are given in Table 2.1. Groups of LEN 1 – 4 were designed to understand the effect of PD length on damping performance. Note that, the regions (center or tip) and the number of PDs were designed similar for the specimens in each LEN group. LOC 1 – 6 were used to understand the effect of the PD locations considering different numbers and sizes of dampers. Finally, NOD 1 – 4 were prepared to examine the effect of the number of PDs. Furthermore, NOD 1 – 2 and NOD 3 – 4 were designed to investigate the PDs located at the center and the tip of the specimens, respectively. Fig. 2.1 depicts the schematic side view of the specimens.

Table 2.1 : Designed specimens in groups according to the investigated parameter.

Parameter Definition	Group Name	Specimens in Group
I) Effect of the length of the dampers	LEN 1	1, 3, 5
	LEN 2	2, 4, 6
	LEN 3	8, 11
	LEN 4	9, 12
II) Effect of the locations of the dampers	LOC 1	1, 2
	LOC 2	3, 4
	LOC 3	5, 6
	LOC 4	7, 8, 9
	LOC 5	10, 11, 12
	LOC 6	13, 14, 15
III) Effect of the number of dampers	NOD 1	1, 7, 16
	NOD 2	3, 10
	NOD 3	2, 9
	NOD 4	4, 12

A further DoE was carried out with the aim of exploring how the damping performance is affected by various parameters such as thickness, width, and boundary conditions (In the upcoming section, this DoE will be referred to as the 2nd DoE.). For specimens with an increasing number of cavities, the volume fraction between particle-filled cavities and the total structure volume is 9.2%, 18.4%, and 27.6%, respectively (see Fig. 2.2 for specific dimensional properties). To measure damping performance improvement, researchers used six particle-filled specimens with varying design parameters and a fully-fused specimen of the same dimensions. Additionally, to examine the effects of boundary conditions, the specimens were tested under clamped-free and free-free conditions.

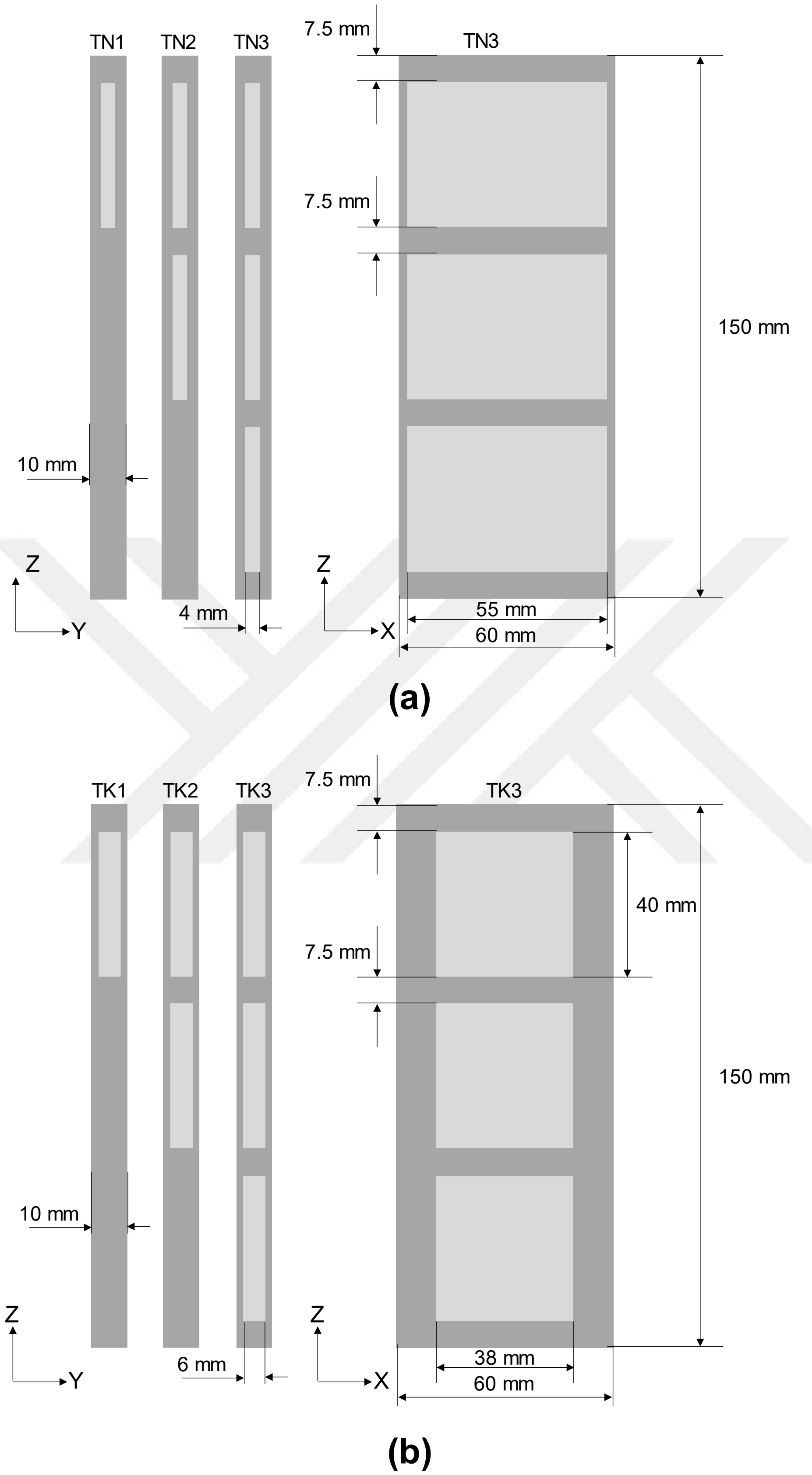

Figure 2.2 : 2nd DoE for testing width, thickness and boundary conditions on damping (a) TN Models (b) TK Models.

2.2 Manufacturing of The Specimens

2.2.1 Design parameters and build layout

Once the designs are finalized at computer-aided design (CAD) environment, the next step in the manufacturing process is to create a build layout. This layout is critical in ensuring that the design is optimized for additive manufacturing (AM) and follows best practices for this particular process, such as cross-section approximation, tilt angle, wall thickness, part size, etc [32].

One important consideration when designing a build layout for AM is cross-section approximation. Ehlers at al. suggest that by following manufacturing limitations, it is feasible to create cavities filled with particles that have a smallest cross-sectional area of 2×2 mm² [32]. Another crucial factor to consider when designing a build layout is the tilt angle. This is the angle at which the part is positioned on the build platform, and it affects the support structures needed to hold the part in place during the printing process. Optimal tilt angles help minimize the need for support structures and improve the part's surface quality. This angle should be less or equal to 45° according to same study. Wall thickness is another design consideration that impacts the build layout [32]. The CAD software will ensure that the wall thickness is consistent and appropriate for the selected material and printing process. Additionally, the software will take into account the part size and the printer's build volume to optimize the layout for the best printing results. Study of Ehlers at al. specifies that the wall thickness is restricted to a minimum of 0.6 mm [32].

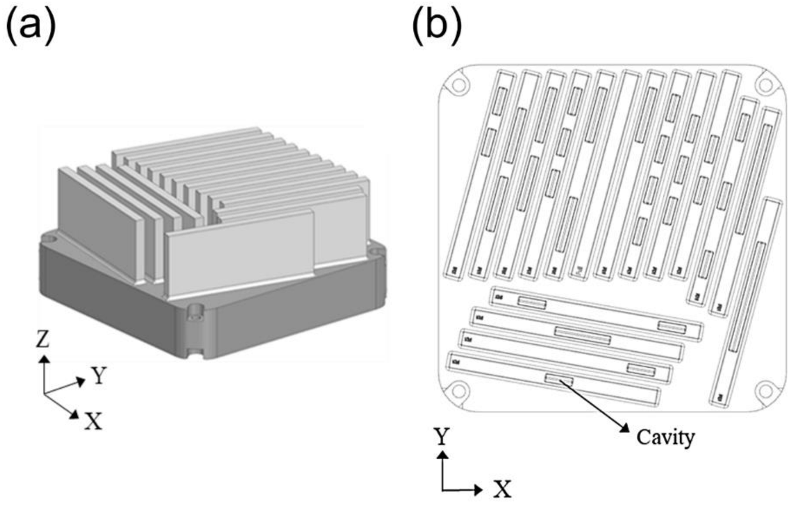

Figure 2.3 : (a) Isometric view and (b) transparent top view of printed samples on the build plate.

Overall, creating a build layout is a crucial step in the AM process, as it ensures that the part is optimized for the selected printing technology and results in a high-quality final product. In this study, these and similar criteria were taken into account during the design process. However, it should be noted that these limiting factors may change in the future with developing material and machine technology.

In this study, after design phase was completed, build layout was prepared as shown in Fig. 2.3 and started to work on converting these to machine readable format.

Similar processes were performed for 2nd DoE too. Build layout and printed specimens showed in Fig 2.4.

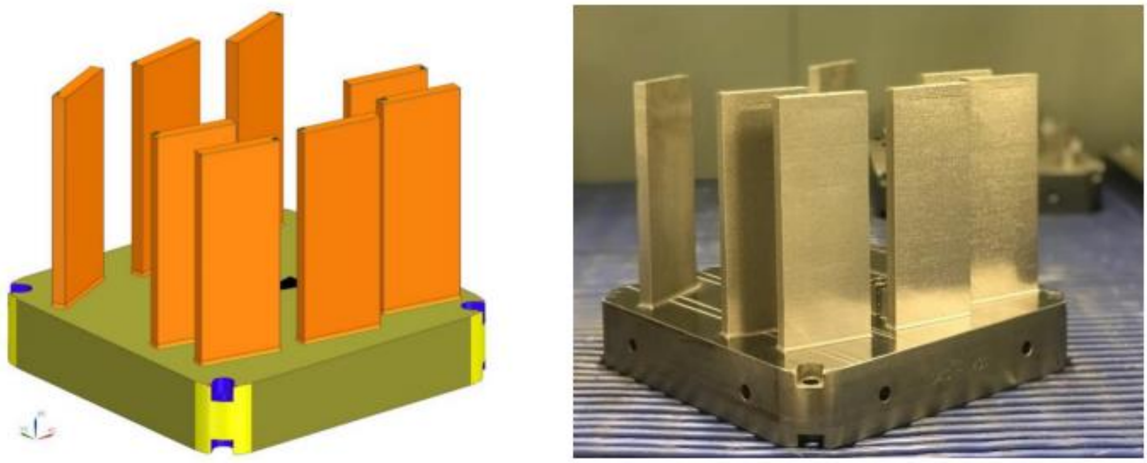

(a) (b)

Figure 2.4 : (a) Specimens in CAD environment (b) printed specimens.

2.2.2 Machine readable format and slicing

The process of converting a three-dimensional (3D) model into a set of instructions that can be interpreted by a 3D printer is commonly referred to as "slicing." Essentially, this technique involves dividing the 3D model into multiple thin layers and determining the optimal printing approach for each layer (i.e., the tool path) to achieve desired outcomes such as minimum time, maximum strength, and other relevant characteristics. Slicing plays a crucial role in the successful implementation of 3D printing technology, particularly in the manufacturing industry, and thus understanding this process is essential for effective and efficient use of this technology [66, 67]. Process illustration is given in Fig. 2.5.

Build a layouts that are represented in Fig. 2.3 and Fig. 2.4, which indicates how the parts are arranged and aligned on the build plate to optimize the use of space and minimize support structures. Then, transform the CAD data of the parts into a format (.cls) that the machine can read and interpret, including details about the parts' shape and slicing settings such as layer thickness and hatch spacing.

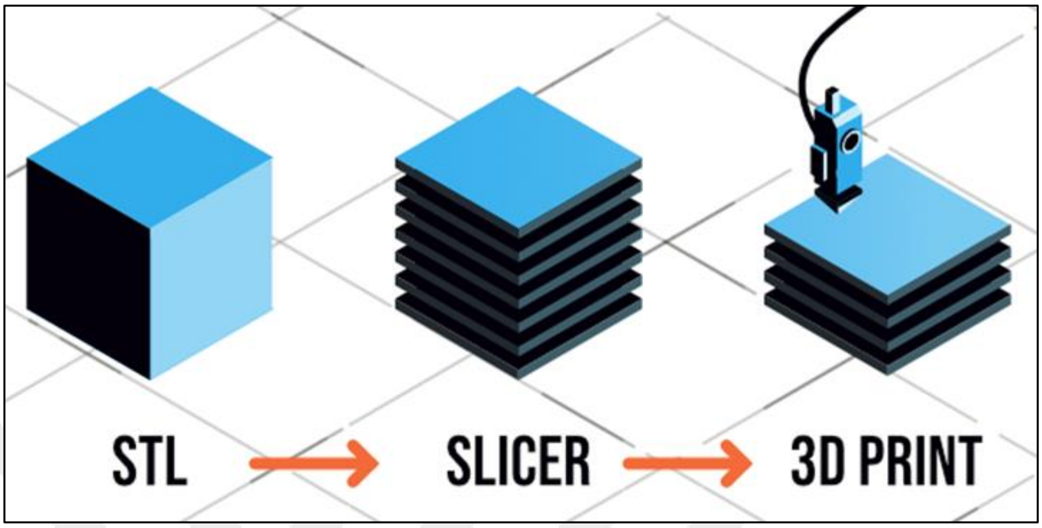

Figure 2.5 : Illustrations of slicing and printing of a 3D data [66].

Hence, it is possible to create gcodes for the parts, which are a series of commands that specify the coordinates and parameters for each layer. Generating gcodes for the additive manufacturing (AM) machine is essential, as they are instructions that tell the machine how to move and deposit material in layers according to the gcode commands. This way, printed models that conform to the design criteria and specifications, such as dimensional accuracy and surface quality, can be produced.

2.2.3 Material and manufacturing

2.2.3.1 Inconel 718

The exceptional properties of Inconel 718 have made it a highly desirable material for a wide variety of industrial and aerospace applications. This nickel chromium alloy exhibits superior durability and corrosion resistance, making it ideal for use in harsh environments that range from cryogenic temperatures up to 1300°F. Furthermore, Inconel 718 has excellent mechanical properties, including high tensile, fatigue, creep, and rupture strength, which make it a popular choice for fabricating components that require high-stress performance [68].

In addition to its use in traditional manufacturing processes, Inconel 718 has become a popular material in metal additive manufacturing due to its high-temperature resistance and structural integrity. Its applications in this field include manufacturing parts for aircraft, gas turbines, and other corrosive and structural components. Numerous studies researched the mechanical properties of Inconel 718 manufactured using additive manufacturing techniques [69].

Praxair, the vendor for Inconel 718 powder, provides data on the element composition of the alloy in Table 2.2 [70].

Table 2.2 : Element composition in vendor data [70].

Element	Composition Range
Ni	50.000 – 55.000
Cr	17.000 – 21.000
Fe	15.000 – 21.00
Nb+Ta	4.750 – 5.500
Mo	2.800 – 3.300
Ti	0.650 – 1.150
Al	0.200 – 0.800
Co	≤ 1.000
Mn	≤ 0.350
Si	≤ 0.350
Cu	≤ 0.300
C	≤ 0.080
Ta	≤ 0.050
P	≤ 0.015
S	≤ 0.015
B	≤ 0.006

According to Praxair's data, the alloy's excellent properties are available up to 1300°F (704°C), as previously stated in another source. Furthermore, Praxair provides typical mechanical properties of the alloy for as build structures in the Table 2.3 below [70].

Table 2.3 : Mechanical properties at room temperature for Inconel 718 powder in vendor data [70].

Mechanical Property	Orientation	As Built	As Built Min. ASTM F3055-14
Tensile Strength	XY	1080 ± 50 Mpa	980 Mpa
	Z	960 ± 50 Mpa	920 Mpa
Yield Strength	XY	800 ± 50 Mpa	940 Mpa
	Z	625 ± 50 Mpa	920 Mpa
Elongation	XY	31 ± 5 %	12 %
	Z	35 ± 5 %	12 %

It is worth noting that the particle size distribution of the Inconel 718 powder can be customized to suit specific applications upon customer request [70]. For this study, particle size distribution includes d_{10} = 23 µm, d_{50} = 35 µm, and d_{90} = 50 µm.

Overall, the unique combination of properties exhibited by Inconel 718, including its excellent mechanical performance, resistance to corrosion, and ease of fabrication, have made it a versatile and widely used material in a diverse range of industries. Due to its remarkable mechanical characteristics such as robustness, endurance against fatigue, creep, and rupture, the alloy proves to be a dependable and long-lasting substance in severe surroundings. In addition, Inconel 718's customizability and versatility make it an attractive option for use in various industrial and aerospace applications, including components for gas turbines, cryogenic tankage, and various sheet metal parts.

2.2.3.2 Manufacturing with laser powder bed fusion

Laser Powder Bed Fusion, is a cutting-edge technology that is revolutionizing the manufacturing industry. The use of lasers to melt thin layers of metal powder is allowing for the creation of complex and intricate 3D objects. This process of LPBF begins with the creation of a CAD-generated .stl file, which is then converted into a sliced file using specialized software. This sliced file is then transformed into .cls and sent to a machine for building. The use of lasers to selectively melt tiny particles in the metal powder allows for precise control over the manufacturing process, resulting in objects with uniform and accurate features [71].

Figure 2.6 : Laser melting phase of LPBF process [71].

The process of building the object layer by layer is made possible by the motion of the recoater is responsible for applying a fine layer of metallic powder onto the printing surface. The laser follows the scan paths laid out in the sliced file to melt the powder. This process is repeated until all layers have been printed, and any excess powder is removed to reveal the final product [71]. A picture from part manufacturing is given in Fig. 2.6.

One of the most significant advantages of LPBF is the minimal finishing required on the final product. The precision and accuracy of the laser melting process result in objects with smooth and even surfaces, reducing the need for additional processing. As this technology continues to advance, it is likely to become an increasingly essential part of the manufacturing industry. The ability to produce complex 3D objects quickly and with minimal finishing is a game-changer that is opening up new possibilities for designers and engineers alike [71].

2.2.4 Post-processing

After the completion of the printing process, unmelted powder was evacuated. The next step is to remove the printed object from the build plate. In the case of the LPBF process, the removal of the object from the plate is performed with the help of wire electrical discharge machining (EDM) operation. No heat treatment and/or surface finishing process was applied to the printed specimens.

Volume fractions of the PDs are important to compare with each model [12]. In addition to the volume fraction information, the specimens were weighed using a precision scale with 1 g sensitivity (Techfit TF-1010), and the results have been presented in Table 2.4. The weight information is crucial for analyzing the density of the specimens and identifying any discrepancies in the printing process. By comparing the weight and volume fraction data, one can obtain insights into the accuracy and quality of the 3D printing process, and identify any potential errors or defects. Therefore, the combination of volume fraction and weight data provides a comprehensive picture of the 3D printed specimens and their characteristics.

The processes were the same for this 2nd DoE, but unlike the 1st DoE, tests were conducted to simulate the clamped-free condition before the separation process with EDM. This was a lessons learned that will be discussed in more detail in the section where modal tests are described. In the first DoE, clamped-free tests were also attempted, but unstable measurements were obtained due to insufficient clamp load. The aim in the 2nd DoE was to find a solution to this issue. The cutting process was performed after the clamped-free tests in this case. Results for 2nd DoE are given in Table 2.5.

Table 2.4 : Dimension of PDs, volume fraction of PDs and mass of the specimens in the 1st DoE.

Specimen No	Centerline Based Cavity Dimensions (mm)	Number of Cavities	Mass (g)	Volume Fraction (%)	Cavity Locations
0 (Fully Fused)	-	-	731	-	-
1	80×40×6	1	670	20	Center
2	80×40×6	1	669	20	Tip
3	40×40×6	1	697	10	Center
4	40×40×6	1	701	10	Tip
5	20×40×6	1	711	5	Center
6	20×40×6	1	712	5	Tip
7	40×40×6	2	670	20	Center
8	40×40×6	2	669	20	2 Tips
9	40×40×6	2	671	20	Tip
10	20×40×6	2	700	10	Center
11	20×40×6	2	698	10	2 Tips
12	20×40×6	2	701	10	Tip
13	20×40×6	3	685	15	Center
14	20×40×6	3	684	15	Center & 2 Tips
15	20×40×6	3	685	15	Tip
16	20×40×6	4	669	20	Center

Table 2.5 : Dimension of PDs, volume fraction of PDs and mass of the specimens in the 2nd DoE.

Specimen No	Centerline Based Cavity Dimensions (mm)	Number of Cavities	Mass (g)	Volume Fraction (%)	Cavity Locations
0 (Fully Fused)	-	-	737	-	-
1	40×55×4	1	707	9.2	Tip
2	40×55×4	2	677	18.4	Tip & Center
3	40×55×4	3	647	27.6	Center & 2 Tips
4	40×38×6	1	708	9.2	Tip
5	40×38×6	2	677	18.4	Tip & Center
6	40×38×6	3	646	27.6	Center & 2 Tips

For 2nd DoE, the fully-fused counterparts of particle-filled beams are up to 13% heavier. More specifically, around 30 g of material is saved in each unfused cavity since the particles in the unfused cavities are less dense than those in the fused material.

After the tests were conducted, Specimen 5 was selected (arbitrary), drilled to empty the powder, and tested. Fig. 2.7 shows specimen and emptied powder. The objective here is to compare the results of this test with the results before the powder was emptied and the results of the fully-fused specimen.

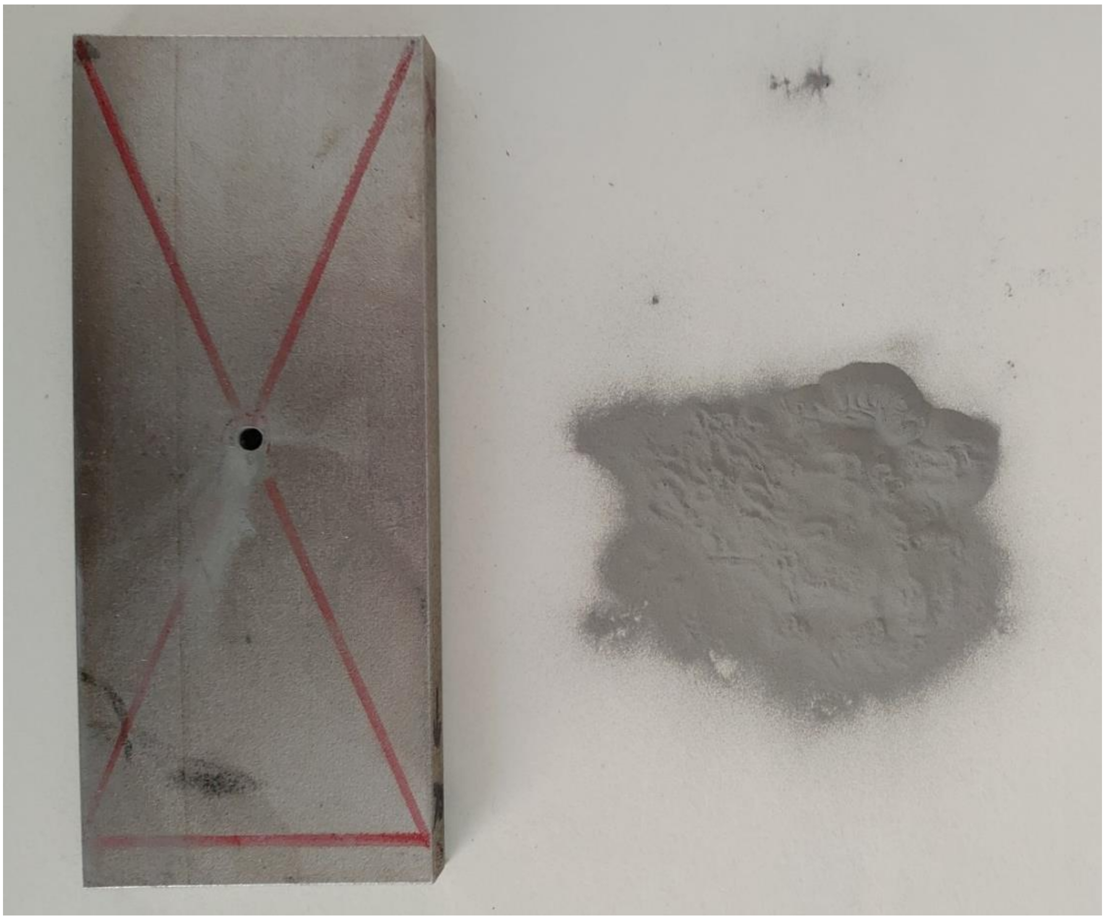

Figure 2.7 : Specimen 5 and emtied powder.

2.3 Numerical Modeling

Finite Element Analysis (FEA) is a potent technique utilized to model and analyze the behavior of various systems. In this instance, ANSYS 19.2 was utilized for FEA to get mode shapes. Natural frequencies denote the inherent vibration frequencies of a structure, which are crucial for identifying potential design flaws or sources of failure. Mode shapes, on the other hand, represent the deformation or vibration pattern of a structure at each natural frequency.

The FEA conducted determined the natural frequencies and mode shapes of the specimens in question, enabling the validation of experimental results and comprehension of the impact of PD location. This information can be crucial for optimizing the system's design to maximize the impact of PD and enhance its damping capability.

The use of FEA allows for a detailed understanding of the behavior of PDs under different deformation profiles of the specimen. The SOLID45 hexagonal mesh elements (as shown in Fig. 2.8) used in building the FEMs provide a robust and accurate representation of the structure being analyzed [72].

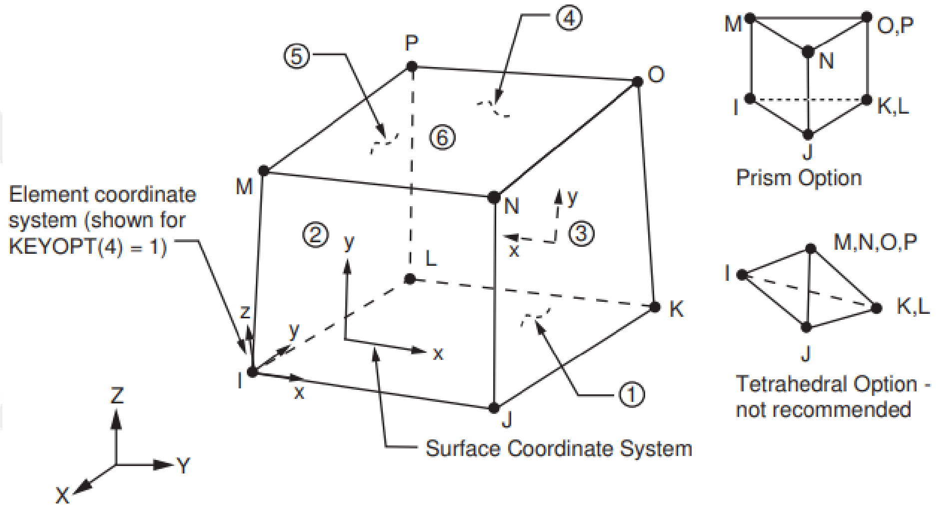

Figure 2.8 : SOLID45 Geometry [72].

The approximation of particle damper cavity volumes as empty regions enables the simulation of the damping behavior without the influence of the cavity shape and size on the structure. However, it is important to consider the mass of unfused powder in the PD, which can affect the overall behavior of the system. To understand this impact, the accurate modeling of the mass of the unfused powder in the PD is essential for understanding its behavior and optimizing its design to enhance its performance in real-world applications.

The MASS21 nodal mass element is commonly used in FEA to model concentrated masses in structures. It is a point element that is typically located at a node of a structural element such as a beam, shell or solid element. The MASS21 can have up to 6 degrees of freedom (DoF). Each coordinate direction can have a unique mass and rotary inertia assigned to it [72]. Therefore, the MASS21 nodal mass elements were used to model the mass of the unfused powder. These elements are highly effective in accurately representing the mass of each particle and its distribution within the damper. Additionally, the RBE3 elements used to tie the nodal masses to the external nodes of the cavity walls help prevent any additional stiffness from being introduced into the model [73].

During the modal analysis, the boundary conditions were set as free on all sides, and the first two modes, namely the bending and torsional modes, were studied to compare with modal tests. The first two mode shapes of the fully fused model can be seen in Fig. 2.9. The mode shapes of all the specimens exhibit minor differences, such as frequency shifts and deflection variations, due to the location of the internal cavity and the effects of the PDs. Also, first five mode shapes of all specimens in 1st DoE are given in appendix. On average, the first mode had a 4.1% shift, and the second mode had a 3.3% shift, according to the test results. These variations are caused by the changes in stiffness and mass resulting from the particle dampers. It is crucial to consider these variations and accurately model the mass of the unfused powder in the PD to optimize its design and improve its performance in practical applications.

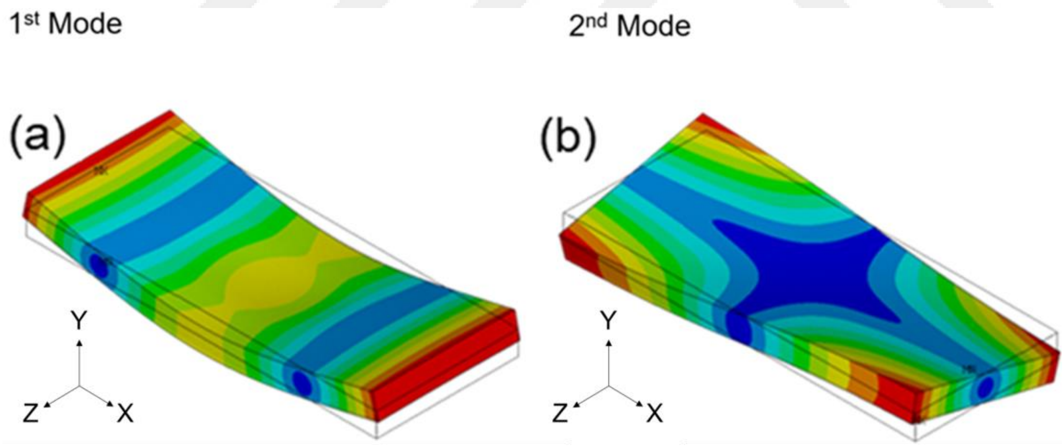

Figure 2.9 : The first two mode shapes (bending and torsional modes) of the fully fused model.

Since the 2nd DoE does not aim to compare the impact of mode shape, it was not included in the scope, and analysis was not performed for the 2nd DoE.

2.4 Experimental Setup and Test Plan for Extracting Damping Ratio

Vibration tests can be used to determine the natural frequencies, damping ratios, and mode shapes of an object. Modal tests are commonly employed for this purpose. Tests consist of measurement and post-processing stages. It is possible to perform experimental modal analysis using a shaker, as well as read results from an accelerometer by applying an impact with a hammer equipped with a sensor at the tip as illustrated in Fig. 2.10 [2, 74, 75].

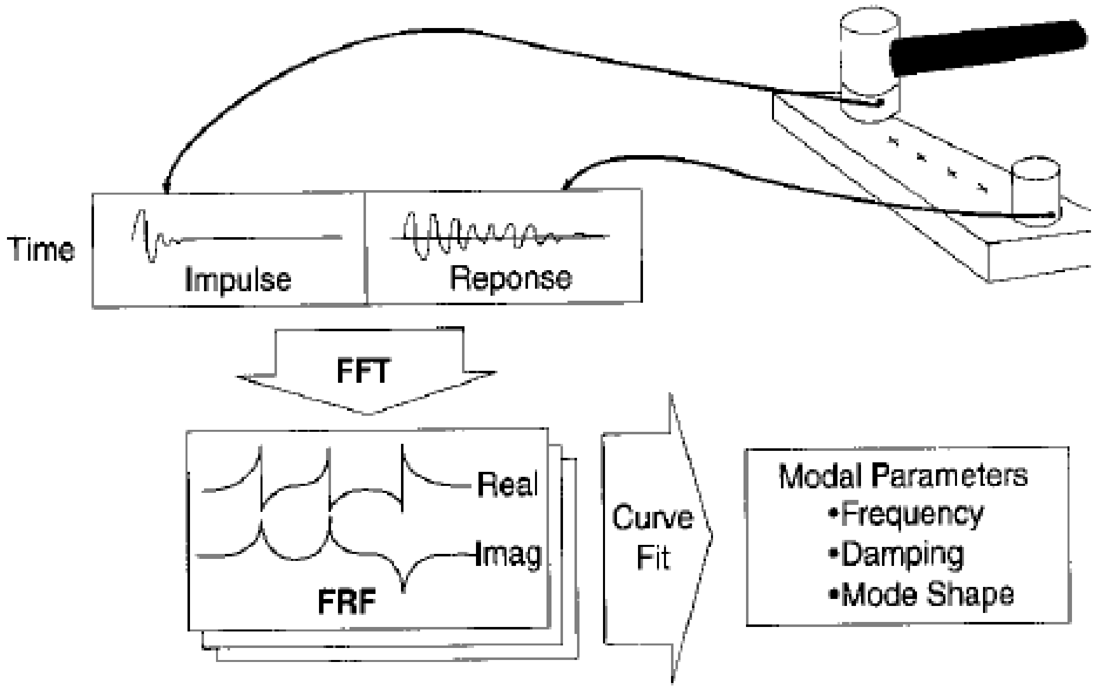

Figure 2.10 : Hammer impact test illustration [75].

Hammer impact modal testing is performed by striking a structure with a hammer and measuring the response with sensors such as accelerometers. The test is conducted by striking multiple locations on the structure and recording the response with sensors, followed by analyzing the data to determine the natural frequencies and damping ratios. This technique can be conducted on existing structures without requiring modifications and is relatively quick and inexpensive compared to other modal testing methods. However, the results can be influenced by the impact location, the type of hammer used, and the sensor measurement accuracy. Furthermore, hammer impact testing only provides information about the impact points [2].

Firstly, as seen in Fig. 2.11, a clamped-free test setup was created. The 8 mm holding area provided during the design stage was held with a vise and tested on the samples. Due to excessive noise, a reliable measurement could not be taken. Even though the clamping area was increased, stable test results could not be obtained. Therefore, it was decided to obtain results only for free-free boundary conditions.

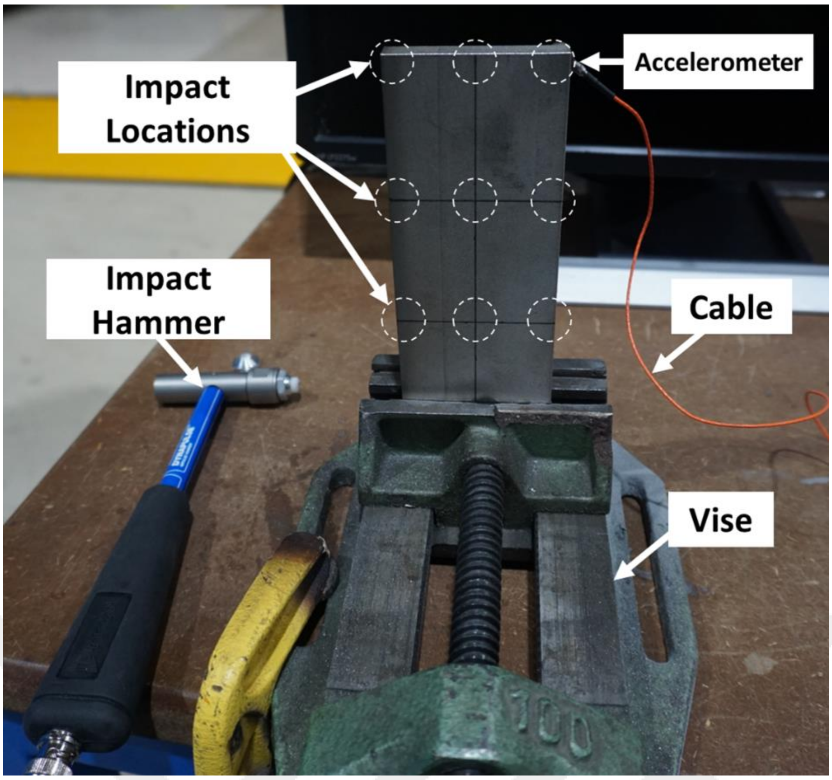

Figure 2.11 : Clamped-free test setup for 1st DoE.

The free-free experimental setup depicted in Fig. 2.12a was utilized to extract the damping ratio of the specimens. This setup comprised of a specimen, foam-based supports, an impact hammer, an accelerometer, and a signal acquisition module. To measure frequencies, the impact hammer was utilized to stimulate the specimens at various points along their surfaces, while the ensuing vibrations were gauged using the accelerometer and recorded using the signal acquisition device and computer. This methodology was employed to accurately determine the damping ratio of the specimens.

To provide the free-free boundary condition, a soft foam (sponge) was used and the contact area between the soft foam and the test samples was minimized (approximately 5% of the total surface area of the specimens) to prevent damping from the ground. The excitation was ensured via an impact hammer (Dytran Dynapulse 5800B4), and the corresponding response of the system was measured using an accelerometer (Dytran 3225F1). To collect the impact and response data, National Instruments NI USB-4431 dynamic signal acquisition module was used during the experiments, and frequency resolution and the sampling rate were set as 0.5 Hz and 102,400 Hz, respectively.

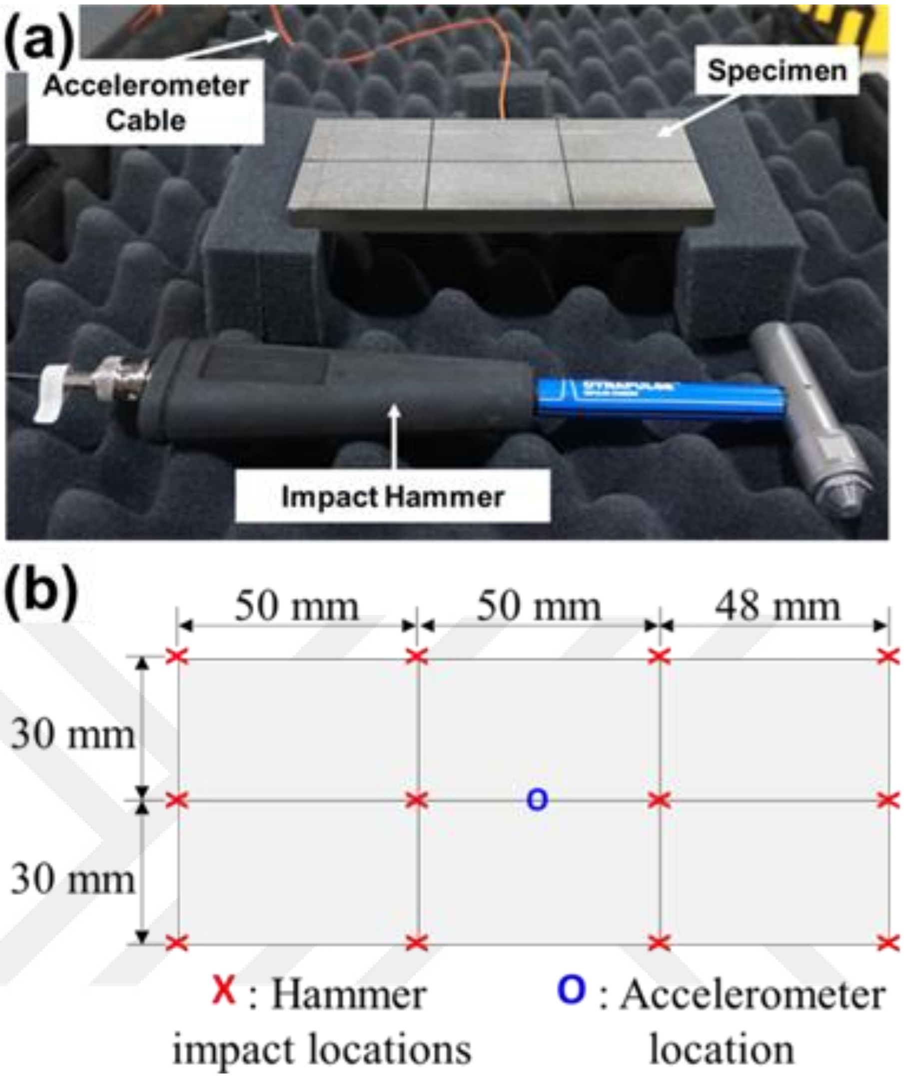

Figure 2.12 : Free-free test setup for 1st DoE.

In order to enhance the precision of the investigation, Fig. 2.12b displays twelve marked points indicated with cross symbols, which were identified during the hammer impact excitation. The results obtained from these twelve points are averaged in investigating the effect on the damping behavior of the specimens. The experimental setup involved the application of a minimum of five impacts to each point during testing to obtain reliable data. The data was then used to calculate the frequency response functions (FRFs). The frequency range of 0 – 4,000 Hz was determined to cover the initial two natural frequencies of the specimens, and FRFs were obtained for each specimen within this range to calculate damping ratios.

A new test was conducted on Specimen 5 in the 1st DoE by emptying the powder as shown in Fig. 2.13. Due to issues encountered in the previous test setup, an alternative setup was established, and measurements were taken. In this setup, a Dytran 3255A accelerometer and a PCB Piezotronics 086E80 impact hammer were used, along with DEWE 43 A for data processing. The impact points are shown as indicated in 2.12 (b).

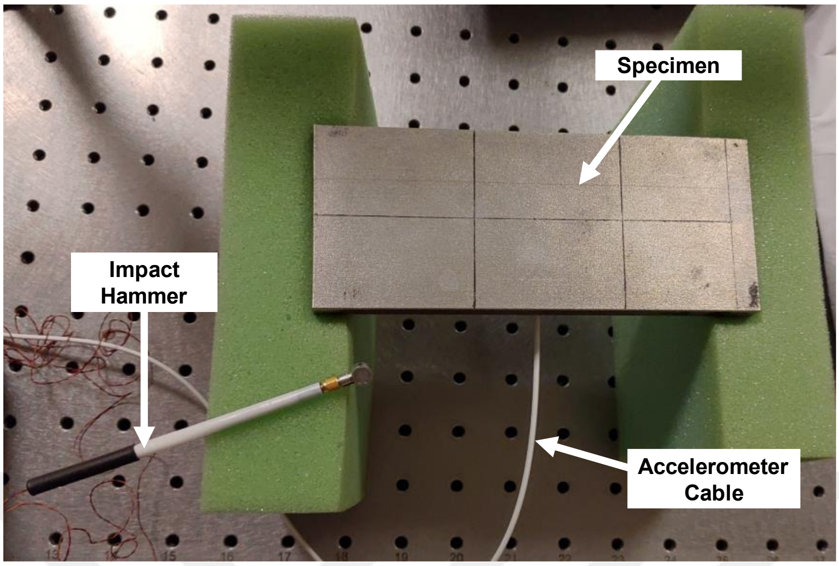

Figure 2.13 : Free-free test setup for Emptied Specimen 5 in 1st DoE.

When the clamped-free results could not be obtained appropriately for the 1st DoE, tests were conducted in the 2nd DoE without separating the specimens from the build plate first. The purpose here was to eliminate noise by leaving a bulk mass at the bottom. Thus, both clamped-free and free-free results were obtained to observe the behavior of the damping performance according to boundary conditions. The relevant test setups are provided in the Fig. 2.14, respectively, for clamped-free and free-free configurations.

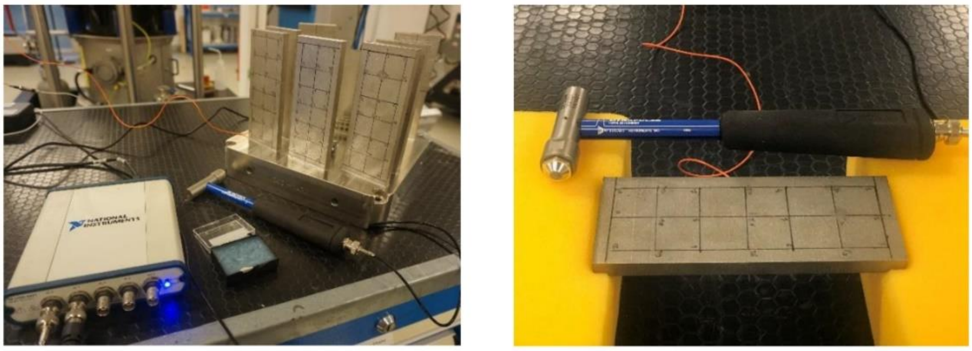

(a) **(b)**

Figure 2.14 : a) Clamped-free and b) Free-free modal test setups for 2nd DoE.

In order to achieve consistent outcomes by delivering equivalent impacts, the samples were stimulated from the nine locations depicted in Fig. 2.15 using an impact hammer for both clamped-free and free-free tests. An accelerometer was placed at the center of the back face of the specimens to measure the accelerations. The same devices used in the 1st DoE test were also used in this study. The natural frequencies and damping ratios of all specimens for the first mode are reported in this study to evaluate the effects of the particle damper.

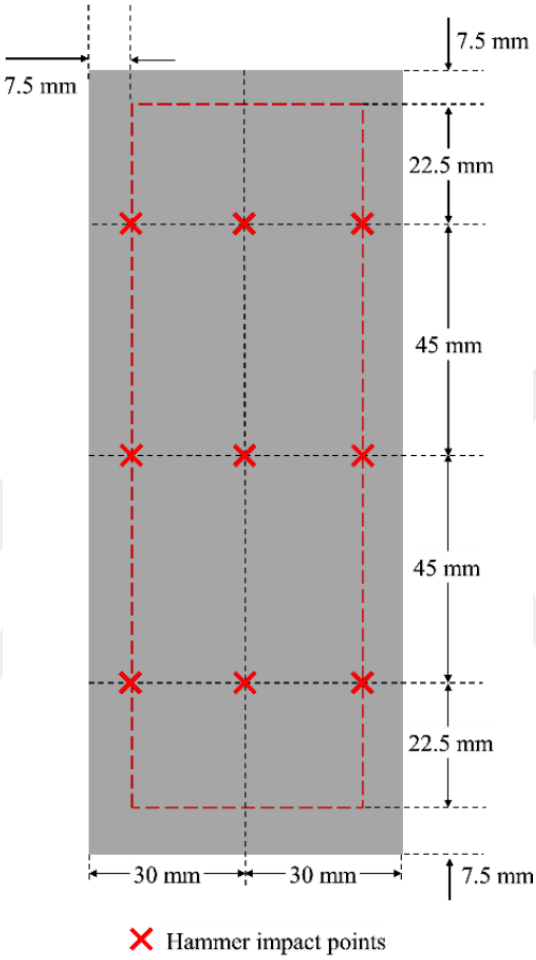

Figure 2.15 : Excitation points on specimens.

2.4.1 Step by step post-processing of the test data

In this section, the post-processing of a arbitrarily chosen analysis of the fully fused component is described step by step, explaining how the data provided in the Results section were obtained.

Firstly, as shown in Fig. 2.16, measurement results are collected in a single folder along with the files modal_parameter.m, orthogonal.m, and rfp.m. The relevant codes are provided in the attachment. The important aspect here is not the file extension but the content of the results. The first column represents frequency, and the second and third columns represent the real and imaginary parts of the magnitude, respectively.

Name

- HB1.frf
- HB2.frf
- HB3.frf
- HD1.frf
- HD2.frf
- HD3.frf
- HM1.frf
- HM2.frf
- HM3.frf
- HT1.frf
- HT2.frf
- HT3.frf
- modal_parameter.m
- orthogonal.m
- rfp.m

HD3.frf

1	0.000000e+000	3.862351e-001	-0.000000e+000
2	5.000000e-001	9.315198e-002	2.489220e-002
3	1.000000e+000	-3.028608e-002	-4.044757e-003
4	1.500000e+000	-2.177025e-004	-3.218694e-003
5	2.000000e+000	-5.662540e-003	-5.549001e-005
6	2.500000e+000	-1.811429e-003	1.489771e-003
7	3.000000e+000	1.975211e-004	1.286110e-003
8	3.500000e+000	1.078361e-004	2.921277e-004
9	4.000000e+000	1.140779e-003	7.302079e-004
10	4.500000e+000	4.733007e-004	1.707792e-004
11	5.000000e+000	-4.261900e-005	1.947846e-004
12	5.500000e+000	4.164785e-004	3.540444e-004
13	6.000000e+000	8.832621e-004	1.407735e-004
14	6.500000e+000	7.834753e-004	-1.103586e-005
15	7.000000e+000	9.095236e-004	-5.713361e-005
16	7.500000e+000	1.056935e-003	-1.737174e-005
17	8.000000e+000	1.384514e-003	-2.966826e-004
18	8.500000e+000	1.833493e-003	-8.349730e-004
19	9.000000e+000	2.030007e-003	-2.130387e-003

Figure 2.16 : Required folder format.

Next, using a program that can open files with the .m extension, such as MATLAB or Octave, the modal_parameter.m file is opened. In this study, GNU Octave 7.3.0 was used and some rows are modified as shown in Fig. 2.17.

modal_parameter.m

```
1  clear all;
2  clc;
3
4  %Inputs
5  % user has to play with beginning and ending frequency to get a good fit
6  freqst=0;% beginning frequency
7  freqen=4000; % end frequency
8  no_modes=2;
9  S=load('HD3.frf'); % load frf data
10 deltaf=(S(2,1,1)-S(1,1,1));% delta frequency
11 omega=S(1+round(freqst/deltaf):1+round(freqen/deltaf),1);
12 rec=S(1+round(freqst/deltaf):1+round(freqen/deltaf),2)+1i.*S(1+round(freqst/deltaf):1+round(freqen/deltaf),3);
13
14 error=zeros(no_modes,1);
15
16 for N=1:no_modes
17     [alpha,modal_par]=rfp(rec,omega,N);
18     error(N)=sum((abs(rec-alpha')));
19 end
20
21 [Y,I]=min(error);%find min error place
22 [alpha,modal_par]=rfp(rec,omega,I);%rerun alpha with min error
23
24 close all;
25 figure(1);
26 semilogy(omega,abs(rec))
27 hold on
28 semilogy(omega,abs(alpha),'r')
29 title('HD3 - First Two Modes','FontSize', 18)
30 xlabel('Frequency [Hz]','FontSize', 18)
31 ylabel('Magnitude X/F-[m/N]','FontSize', 18)
32 legend('Measurement','Curve Fit','FontSize', 18)
33 set(gca,'fontsize',18)
```

Figure 2.17 : Modified parts of code.

In this file, first, the name of the desired result file is provided on line 9. In this particular study, it was possible to capture the first two modes within the 0-4000 Hz range, and the other results were not read due to their high coherence values. Therefore, the exact positions of the first two modes can be observed by limiting the analysis to this 0-4000 Hz range in lines 6 and 7. Although increasing the value in the "number of modes" part on line 8 may result in a better-fitting curve, it also makes it more challenging to determine the actual mode. Obtaining the most accurate result with the minimum number of modes yields more reliable results. Fitting the curve to each mode individually allows for this approach. This is addressed in the subsequent figures.

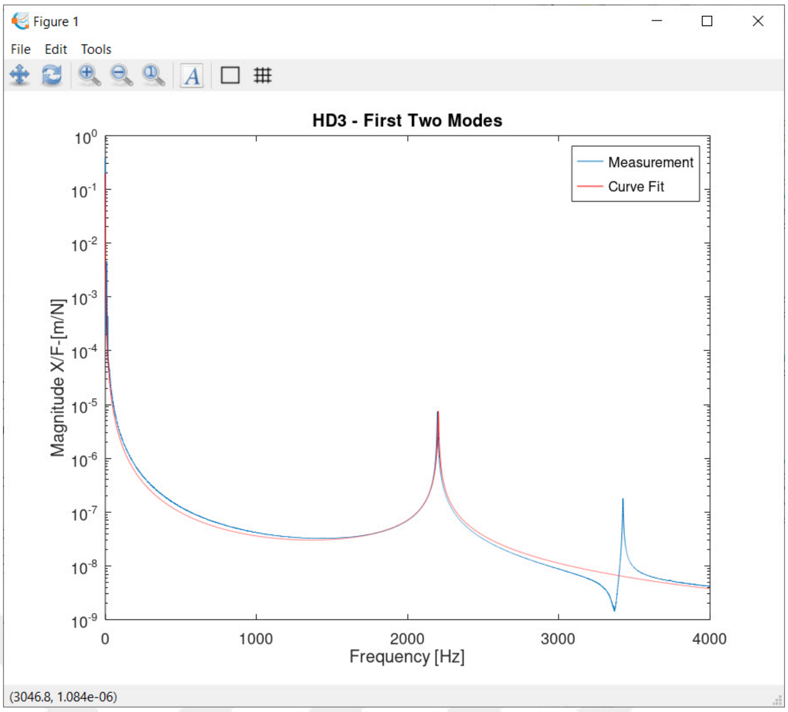

Figure 2.18 : Raw data and fitted curve on first two mode.

As shown in Fig. 2.18, even though the number of modes was set to 2, the second mode was not captured effectively. However, from this graph, it was determined that the first mode is within the range of 2100 to 2300 Hz, while the second mode is within the range of 3000 to 4000 Hz. By fitting the curve to each mode individually, a better curve fit can be obtained. Initially, for the first mode, lines 6 and 7 were updated as shown in Fig. 2.19, and Fig. 2.20 was obtained.

```
modal_parameter.m
1  clear all;
2  clc;
3
4  %Inputs
5  % user has to play with beginning and ending frequency to get a good fit
6  freqst=2100;% beginning frequency
7  freqen=2300; % end frequency
8  no_modes=2;
9  S=load('HD3.frf'); % load frf data
10 deltaf=(S(2,1,1)-S(1,1,1));% delta frequency
11 omega=S(1+round(freqst/deltaf):1+round(freqen/deltaf),1);
12 rec=S(1+round(freqst/deltaf):1+round(freqen/deltaf),2)+1i.*S(1+round(freqst/deltaf):1+round(freqen/deltaf),3);
13
14 error=zeros(no_modes,1);
15
16 for N=1:no_modes
17     [alpha,modal_par]=rfp(rec,omega,N);
18     error(N)=sum((abs(rec-alpha')));
19 end
20
21 [Y,I]=min(error);%find min error place
22 [alpha,modal_par]=rfp(rec,omega,I);%rerun alpha with min error
23
24 close all;
25 figure(1);
26 semilogy(omega,abs(rec))
27 hold on
28 semilogy(omega,abs(alpha),'r')
29 title('HD3 - First Mode','FontSize', 18)
30 xlabel('Frequency [Hz]','FontSize', 18)
31 ylabel('Magnitude X/F-[m/N]','FontSize', 18)
32 legend('Measurement','Curve Fit','FontSize', 18)
33 set(gca,'fontsize',18)
```

Figure 2.19 : Modified parts of code to capture the first mode.

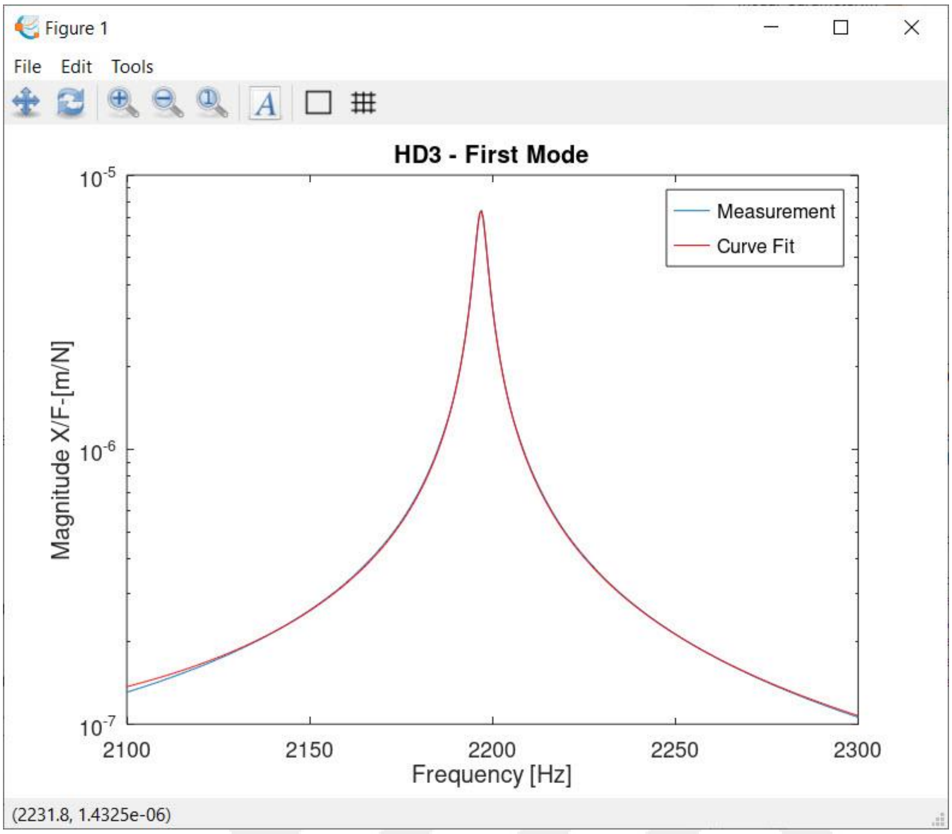

Figure 2.20 : Fitted curve for the first mode.

Once it is ensured that the curve in Fig. 2.20 fits well, the modal parameters become extractable. If it is believed that the curve does not fit well, the number of modes and frequency values, i.e., lines 6, 7, and 8, can be revised appropriately to search for a better result. In this visualization, it is concluded that the result is sufficiently good, and the result is obtained from here. Thus, the frequency and damping ratio values can be read from the modal_par matrix.

modal_par [2x4 double]

	1	2
1	2066.9	0.01631
2	2196.8	0.00071254

Figure 2.21 : First column is frequency and second column is damping ratio.

Since the number of modes was chosen as two, two results are obtained as in Fig. 2.21. However, it is clearly seen from the graph that the primary root is around 2200 Hz. Therefore, the second line result, which corresponds to the first mode, is obtained as 2196.8 Hz, and the damping ratio for the first mode is 7.1e-4. The following images

(Fig. 2.22 – Fig. 2.24) also demonstrate that the same result is achieved for the second mode. The method is the same for this part as well.

modal_parameter.m

```
clear all;
clc;

%Inputs
% user has to play with beginning and ending frequency to get a good fit
freqst=3000;% beginning frequency
freqen=4000; % end frequency
no_modes=2;
S=load('HD3.frf'); % load frf data
deltaf=(S(2,1,1)-S(1,1,1));% delta frequency
omega=S(1+round(freqst/deltaf):1+round(freqen/deltaf),1);
rec=S(1+round(freqst/deltaf):1+round(freqen/deltaf),2)+1i.*S(1+round(freqst/deltaf):1+round(freqen/deltaf),3);

error=zeros(no_modes,1);

for N=1:no_modes
    [alpha,modal_par]=rfp(rec,omega,N);
    error(N)=sum((abs(rec-alpha')));
end

[Y,I]=min(error);%find min error place
[alpha,modal_par]=rfp(rec,omega,I);%rerun alpha with min error

close all;
figure(1);
semilogy(omega,abs(rec))
hold on
semilogy(omega,abs(alpha),'r')
title('HD3 - Second Mode','FontSize', 18)
xlabel('Frequency [Hz]','FontSize', 18)
ylabel('Magnitude X/F-[m/N]','FontSize', 18)
legend('Measurement','Curve Fit','FontSize', 18)
set(gca,'fontsize',18)
```

Figure 2.22 : Modified parts of code to capture the second mode.

For the second mode, the frequency and damping ratio values were obtained as 3423.9 Hz and 5.0e-4, respectively. However, these values are only obtained from the results of a single test point.

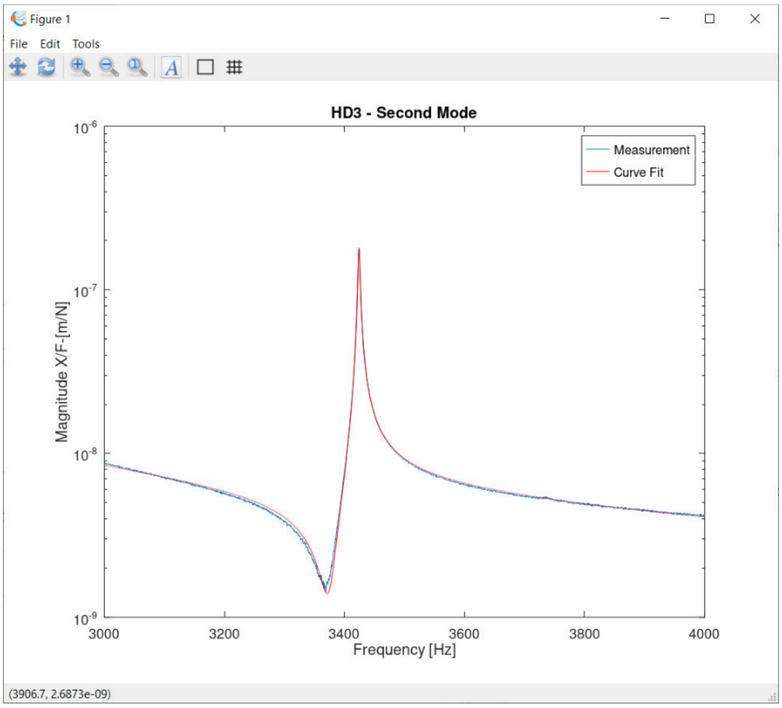

Figure 2.23 : Fitted curve for the second mode.

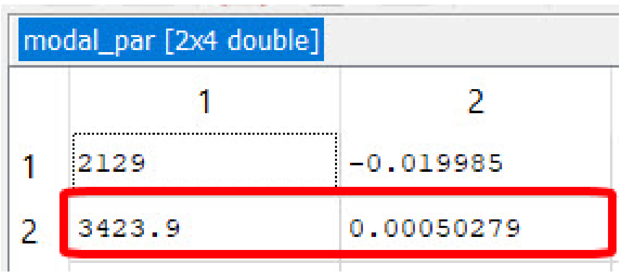

modal_par [2x4 double]

	1	2
1	2129	-0.019985
2	3423.9	0.00050279

Figure 2.24 : First column is frequency and second column is damping ratio.

The same procedures were repeated for 12 test points in the first DoE and 9 test points in the second DoE, and the average values are provided in the results section.

2.5 Methods of Analysis

The Frequency Response Function (FRF) describe the relationship between input and output signals in linear systems and are important for understanding the system's dynamic behavior. They are calculated as the ratio of output to input Fourier components, but approximations are used in practice. FRFs are only available at virtual harmonic frequencies where continuous input signals are applied [76]. FRF is a function that has both real and imaginary components and is defined across a range of frequencies. Curve fitting is typically utilized as a means of extracting information from measurements of this nature.

A complex mathematical expression (2.1) is obtained when displacement (mm) is used as the response parameter for FRF, which includes both magnitude and phase components. The magnitude component, which is calculated using expression (2.2), is used for analysis output purposes [77].

$$H(\omega) = a(\omega) = \frac{1}{(k - \omega^2 m) + i(\omega c)} \tag{2.1}$$

$$|a(\omega)| = \frac{|X|}{|F|} = \frac{1}{\sqrt{(k - \omega^2 m)^2 + (\omega c)^2}} \tag{2.2}$$

In the equation, the displacement represented by " X ", force by " F " dynamic flexibility by " a ", rigidity by " k ", frequency by "ω", mass by " m ", and damping constant by " c " for a system. If velocity is used instead of displacement, equation 2.1 becomes 2.2 and equation 2.5 becomes 2.6 [77].

$$x(t) = Xe^{i\omega t} \tag{2.3}$$

$$v(t) = \dot{x}(t) = Ve^{i\omega t} = i\omega Xe^{i\omega t} \tag{2.4}$$

$$Y(\omega) = \frac{V}{F} = i\omega \frac{X}{F} = i\omega\ a(\omega) \tag{2.5}$$

$$|Y(\omega)| = \omega |a(\omega)| \tag{2.6}$$

The term "mobility" is used to refer to the expression $Y(\omega)$. Similarly, when acceleration is taken as the response parameter, the expression $A(\omega)$ represents inertance [77].

$$a(t) = \ddot{x}(t) \tag{2.7}$$

$$A(\omega) = \frac{A}{F} = -\omega^2 a(\omega) \tag{2.8}$$

In addition to these calculations, the Rational Fraction Polynomial (RFP) method, which is able to be used to curve fitting to the FRFs in order to determine modal parameters of the most significant vibration modes of the specimens [78]. Hence, in the first step, the RFP method, which is a technique that uses a complex function valued within a user-defined frequency [79], was used to fit a curve on test data for each FRF measurement and obtain the corresponding natural frequencies and calculate the damping ratios. The rational fraction form is a mathematical expression that contains two polynomials with independent orders for the numerator and denominator. The characteristic polynomial, which forms the denominator of the transfer function, has roots that correspond to the points where the transfer function approaches infinity, also known as the poles of the transfer function [79]. On the other hand, the roots of the numerator polynomial correspond to the zeros of the transfer function where it becomes zero. To determine the poles and zeros of the transfer function, the rational fraction form is fitted to frequency response function data using equation 2.9, and then the roots of both polynomials are solved for [79].

$$H(\omega) = \left. \frac{\sum_{k=0}^{m} a_k s^k}{\sum_{k=0}^{n} b_k s^k} \right|_{s=j\omega} \tag{2.9}$$

The coefficients for the numerator and denominator polynomials, represented as $(a_k, k = 0, \dots, m)$ and $(b_k, k = 0, \dots, n)$, respectively, are solved for in order to obtain the rational fraction form. The variable s, which is a complex number typically denoted as the Laplace variable, is used to evaluate the transfer function [79]. This method applied with a MATLAB code which is given in appendix.

Then, in the second step, the overall acceleration function's root-sum-square (RSS) is calculated up to 4,000 Hz to quantify the average vibration amplitude of the specimens. This method is a statistical method used for combining uncertainties from multiple sources into a single, overall uncertainty value [80]. This method is commonly used in engineering and science to estimate the overall uncertainty of a measurement or calculation based on the uncertainties associated with individual measurements or parameters. The RSS method has found extensive application in diverse areas, including aerospace, chemistry, physics, and metrology. In this study, acceleration data was collected from various points on beams as stated above and the dynamic behavior of the parts within 0 – 4,000 Hz was evaluated and compared with each other and to the fully fused model using the following equations:

$$A(\omega) = \sum_{i=1}^{N} a_i(\omega) \tag{2.10}$$

$$RSS = \sqrt{\sum_{i=0}^{4000} A(\omega_i)^2} \tag{2.11}$$

Here, N is number of measured values, ω is frequency, a is acceleration measured from accelerometer at a specific natural frequency, and A is sum of measured a values.

3. RESULTS AND DISCUSSION

3.1 Determination of Particle Mass and Packing Density

Before discussing the results of the study, it is important to understand the two types of density that were measured. The first is true density, which refers to the actual density of a material, taking into account any internal voids or cavities. True density (or bulk density) is calculated by dividing the mass of the material by its true volume. The second type of density measured in this study is tapped density as shown in Fig. 3.1. Tapped density is a measure of the density of a powder material when it is packed or settled into a container. It is determined by tapping or vibrating the container and measuring the change in volume or mass of the material as it becomes more compacted. Both true density and tapped density are important measures of the powder properties and can provide valuable information for understanding its behavior in different applications. In the context of the study discussed here, both types of density were used to gain insight into the impacts of integrated cavities on the mechanical properties of an additive manufactured structure.

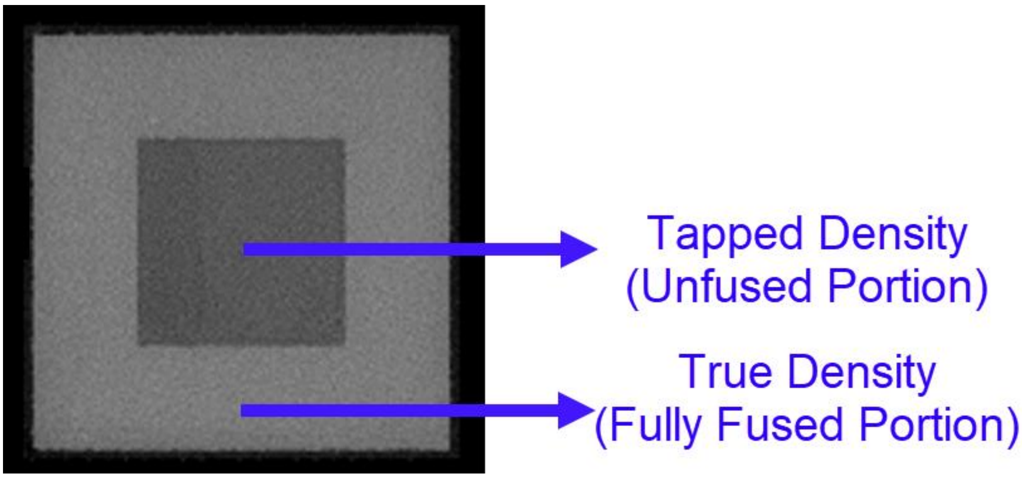

Figure 3.1 : True density & tapped density definitions on computed tomography can view from study of Ehlers et al. [12].

For the 1st DoE, the fully fused beam has an outer volume of 88.8 cm^3 and a mass of 731 g, resulting in a true density of 8.232 g/cm^3. This value is slightly higher than the density provided by Praxair's additive powder datasheet, which is 8.2 g/cm^3. For the

2^{nd} DoE, the fully fused beam has an outer volume of 90 cm3 and a mass of 737 g, resulting in a true density of 8.183 g/cm^3.

The tapped density of the powder bed was determined to be 4.511 g/cm^3 at the locations of the cavities for 1^{st} DoE, which is lower than the 5.0 g/cm^3 density stated in Praxair's additive powder datasheet. This means that the relative density of the structure was calculated to be around 55%, based on the calculated true and tapped densities. This density was calculated as 4.58 g/cm^3 for 2^{nd} DoE and ratio is 56%.

The observation that the body-integrated cavity increment of the specimen reduced its mass compared to the fully fused structure, resulting in a lower relative density, has significant implications for industries that rely on lightweight yet durable materials, such as aerospace. Ultimately, this knowledge can lead to the creation of stronger, more lightweight, and efficient products.

3.2 Results of Tests and Analysis for 1^{st} DoE

In this section, the examination and analysis outcomes of the investigation are displayed. More precisely, by utilizing the RFP technique, a comprehensive evaluation of the measured FRFs led to the determination of the natural frequencies and damping ratios of the initial two modes. All FRF graphs are given in appendix. To ensure accurate and reliable results, the investigation was conducted using the test matrix provided in Table 3.1. Furthermore, in addition to the natural frequencies and damping ratios, mode shapes for the first two modes were also generated through detailed analysis. These mode shapes provided valuable insights into the dynamic behavior of the system and helped to identify any potential issues or areas for improvement. Overall, the results of the analysis presented in this section are critical for understanding the dynamic behavior of the system under investigation. This information is able to be utilized to optimize the system's performance, improve its reliability, and ensure that it operates safely and efficiently under a wide range of operating conditions.

The fully-fused specimen was tested to determine the first two natural frequencies and damping ratios, which were then compared with those of PD integrated structures to assess the effectiveness of PDs. Specifically, the analysis aimed to get results of the first and second modes. The results of the analysis revealed that the first mode of the structure had a natural frequency of 2,197 Hz, while the second mode had a natural frequency of 3,424 Hz. Additionally, the damping ratios for these modes were measured as and 7.1×10^{-4} and 5.0×10^{-4} respectively.

The comparisons are presented in Fig. 3.3 – 3.5 and detailed descriptions of these are ensured in the subsequent sections. The study showed that specimen 1 had the highest damping ratio for the first mode is 7.7×10^{-3} (see Fig. 3.3a), and specimen 2 had the highest damping ratio for the second mode is 4.7×10^{-3} (refer to Fig. 3.3b). Significant improvements in damping ratios were observed when using PDs.

Damping ratios for the first mode and second mode using PDs were found to reach up to 10.8 times and 9.4 times, respectively, when compared to fully fused specimens. These findings are presented in Table 3.1. Therefore, PDs can lead to substantial improvements in damping ratios, which are useful in engineering applications where vibration control is critical. The study's results have significant implications for designing and constructing structures that require enhanced damping capabilities.

As mentioned earlier, the FEA provided information about the first two natural frequencies of the specimen, as well as their corresponding bending and torsional mode shapes. However, it was observed that there were slight variations in the predicted natural frequencies compared to the actual experimental values. This could be attributed to the approximations made during the numerical modeling process. For instance, when considering the fully fused specimen, the FEA predicted the first two natural frequencies to be 2,331 Hz and 3,339 Hz, respectively. However, these values had discrepancies of 6.1% and 2.5% when compared to the values obtained through experimentation.The FRFs can be used to extract information about the dynamic properties of the specimens, such as their natural frequencies, damping ratios, and mode shapes. The RSS values, on the other hand, provide an indication of the overall response of the specimens in the frequency range of interest, allowing for a comprehensive evaluation of their performance. Table 3.1 presents the experimental data for all the specimens containing PDs, including the RSS values besides to natural frequencies and damping ratios of the measured FRFs. The frequency range for the calculation of the FRFs was set between 0 and 4,000 Hz, which covers the first two modes. These results are significant in identifying the behavior of the specimens under test and analyzing the impact of the PDs on their performance.

Table 3.1 : Experimentally identified modal parameters of the specimens and the RSS values of the calculated FRFs.

Parameter	1st Mode Frequency (Hz)	1st Mode Damping Ratio	2nd Mode Frequency (Hz)	2nd Mode Damping Ratio	RSS from Experiment (0 - 4000 Hz)
0 (Fully Fused)	2,197	7.1e-4	3424	5.0e-4	0.036
1	2,201	7.7e-3	3340	3.1e-3	0.060
2	2,207	6.4e-3	3294	4.7e-3	0.039
3	2,238	5.3e-3	3321	7.7e-4	0.034
4	2,168	3.1e-3	3424	2.0e-3	0.043
5	2,204	3.3e-3	3373	5.2e-4	0.032
6	2,218	2.4e-3	3437	1.3e-3	0.033
7	2,139	5.8e-3	3317	2.3e-3	0.051
8	2,111	4.7e-3	3396	3.0e-3	0.051
9	2,202	7.1e-3	3339	2.4e-3	0.045
10	2186	4.7e-3	3342	8.4e-4	0.035
11	2196	2.6e-3	3432	1.8e-3	0.032
12	2175	2.9e-3	3453	1.5e-3	0.038
13	2149	4.3e-3	3337	1.8e-3	0.037
14	2178	4.3e-3	3436	3.2e-3	0.029
15	2203	4.8e-3	3373	1.7e-3	0.038
16	2145	4.6e-3	3376	3.8e-3	0.038

The PDs reduces the displacement amplitudes, and thus the RSS values will decrease around the natural frequency regions. However, considering the whole frequency range up to 4,000 Hz, the RSS value may increase in the other regions of the measured FRFs as shown in Table 3.1 since the stiffness of the specimens is also decreasing with PDs. This phenomenon can be observed from Fig. 3.2 that shows the measured FRFs of the fully fused specimen and specimen 14 which shows the lowest RSS.

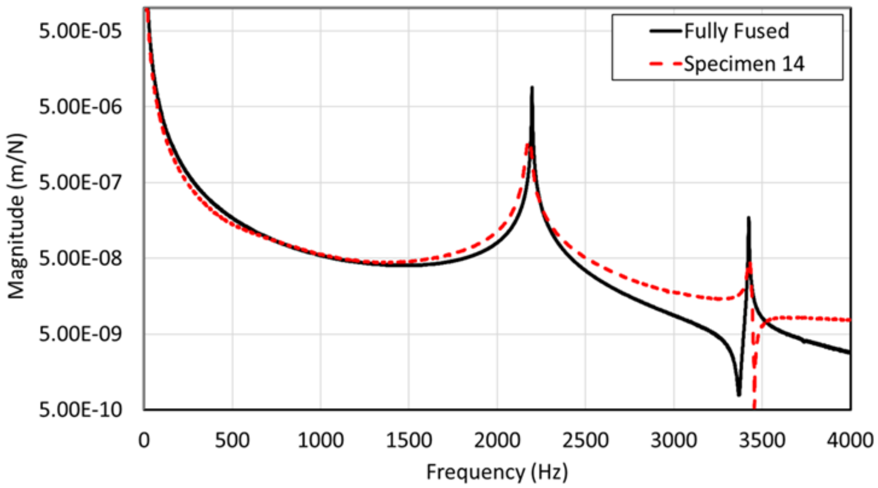

Figure 3.2 : FRF comparison of fully fused beam and specimen 14.

These results provide critical insights into the dynamic behavior of the fully-fused specimen under various operating conditions. They are essential for understanding the system's behavior and can be used to optimize its performance, improve its reliability, and ensure that it operates safely and efficiently and they provide a foundation for more in-depth investigations and can be used to guide future research efforts in this area.

One key finding from this research is that the damping performance of PDs is heavily influenced by several factors, including the volume fraction, location, and number and length of the dampers. In particular, studies have shown that increasing the volume fraction of PDs in a given host material leads to a corresponding increase in damping ratios, as illustrated in Fig. 3.3.

Another crucial element that influences the damping performance of PDs is the location of the dampers within the host material. As shown in Fig. 3.4, the damping ratios for both the first two modes of vibration are significantly influenced by the location of the PDs. Specifically, dampers located closer to the center of the main body exhibit higher damping ratios for the first mode, while dampers located near the tip regions perform better for the second mode.

The number and length of PDs are also important considerations when designing and implementing these dampers. Studies have found that increasing the number of PDs can lead to improved damping performance, although there may be diminishing returns beyond a certain point. Similarly, increasing the length of the PDs can also improve their damping capabilities, but there may be practical limitations to how long these dampers can be.

Overall, these findings underscore the importance of carefully considering the various parameters that affect the performance of PDs. By taking these factors into account, engineers and designers can optimize the damping capabilities of these materials for a wide range of applications. Details discussions of these results in terms of the impact of parameters (such as volume fraction, location, number and length of PDs) are given in the following sections.

3.2.1 Size effect of the unfused cavities

The size effect of the PDs was examined using the LEN 1 – 4 groups of specimens. The specimens were grouped in a way that the location/region and the number of PDs were kept similar. The damping ratios for the first two modes of all specimens are shown in Fig. 3.3.

The findings reveal that the damping ratios obtained from specimens 1, 2, 8, and 9 were comparatively higher than the other specimens within their respective groups, mainly due to the presence of PDs with high volume fractions. This implies that as the volume fraction of PDs decreases, the damping performance for the first two modes also declines. Furthermore, the extent of reduction in damping ratios, in relation to changes in the volume fraction, is influenced by the regions covered by the PDs. These regions can affect the way the PDs interact with the surrounding material, leading to variations in the damping response which shows that these variations are also influenced by the mode shape profile of the specimens.

It is worth noting that the alignment between the PDs and the mode shape profile is critical in optimizing the damping performance of structures. This is because PDs are designed to dissipate energy by applying forces that are proportional to the velocity of the structure's motion. Therefore, if the PDs are not aligned correctly with the mode shape, the damping effect may not be fully utilized.

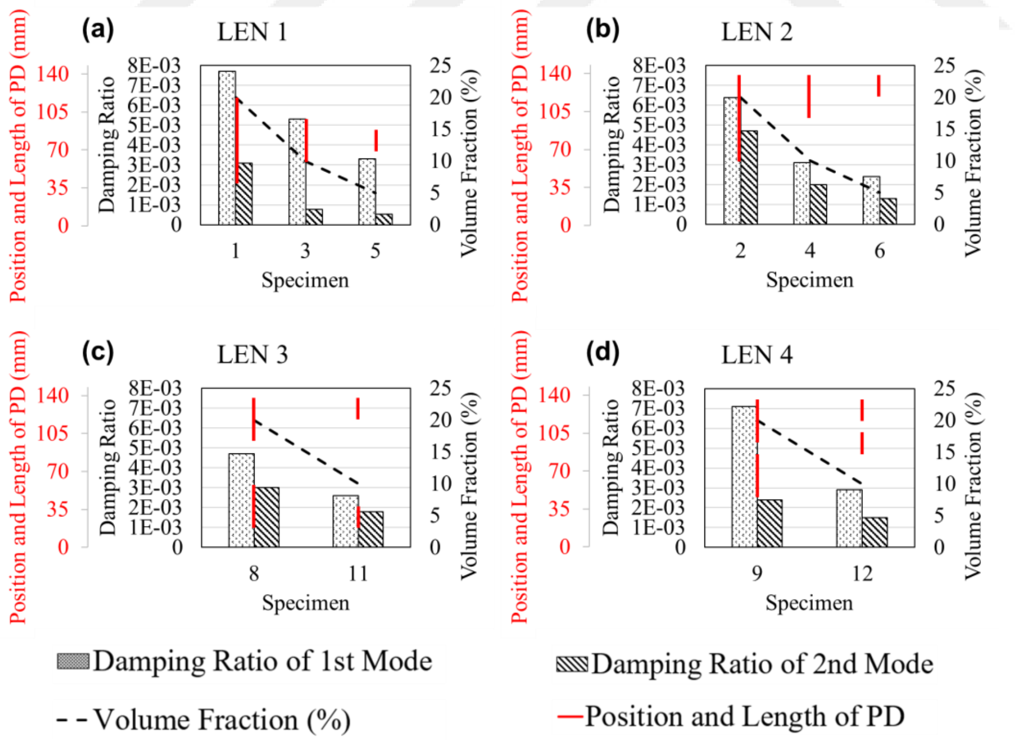

Figure 3.3 : Effect of length of particle dampers (a) LEN 1, (b) LEN 2, (c) LEN 3 and (d) LEN 4. Red lines represent the cavity length and location for illustration purposes to compare the data clearly.

In addition, the results presented in Fig. 3.3a show that the effectiveness of PDs in damping the vibration modes depends on their length. As the length of the PD enhances, the probability of it coinciding with the maximum deformation region of the mode also increases, resulting in better damping performance. However, the degree of improvement in damping performance varies depending on the location of the PD within the structure. For example, as seen in Fig. 3.3a, the damping performance for the first mode decreases significantly as the length of the PD decreases.

These results have significant suggestions for the design of damping systems for structures, particularly for applications that involve complex vibration modes. It is crucial to carefully consider the placement and length of PDs to ensure that they are aligned correctly with the mode shape profile, and to optimize the damping performance of the structure. By doing so, it is possible to minimize the damage caused by vibrations and improve the durability of structures, ultimately leading to safer and more efficient designs.

3.2.2 Location effect of the unfused cavities

The effectiveness of PDs is heavily dependent on their location and placement within a given structure. To better understanding of this phenomenon, six distinct groups (LOC 1 – 6) were formed and conducted a comprehensive analysis of the results. The findings, which are presented in Fig. 3.4, shed light on the significance of the placement of PDs in relation to specific regions within the beam. This study proved that the location of PDs within a beam plays a critical role in their efficacy. Specifically, for the first mode, PDs that were placed closer to the center region of the beam proved to be more effective. Conversely, PDs placed nearer to the tip regions demonstrated a higher efficacy for the second mode. These results can be attributed to the unique deformation profiles of the mode shapes, as discussed in the preceding section.

Recalling Fig. 2.9, the displacement of the middle section of the specimen is higher for the first bending mode and the displacement of the tip regions are higher for the second mode. Hence, as previously discussed, the displacement of the middle section of the specimen is greater for the first bending mode, while the displacement of the tip regions is more significant for the second mode. This phenomenon is able to be defined by the unique deformation profile of each mode shape. Given this information, it becomes clear that PDs placed at the tip regions of a structure would be more effective at increasing damping for the second mode.

This is supported by our results, as demonstrated by the comparison of LOC 1-3 in Fig. 3.4a-c. In contrast, for the first mode, PDs located closer to the center region of the beam were found to be more effective in increasing damping which can be also observed in same figures.

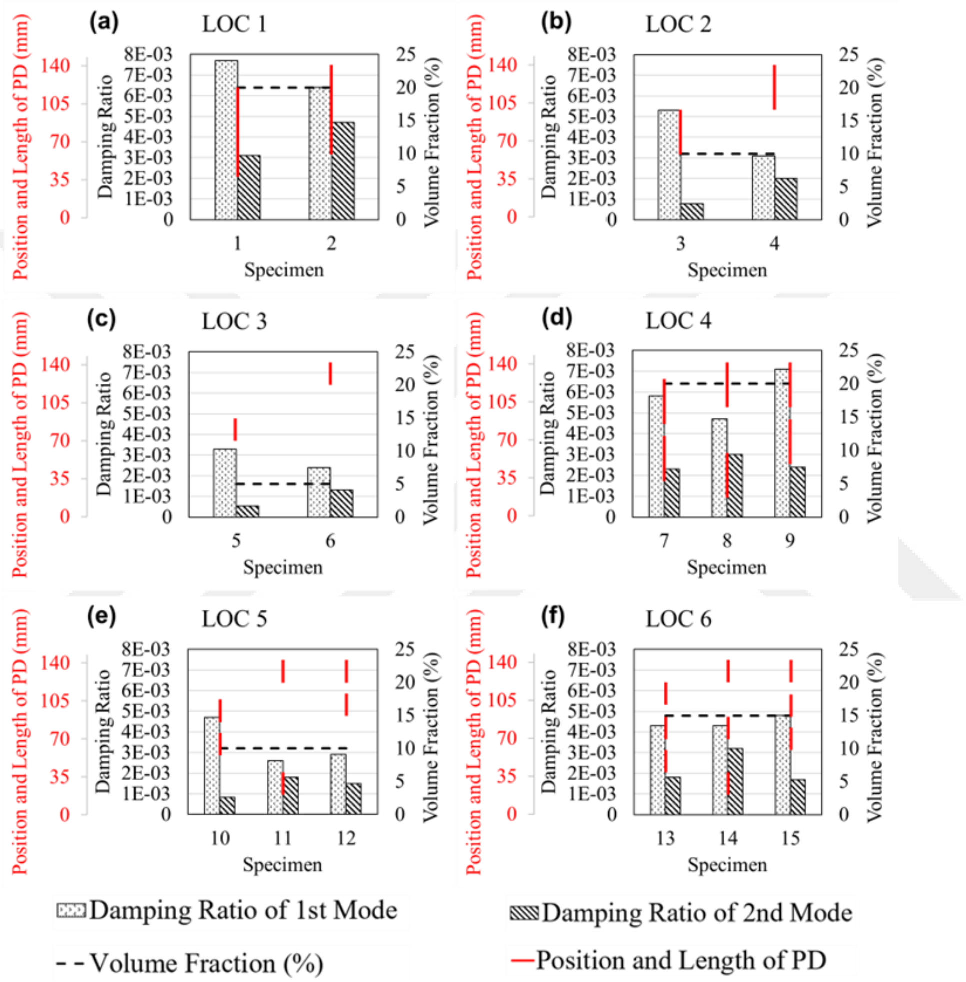

Figure 3.4 : Effect of the dampers on different mode shapes (a) LOC 1, (b) LOC 2, (c) LOC 3, (d) LOC 4, (e) LOC 5 and (f) LOC 6. Red lines represent the cavity length and location for illustration purposes to compare the data clearly.

Hence, it was showed that the presence of PDs located at the tips effectively increases the damping for the second mode, which is evident when comparing the results of LOC 1 – 3, as showed in Fig. 3.4a-c.

In the existence of multiple PDs in the structure (LOC 4 – 6 groups), the results are presented in Fig. 3.4d-f. LOC 4 and LOC 5 include two PDs, and LOC 6 specimens have 3 PDs along the length of the beams. Similar to the results obtained for beams having a single PD, the location is the most critical factor for improving damping of a specific mode. The intersection of PDs with the maximum displacement regions of modes is also crucial for optimal damping performance. When PDs intersect with the maximum displacement region, their effectiveness in reducing vibrations is increased. Conversely, if there are regions of maximum displacement that are not covered by dampers, the damping performance may be reduced.

For instance, considering the specimens listed in LOC 4, specimen 8 has PDs both around the tip regions; thus, the damping ratio of the second mode is the highest in this group with a value of 3.0×10^{-3}. However, specimen 9 has the best performance for the first mode since one of the PD locations is well aligned with the high deformation zone of the first mode. In the case of specimen 7, despite the PDs being located near the center, their damping performance is inferior to that of specimen 9. This is because there is a gap between the two PDs, which intersect with the maximum displacement region for the first mode. Thus, statemens above could be observed on these results.

Also for the PDs of specimens in groups LOC 4 and LOC 5 are similarly dispersed in the main body. It might have been expected that the damping performance order of LOC 5 specimens for the first mode would be similar to LOC 4, with a descending order of damper performances for specimens 10, 12, and 11, given the similar-looking PD locations. However, there are differences observed between the two groups. The PDs in LOC 5 are shorter in length than those in LOC 4, which causes them to miss some of the maximum displacement regions and reduces their damping performance. Consequently, a descending order of specimens 12, 10, and 11 was observed for the damping performance of the first mode in LOC 5.

Finally, LOC 6 specimens once again showed that the fact that PDs positioned at the center are more effective in the first mode and those placed at the tip(s) are more effective in the second mode.

From the results of LOC 4 – 6, we can conclude that PDs that are better dispersed in the main body generally lead to increased damping ratios for both modes. As a result, it is crucial to carefully consider the placement of PDs to ensure that they effectively intersect with the maximum displacement regions of modes, thereby achieving optimal damping performance.

3.2.3 Effect of the number of the unfused cavities

As explained in the previous sections, the mode shape deformation profile plays a critical role in determining a specimen's effectiveness for a given mode. One of the key ideas in this study was to investigate how the distribution of particle dampers (PDs) within the main body affects the specimen's behavior. To this end, specimens were designed with PDs having equal volume fractions for each group but varying in number, and efforts were made to maintain the PDs' locations within the main body as similar as possible. The resulting four comparison groups were labeled NOD 1 through 4.

Fig. 3.5 displays the results for specimens in groups NOD 1–4, with Fig. 3.5a showing group NOD 1, which contains specimens 1, 7, and 16. Considering the specimens in NOD 1 (see Fig. 3.5a), it was found that specimen 1, which has a single cavity for the same volume fraction, was the most effective for the first mode. However, specimen 16 exhibited the best performance for the second mode in this group, owing to its mode shape deformation profile, as mentioned in the previous sections. Moreover, the damping ratio of the first mode for specimen 7 fell between those of specimens 1 and 16. However, its performance was the worst among the three specimens for the second mode. In the case of specimen 7, although the PDs are located closer to the tips than in specimen 1, their position is also closer to the nodal points of the second mode shape, resulting in lower damping ratios. This highlights the fact that the PDs' location has a greater impact on the overall damping performance of the specimen than their quantity.

In the case of NOD 2 specimens (see Fig. 3.5b), we compared specimen 3, which has a single cavity, to specimen 10, which has two cavities. The damping ratio of the first mode is higher for specimen 3 because it covers a larger region in the high deformation zone for the first mode, unlike specimen 10 with its two distributed cavities that are located away from this regionHowever, the damping ratios of the second mode are similar for both specimens since neither of them covers any region closer to the tips, which is the high deformation zone for the second mode. A similar trend can also be observed for the groups of NOD 4 specimens, as shown in Fig. 3.5d.

In summary, separating cavities can result in missing the maximum deflection zone due to their location. This was observed more clearly in NOD 3, where even a small shift in the cavity location had a noticeable impact. It was found that changing the number of particle dampers (PD) did not cause a significant increase or decrease in damping performance, as long as the volume fractions and locations of the PDs remained similar. Nonetheless, it was observed that the location of the dampers is closely associated with their efficacy.

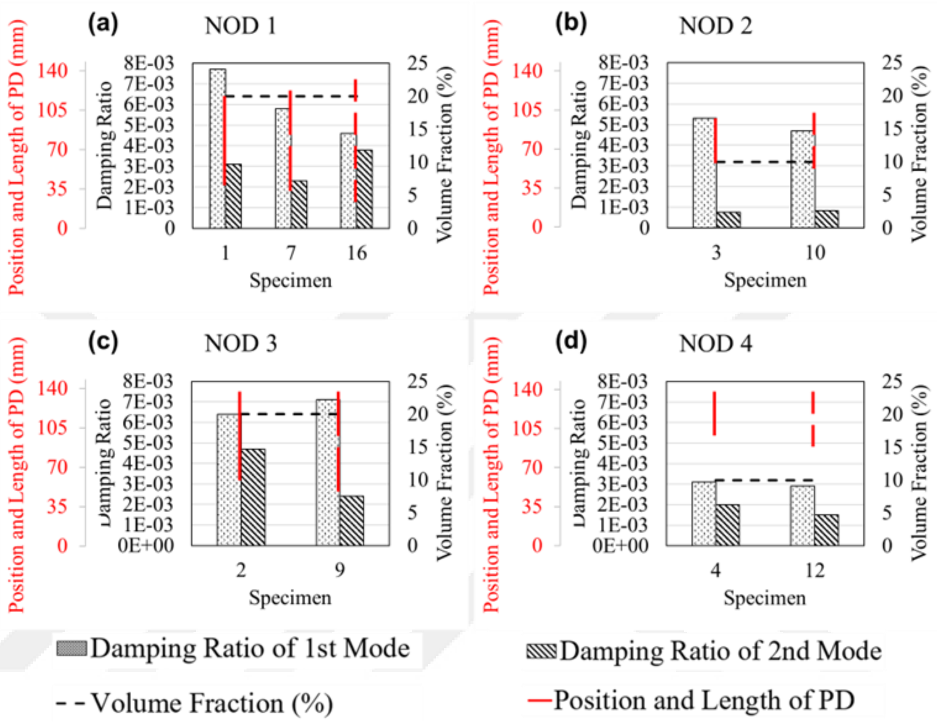

Figure 3.5 : Effect of the number of dampers (a) NOD 1, (b) NOD 2, (c) NOD 3 and (d) NOD 4. Red lines represent the cavity length and location for illustration purposes to compare the data clearly.

Additionally, the results of this study recommend that the number and distribution of cavities in a specimen can significantly impact its effectiveness for different modes. Specimen 1, for instance, has a single cavity, whereas specimen 16 has multiple cavities. Nevertheless, specimen 1 performed better than the other specimens in NOD 1 for the first mode, proving that having a single, well-placed cavity can be more effective than having multiple cavities in certain cases.

As a summary, these findings highlight the importance of carefully designing the geometry and properties of specimens to optimize their performance for different modes. By doing so, it may be possible to enhance the mechanical behavior of materials and structures and, in turn, improve their efficiency and durability in various applications.

3.2.4 Results of emptied specimen

Below are the normalized comparisons of the test results conducted before and after dust emptying in Specimen 5 in Table 3.2. The graphs and damping ratio calculations clearly show the damping effect caused by the powder. Due to the different setups, back-to-back amplitude values could not be obtained, and therefore, an RSS comparison could not be performed.

Table 3.2 : Fully-fused specimen, specimen 5 with powder and specimen 5 without powder results.

Parameter	1st Mode Frequency (Hz)	1st Mode Damping Ratio	2nd Mode Frequency (Hz)	2nd Mode Damping Ratio
0 (Fully Fused)	2,197	7.1e-4	3424	5.0e-4
5 (With Powder)	2,204	3.3e-3	3373	5.2e-4
5 (Without Powder)	2189	1.1e-3	3366	4.6e-4

The normalized graph is presented with a focus on the first mode since this specimen is more effective in that mode. The FRF results for each point are provided in the appendix. The comparison plots in Fig. 3.6 include the fully fused specimen as well, ensuring a clear comparison.

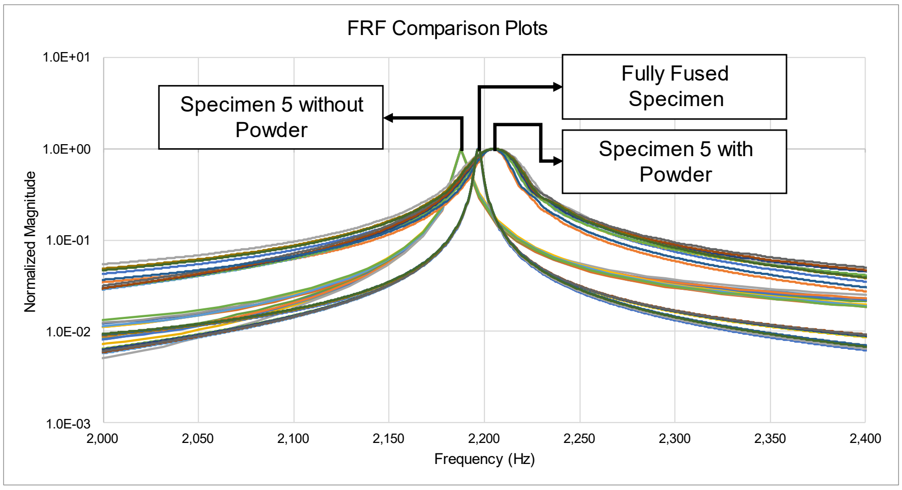

Figure 3.6 : Fully-Fused Specimen & Specimen 5 with and without powder normalized FRF comparison for the first mode.

The normalized graph is specifically focused on this specimen because it is more effective in the first mode. The FRF results for each point are provided in the appendix.

The results clearly indicate that emptying the powder has led to a threefold decrease in damping ratio for the first mode and a 1.13-fold decrease for the second mode. In fact, it has been observed that the damping ratio of the second mode is even lower compared to the fully fused specimen.

3.3 Results of Clamped-Free and Free-Free Tests for 2nd DoE

The impact of the design parameters and boundary conditions on the damping behavior is examined in this section, where comparative experimental results are provided. All FRF graphs are given in appendix. Table 3.3 presents the natural frequencies, damping ratios for the first mode, and weight of the printed specimens. The specimens were excited from 9 different places as indicated in Fig. 2.15, and each damping ratio given in Table 3.3 was averaged by these points to provide a better interpretation. The natural frequencies and damping performance are significantly impacted by the total mass of the fabricated beams and the volume fraction of the unfused cavity to total volume. It is also shown in Table 3.3 that PDs exhibit up to 12 times higher damping when compared to the fully fused one, while a change in natural frequencies less than 3% is observed for specimens tested both clamped-free and free-free.

Table 3.3 : Damping ratio comparison according to boundary condition.

Parameter	Boundary Condition	Natural Frequency (Hz)	Damping Ratio
0 (Fully Fused)	Clamped -Free	299.8	0.0059
	Free-Free	1912	0.0010
1	Clamped -Free	313.9	0.0093
	Free-Free	1915	0.0034
2	Clamped -Free	316.5	0.0112
	Free-Free	1966.2	0.0086
3	Clamped -Free	303.7	0.0136
	Free-Free	1956.7	0.0087
4	Clamped -Free	314.9	0.0143
	Free-Free	1881	0.004
5	Clamped -Free	313.7	0.0271
	Free-Free	1981.4	0.0111
6	Clamped -Free	300.9	0.0172
	Free-Free	1912.8	0.0122

3.3.1 Effects of thickness and width on damping performance

In this section, the effects of the cavity thickness on the damping performance is investigated. To examine the impact of damping performance while keeping the overall unfused particle volume constant, beams with two different cavity thicknesses of 4 mm and 6 mm are fabricated, with the widths of the unfused powder cavities adjusted accordingly. Fig. 3.7 presents the damping ratios of the first mode of the beams with unfused cavities. It can be observed that the damping of the PD integrated specimens enhances with increasing cavity thickness for all specimens under both clamped-free and free-free boundary conditions. A similar trend was also reported by Ehlers et al. in their study on the effect of cavity thickness on damping performance [12].

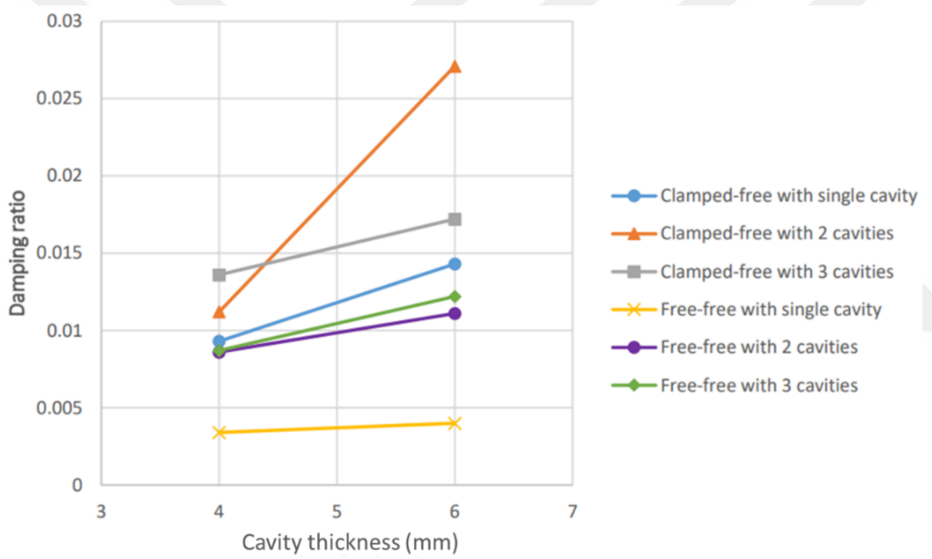

Figure 3.7 : Effect of boundary conditions on the damping performance.

The improvement in the damping performance by increasing cavity thickness is related to the increasing cross-sectional area in the direction of vibration. However, in the current study, the cross-sectional area was kept constant while increasing the thickness of the unfused cavity through reducing the cavity width. The results indicate that the variation in thickness in the direction of vibration has a greater effect on the damping performance than the variation in width.

3.3.2 Effects of boundary conditions on damping performance

The damping performance of the fabricated beams is tested under clamped-free and free-free conditions to characterize the impact of the boundary conditions. The obtained damping ratios from impact hammer testing are compared in Fig. 3.8. It can be seen that damping values of the clamped-free specimens are higher compared to the specimens tested under free-free condition for the first bending mode.

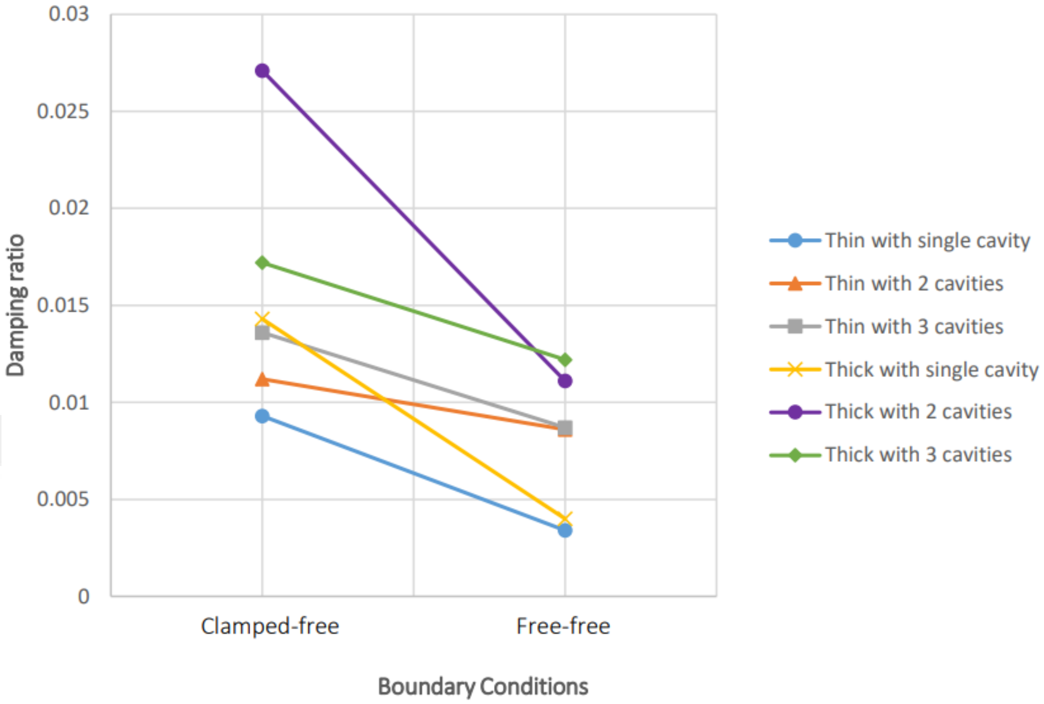

Figure 3.8 : Effect of boundary conditions on the damping performance.

This can be explained by the frequency and mode shape dependency of the damping performance. The impact of the frequency dependency of the particle dampers on the damping behavior through testing beams only under the free-free condition for higher bending modes was demonstrated by Ehlers et al. [12, 38]. The results show that damping decreases with increasing frequency, confirming the findings of the present study. However, assessments should be repeated for higher natural frequencies under different boundary conditions to have frequency-dependent damping characterization.

5. CONCLUSION

This thesis examined the dynamic behavior of Inconel 718 samples with integrated particle dampers (PDs) produced using LPBF. Modal tests were conducted, and the modal parameters were obtained from the FRFs up to 4,000 Hz using the RFP method. Two modes (bending and torsional modes) were identified within the measured frequency range. The impact of parameters such as the number of PDs, location, and size on the damping characteristics of the fabricated beams was examined separately by conducting a wide DoE analysis. The results revealed that the damping performance is better for larger PDs (i.e., for higher volume fractions), and the location effect is the most important factor in the damping performance of the particle dampers for a specific mode. Additionally, the damping ratios can be enhanced up to 10 times compared to the fully fused specimen.

In the section where boundary conditions are investigated, it was observed how much damping ratios can vary. Therefore, it was emphasized that boundary conditions should be considered in PD design. Additionally, it should be noted that damping can also come from the clamped end if there is one. Moreover, since mode shape can also vary depending on the boundary conditions, attention should be paid to the issue discussed in the 1st DoE. Further investigations on these areas are necessary in future studies.

In addition to the aforementioned conclusions, there is a need to develop analytical solutions, increase experimental studies, and establish a suitable optimization method to make this technology usable. Also, it is possible to use experimental modal analysis to determine the dynamic characteristics of physical systems while considering structural parameters, validating models, troubleshooting and fault detection, conducting structural health monitoring, and performing design optimization. Moreover, although there are limited examples in the literature, there is also a need for studies with structures simulating a real component, in addition to simple test samples. The effectiveness of these structures should be demonstrated not only in laboratory tests but also in real applications.

In summary, while PDs integrated into structures offer advantages such as additive manufacturing, lighter designs, and improved damping performance, further research is needed. Developing high-fidelity numerical models can better understand how PDs affect the dynamic behavior, and experimentally extracting damping characteristics for higher modes and different boundary conditions can create a dataset for possible optimization applications. The use of PDs in various industries, along with continued research and development, can lead to significant advancements in engineering design and manufacturing.

REFERENCES

[1] **Url-1** <*https://mustafaeroglu.sakarya.edu.tr/sites/mustafaeroglu.sakarya.edu.tr/file/Mekanik_Titresimler_Ders_Notlari_Zeki_Kiral.pdf*>, date retrieved 02.04.2023.

[2] **Rao, S. S.** (2006). *Mechanical Vibrations* (5th ed.). Pearson Education, Inc.

[3] **Url-2** **<***https://theconstructor.org/earthquake/seismic-dampers/8332/*>, date retrieved 02.04.2023.

[4] **Zhang, C., Chen, T., Wang, X., and Yu, K.** (2016). Influence of cavity on the performance of particle damper under centrifugal loads. *JVC/Journal of Vibration and Control*, *22*(6), 1704–1714. https://doi.org/10.1177/1077546314544351

[5] **Lu, Z., Wang, Z., Masri, S. F., and Lu, X.** (2018). Particle impact dampers: Past, present, and future. In *Structural Control and Health Monitoring* (Vol. 25, Issue 1). John Wiley and Sons Ltd. https://doi.org/10.1002/stc.2058

[6] **Simonian, S. S.** (1995). Particle beam damper. In C. D. Johnson (Ed.), *Smart Structures and Materials 1995: Passive Damping* (Vol. 2445, pp. 149–160). SPIE. https://doi.org/10.1117/12.208884

[7] **Mao, K., Wang, M. Y., Xu, Z. Z., and Chen, T.** (2004). Simulation and characterization of particle damping in transient vibrations. *Journal of Vibration and Acoustics, Transactions of the ASME*, *126*(2), 202–211. https://doi.org/10.1115/1.1687401

[8] **Saeki, M.** (2005). Analytical study of multi-particle damping. *Journal of Sound and Vibration*, *281*(3–5), 1133–1144. https://doi.org/10.1016/j.jsv.2004.02.034

[9] **Fowler, B. L., Flint, E. M., and Olson, S. E.** (2001). Design methodology for particle damping. In D. J. Inman (Ed.), *Smart Structures and Materials 2001: Damping and Isolation* (Vol. 4331, pp. 186–197). SPIE. https://doi.org/10.1117/12.432703

[10] **Xiao, W., Li, J., Wang, S., and Fang, X.** (2016). Study on vibration suppression based on particle damping in centrifugal field of gear transmission. *Journal of Sound and Vibration*, *366*, 62–80. https://doi.org/10.1016/j.jsv.2015.12.014

[11] **Olson, S. E.** (2003). An analytical particle damping model. *Journal of Sound and Vibration*, *264*(5), 1155–1166. https://doi.org/10.1016/S0022-460X(02)01388-3

[12] **Ehlers, T., Tatzko, S., Wallaschek, J., and Lachmayer, R.** (2021). Design of particle dampers for additive manufacturing. *Additive Manufacturing*, *38*, 101752. https://doi.org/10.1016/j.addma.2020.101752

[13] **Papalou, A., and Masri, S. F.** (1996). Performance of Particle Dampers Under Random Excitation. *Journal of Vibration and Acoustics*, *118*(4), 614–621. https://doi.org/10.1115/1.2888343

[14] **Panossian, H. V.** (1992). Structural Damping Enhancement Via Non-Obstructive Particle Damping Technique. *Journal of Vibration and Acoustics*, *114*(1), 101–105. https://doi.org/10.1115/1.2930221

[15] **Friend, R. D., and Kinra, V. K.** (2000). Particle impact damping. *Journal of Sound and Vibration*, *233*(1), 93–118. https://doi.org/10.1006/jsvi.1999.2795

[16] **Fowler, B. L., Flint, E. M., and Olson, S. E.** (2000). Effectiveness and predictability of particle damping. In T. T. Hyde (Ed.), *Smart Structures and Materials 2000: Damping and Isolation* (Vol. 3989, pp. 356–367). SPIE. https://doi.org/10.1117/12.384576

[17] **Sánchez, M., Carlevaro, C. M., and Pugnaloni, L. A.** (2014). Effect of particle shape and fragmentation on the response of particle dampers. In *JVC/Journal of Vibration and Control* (Vol. 20, Issue 12, pp. 1846–1854). SAGE Publications Inc. https://doi.org/10.1177/1077546313480544

[18] **Aiba, T., Murata, R., Henmi, N., and Nakamura, Y.** (1995). An Investigation on Variable-Attractive-Force Impact Damper and Application for Controlling Cutting Vibration in Milling Process. *Journal of the Japan Society for Precision Engineering*, *61*(1), 75–79. https://doi.org/10.2493/jjspe.61.75

[19] **Moore, J. J., Palazzolo, A. B., Gadangi, R., Nale, T. A., Klusman, S. A., Brown, G. V., and Kascak, A. F.** (1995). A Forced Response Analysis and Application of Impact Dampers to Rotordynamic Vibration Suppression in a Cryogenic Environment. *Journal of Vibration and Acoustics*, *117*(3A), 300–310. https://doi.org/10.1115/1.2874452

[20] **Chen, J., and Georgakis, C. T.** (2013). Tuned rolling-ball dampers for vibration control in wind turbines. *Journal of Sound and Vibration*, *332*(21), 5271–5282. https://doi.org/10.1016/j.jsv.2013.05.019

[21] **Tian, L., and Gai, X.** (2015). Wind-induced vibration control of power transmission tower using pounding tuned mass damper. *Journal of Vibroengineering*, *17*(7), 3693–3701.

[22] **Zhang, P., Song, G., Li, H.-N., and Lin, Y.-X.** (2013). Seismic Control of Power Transmission Tower Using Pounding TMD. *Journal of Engineering Mechanics*, *139*(10), 1395–1406. https://doi.org/10.1061/(ASCE)EM.1943-7889.0000576

[23] **Zhang, P., Li, L., Patil, D., Singla, M., Li, H.-N., Mo, Y. L., and Song, G.** (2016). Parametric study of pounding tuned mass damper for subsea jumpers. *Smart Materials and Structures*, *25*(1), 015028. https://doi.org/10.1088/0964-1726/25/1/015028

[24] **Li, H., Zhang, P., Song, G., Patil, D., and Mo, Y.** (2015). Robustness study of the pounding tuned mass damper for vibration control of subsea

jumpers. *Smart Materials and Structures*, *24*(9), 095001. https://doi.org/10.1088/0964-1726/24/9/095001

[25] **Heckel, M., Sack, A., Kollmer, J. E., and Pöschel, T.** (2012). Granular dampers for the reduction of vibrations of an oscillatory saw. *Physica A: Statistical Mechanics and Its Applications*, *391*(19), 4442–4447. https://doi.org/10.1016/j.physa.2012.04.007

[26] **Wong, C., and Rongong, J.** (2009). Control of Particle Damper Nonlinearity. *AIAA Journal*, *47*(4), 953–960. https://doi.org/10.2514/1.38795

[27] **Sánchez, M., and Manuel Carlevaro, C.** (2013). Nonlinear dynamic analysis of an optimal particle damper. *Journal of Sound and Vibration*, *332*(8), 2070–2080. https://doi.org/10.1016/j.jsv.2012.09.042

[28] **Masri, S. F.** (1969). Analytical and Experimental Studies of Multiple-Unit Impact Dampers. *The Journal of the Acoustical Society of America*, *45*(5), 1111–1117. https://doi.org/10.1121/1.1911581

[29] **Nayeri, R. D., Masri, S. F., and Caffrey, J. P.** (2007). Studies of the Performance of Multi-Unit Impact Dampers Under Stochastic Excitation. *Journal of Vibration and Acoustics*, *129*(2), 239–251. https://doi.org/10.1115/1.2346694

[30] **Lieber, P., and Jensen, D. P.** (1945). An Acceleration Damper: Development, Design, and Some Applications. *Journal of Fluids Engineering*, *67*(7), 523–530. https://doi.org/10.1115/1.4018316

[31] **Scott-Emuakpor, O., George, T., Runyon, B., Holycross, C., Langley, B., Sheridan, L., O'Hara, R., Johnson, P., and Beck, J.** (2018). Investigating Damping Performance of Laser Powder Bed Fused Components With Unique Internal Structures. *Volume 7C: Structures and Dynamics*. https://doi.org/10.1115/GT2018-75977

[32] **Ehlers, T., Lachmayer, R., Vajna, S., and Halle, T.** (2020). Producibility. In *Integrated Design Engineering* (1st ed., pp. 287–323). Springer International Publishing. https://doi.org/10.1007/978-3-030-19357-7_9

[33] **Ehlers, T., and Lachmayer, R.** (2021). Design of a Motorcycle Triple Clamp Optimised for Stiffness and Damping. In *Proceedings of the Munich Symposium on Lightweight Design 2020* (pp. 1–17). Springer Berlin Heidelberg. https://doi.org/10.1007/978-3-662-63143-0_1

[34] **Ganter, N. V., Ehlers, T., Gembarski, P. C., and Lachmayer, R.** (2021). Additive refurbishment of a vibration-loaded structural component. *Proceedings of the Design Society*, *1*, 345–354. https://doi.org/10.1017/pds.2021.35

[35] **Chowdhury, S., Yadaiah, N., Prakash, C., Ramakrishna, S., Dixit, S., Gupta, L. R., and Buddhi, D.** (2022). Laser powder bed fusion: a state-of-the-art review of the technology, materials, properties andamp; defects, and numerical modelling. *Journal of Materials Research and Technology*, *20*, 2109–2172. https://doi.org/10.1016/j.jmrt.2022.07.121

[36] **Wischeropp, T. M., Tarhini, H., and Emmelmann, C.** (2020). Influence of laser beam profile on the selective laser melting process of AlSi10Mg.

Journal of Laser Applications, *32*(2), 022059. https://doi.org/10.2351/7.0000100

[37] **Wang, W., and Xia, Y.** (2022). Topology optimization based channel design for powder-bed additive manufacturing. *Additive Manufacturing*, *54*, 102717. https://doi.org/10.1016/j.addma.2022.102717

[38] **Ehlers, T., and Lachmayer, R.** (2022). Design of Particle Dampers for Laser Powder Bed Fusion. *Applied Sciences (Switzerland)*, *12*(4). https://doi.org/10.3390/app12042237

[39] **Scott-Emuakpor, O., Beck, J., Runyon, B., and George, T.** (2021). Determining unfused powder threshold for optimal inherent damping with additive manufacturing. *Additive Manufacturing*, *38*. https://doi.org/10.1016/j.addma.2020.101739

[40] **Goldin, A., Scott-Emuakpor, O., George, T., Runyon, B., and Cobb, R.** (2021). Structural dynamic and inherent damping characterization of additively manufactured airfoil components. *Journal of Engineering for Gas Turbines and Power*, *143*(5). https://doi.org/10.1115/1.4050022

[41] **Scott-Emuakpor, O., George, T., Runyon, B., Holycross, C., Sheridan, L., and O'Hara, R.** (2020). Assessing Additive Manufacturing Repeatability of Inherently Damped Nickel Alloy Components. *Journal of Engineering for Gas Turbines and Power*, *142*(3). https://doi.org/10.1115/1.4044314

[42] **Scott-Emuakpor, O., George, T., Runyon, B., Beck, J., Sheridan, L., Holycross, C., and O'Hara, R.** (2019). Sustainability study of inherent damping in additively manufactured nickel alloy. *AIAA Journal*, *57*(1), 456–461. https://doi.org/10.2514/1.J057608

[43] **Scott-Emuakpor, O., George, T., Runyon, B., Langley, B., Sheridan, L., Holycross, C., O'Hara, R., and Johnson, P.** (2019). *Forced-Response Verification of the Inherent Damping in Additive Manufactured Specimens* (pp. 81–86). https://doi.org/10.1007/978-3-319-95083-9_15

[44] **Guo, H., Ichikawa, K., Sakai, H., Zhang, H., Zhang, X., Tsuruta, K., Makihara, K., and Takezawa, A.** (2022). Numerical and experimental analysis of additively manufactured particle dampers at low frequencies. *Powder Technology*, *396*, 696–709. https://doi.org/10.1016/j.powtec.2021.11.029

[45] **Qin, Y., Liu, C., Zhang, X., Wang, X., Shi, B., Wang, Y., and Deng, S.** (2021). A three-dimensional discrete element model of triaxial tests based on a new flexible membrane boundary. *Scientific Reports*, *11*(1), 4753. https://doi.org/10.1038/s41598-021-84224-7

[46] **Di Renzo, A., and Di Maio, F. P.** (2004). Comparison of contact-force models for the simulation of collisions in DEM-based granular flow codes. *Chemical* Engineering Science, 59(3), 525–541. https://doi.org/10.1016/j.ces.2003.09.037

[47] **Pourtavakoli, H., Parteli, E. J. R., and Pöschel, T.** (2016). Granular dampers: Does particle shape matter? *New Journal of Physics*, *18*(7). https://doi.org/10.1088/1367-2630/18/7/073049

[48] **Xia, Z., Liu, X., and Shan, Y.** (2011). Application of particle damping for vibration attenuation in brake drum. *International Journal of Vehicle Noise and Vibration*, *7*(2), 178. https://doi.org/10.1504/IJVNV.2011.040573

[49] **Thomas, M. D., and Sadek, M. M.** (1974). The Effectiveness of the Impact Damper with a Spring-Supported Auxiliary Mass. *Journal of Mechanical Engineering Science*, *16*(2), 109–116. https://doi.org/10.1243/JMES_JOUR_1974_016_020_02

[50] **Sadek, M. M., and Mills, B.** (1970). Effect of Gravity on the Performance of an Impact Damper: Part 1. Steady-State Motion. *Journal of Mechanical Engineering Science*, *12*(4), 268–277. https://doi.org/10.1243/JMES_JOUR_1970_012_048_02

[51] **Cempel, C., and Lotz, G.** (1993). Efficiency of Vibrational Energy Dissipation by Moving Shot. *Journal of Structural Engineering*, *119*(9), 2642–2652. https://doi.org/10.1061/(ASCE)0733-9445(1993)119:9(2642)

[52] **Xu, Z., Wang, M. Y., and Chen, T.** (2005). Particle damping for passive vibration suppression: numerical modelling and experimental investigation. *Journal of Sound and Vibration*, *279*(3–5), 1097–1120. https://doi.org/10.1016/j.jsv.2003.11.023

[53] **Hollkamp, J. J., and Gordon, R. W.** (1998). *Experiments with particle damping* (L. P. Davis, Ed.; pp. 2–12). https://doi.org/10.1117/12.310675

[54] **Trigui, M., Foltete, E., Abbes, M. S., Fakhfakh, T., Bouhaddi, N., and Haddar, M.** (2009). An experimental study of a multi-particle impact damper. *Proceedings of the Institution of Mechanical Engineers, Part C: Journal of Mechanical Engineering Science*, *223*(9), 2029–2038. https://doi.org/10.1243/09544062JMES1400

[55] **Els, D. N. J.** (2011). Damping of Rotating Beams with Particle Dampers: Experimental Analysis. *AIAA Journal*, *49*(10), 2228–2238. https://doi.org/10.2514/1.J050984

[56] **Jadhav, T. A., and Awasare, P. J.** (2016). Enhancement of particle damping effectiveness using multiple cell enclosure. *Journal of Vibration and Control*, *22*(6), 1516–1525. https://doi.org/10.1177/1077546314543725

[57] **Zhang, C., Chen, T., Wang, X., and Li, Y.** (2014). Discrete element method model and damping performance of bean bag dampers. *Journal of Sound and Vibration*, *333*(23), 6024–6037. https://doi.org/10.1016/j.jsv.2014.07.011

[58] **Wong, C., Daniel, M., and Rongong, J.** (2007). Prediction of the amplitude dependent behaviour of particle dampers. *48th AIAA/ASME/ASCE/AHS/ASC Structures, Structural Dynamics, and Materials Conference*. https://doi.org/10.2514/6.2007-2043

[59] **Wong, C., and Rongong, J.** (2006). Macromodel Characterisation and Application of Particle Dampers to Vibrating Structures. *47th AIAA/ASME/ASCE/AHS/ASC Structures, Structural Dynamics, and Materials Conferenceandlt;BRandgt; 14th AIAA/ASME/AHS Adaptive*

Structures Conferenceandlt;BRandgt; 7th. https://doi.org/10.2514/6.2006-2208

[60] **Rongong, J., and Tomlinson, G.** (2005). Amplitude Dependent Behaviour in the Application of Particle Dampers to Vibrating Structures. *46th AIAA/ASME/ASCE/AHS/ASC Structures, Structural Dynamics and Materials Conference*. https://doi.org/10.2514/6.2005-2327

[61] **Saeki, M.** (2002). Impact Damping With Granular Materials in a Horizontally Vibrating System. *Journal of Sound and Vibration*, *251*(1), 153–161. https://doi.org/10.1006/jsvi.2001.3985

[62] **Veluswami, M. A., and Crossley, F. R. E.** (1975). Multiple Impacts of a Ball Between Two Plates—Part 1: Some Experimental Observations. *Journal of Engineering for Industry*, *97*(3), 820–827. https://doi.org/10.1115/1.3438688

[63] **Veluswami, M. A., Crossley, F. R. E., and Horvay, G.** (1975). Multiple Impacts of a Ball Between Two Plates—Part 2: Mathematical Modelling. *Journal of Engineering for Industry*, *97*(3), 828–835. https://doi.org/10.1115/1.3438689

[64] **Yokomichi, I., Araki, Y., Jinnouchi, Y., and Inoue, J.** (1996). Impact Damper With Granular Materials for Multibody System. *Journal of Pressure Vessel Technology*, *118*(1), 95–103. https://doi.org/10.1115/1.2842169

[65] **Yang, M. Y., Lesieutre, G. A., Hambric, S. A., and Koopmann, G. H.** (2004). *Development of a design curve for particle impact dampers* (K.-W. Wang, Ed.; p. 450). https://doi.org/10.1117/12.540019

[66] **Url-3** *<https://fabheads.com/blogs/what-is-the-role-of-slicing-in-3d-printing/#:~:text=1.-,What%20is%20Slicing%3F,time%2C%20best%20strength%2C%20etc>*, date retrieved 20.03.2023.

[67] **Han, X., Zhan, Z., Song, X., and Cui, L.** (2022). An Additive Manufacturing Direct Slicing Algorithm Based on a STEP Model. *Electronics*, *11*(10), 1582. https://doi.org/10.3390/electronics11101582

[68] **Url-4** *<https://www.specialmetals.com/documents/technical-bulletins/inconel/inconel-alloy-718.pdf>*, date retrieved 22.03.2023.

[69] **Hosseini, E., and Popovich, V. A.** (2019). A review of mechanical properties of additively manufactured Inconel 718. *Additive Manufacturing*, *30*, 100877. https://doi.org/10.1016/j.addma.2019.100877

[70] **Url-5** **<***https://www.praxairsurfacetechnologies.com/-/media/corporate/praxairsurface/us/documents/brochures/truform-718-metal-powder.pdf?la=en>*, date retrieved 22.03.2023.

[71] **Url-6** *<https://www.ge.com/additive/direct-metal-laser-melting>*, date retrieved 22.03.2023.

[72] **Url-7** **<** *https://www.mm.bme.hu/~gyebro/files/fea/ansys/ansys_12_element_reference.pdf>*, date retrieved 23.03.2023.

[73] **Rahman, M. M., Bakar, R. A., Noor, M. M., Rejab, M. R. M., and Sani, M. S. M.** (2008). Fatigue Life Prediction of Spot-Welded Structures: A

Finite Element Analysis Approach. In *European Journal of Scientific Research* (Vol. 22, Issue 3). http://www.eurojournals.com/ejsr.htm

[74] **Url-8** *<https://en.wikipedia.org/wiki/Modal_testing>*, date retrieved 23.03.2023.

[75] **Url-9** *<https://www.crystalinstruments.com/modal-testing>*, date retrieved 23.03.2023.

[76] **Fahy, F.** (2000). *Foundations of Engineering Acoustics*. Elsevier.

[77] **Bötke, A., Horozoğlu, S., and Yılmaz, Ş.** (2014). FRF Analizlerinde Analiz Sonrası İşlemler İçin Makro Oluşturulması. *7. Otomotiv Teknolojileri Kongresi*.

[78] **Url-10 <***https://www.mathworks.com/matlabcentral/fileexchange/3805-rational-fraction-polynomial-method>*, date retrieved 23.03.2023

[79] **Richardson, M. H., and Formenti, D. L.** (1982). *Parameter Estimation From Frequency Response Measurements Using Rational Fraction Polynomials*.

[80] **Url-11** *<https://accendoreliability.com/root-sum-squared-tolerance-analysis-method/>*, date retrieved 23.03.2023

APPENDICES

APPENDIX A: Dimension details for PD cavities on a section view.

APPENDIX B: FEM Model details.

APPENDIX C: First 5 mode shapes of 1st DoE

APPENDIX D: Used MATLAB code for obtaining the damping ratios.

APPENDIX E: 1st DoE raw FRF data.

APPENDIX F: 2nd DoE raw FRF data.

74

APPENDIX A: Dimension details for PD cavities on a section view.

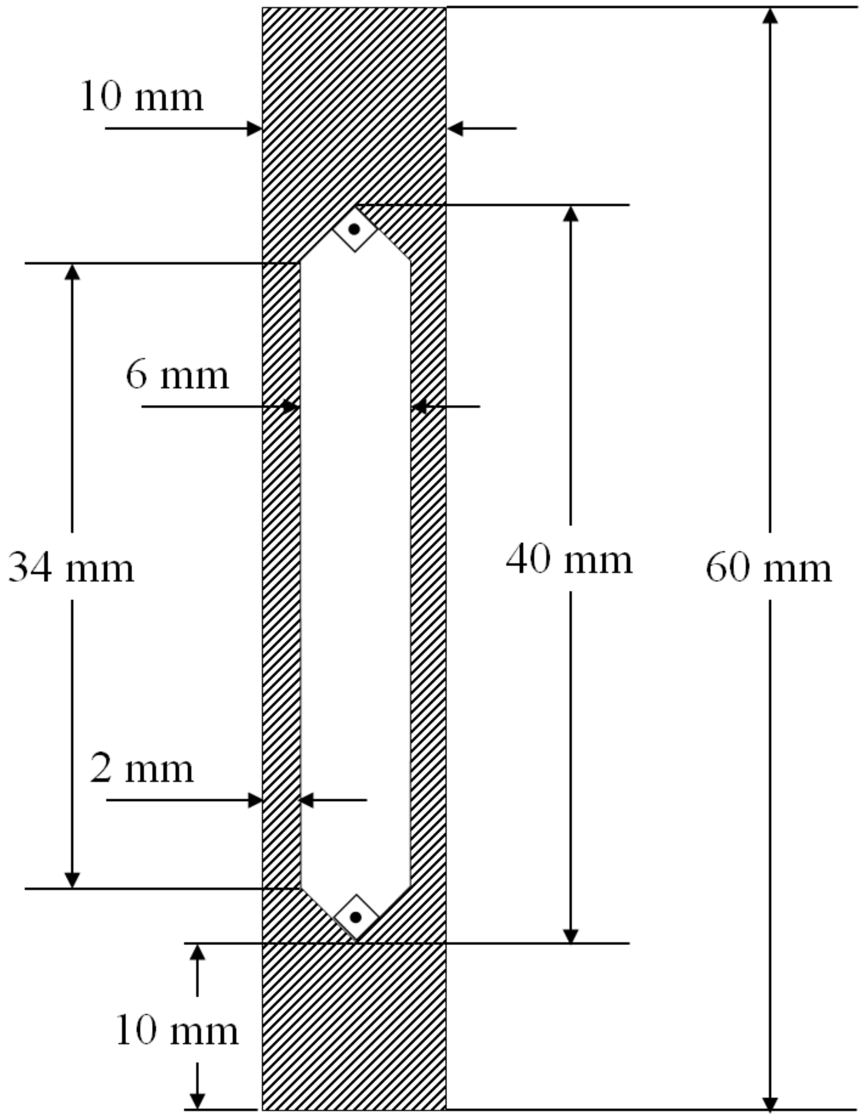

Figure A.1 : Dimension details for PD cavities on a section view for the first DoE. (Print direction is from bottom to top.).

APPENDIX B: FEM Model details.

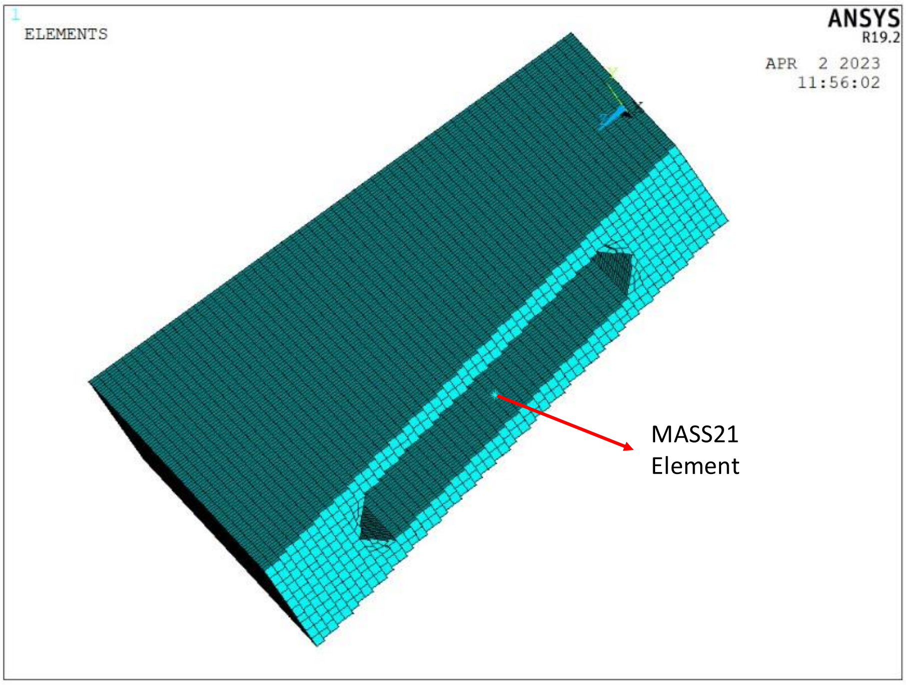

Figure B.1 : Section view of the PD.

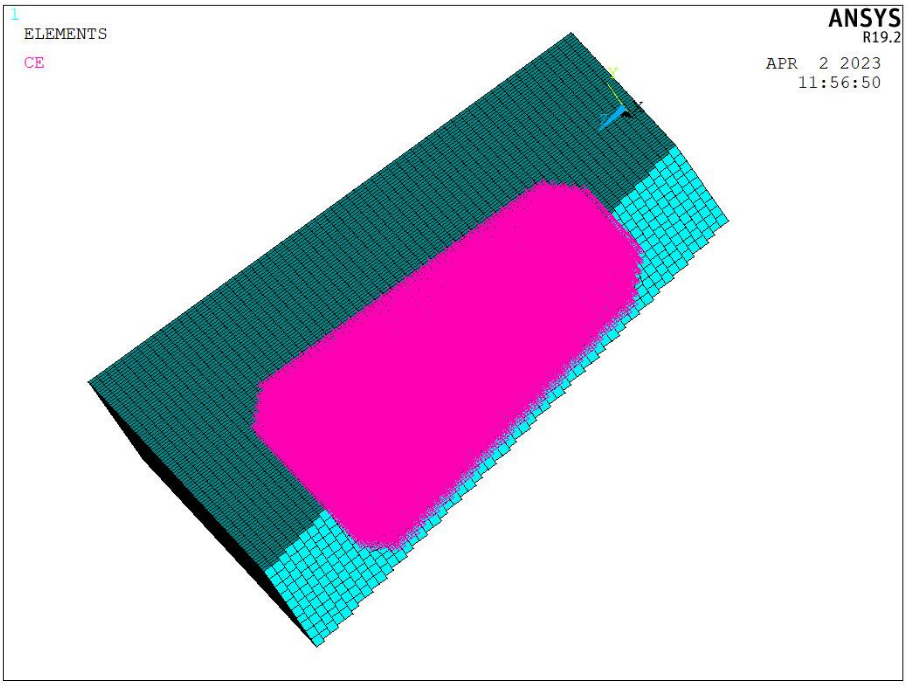

Figure B.2 : RBE3 connection between internal nodes and MASS21 elements (RBE3 elements shown in pink).

APPENDIX C: First 5 mode shapes of 1st DoE

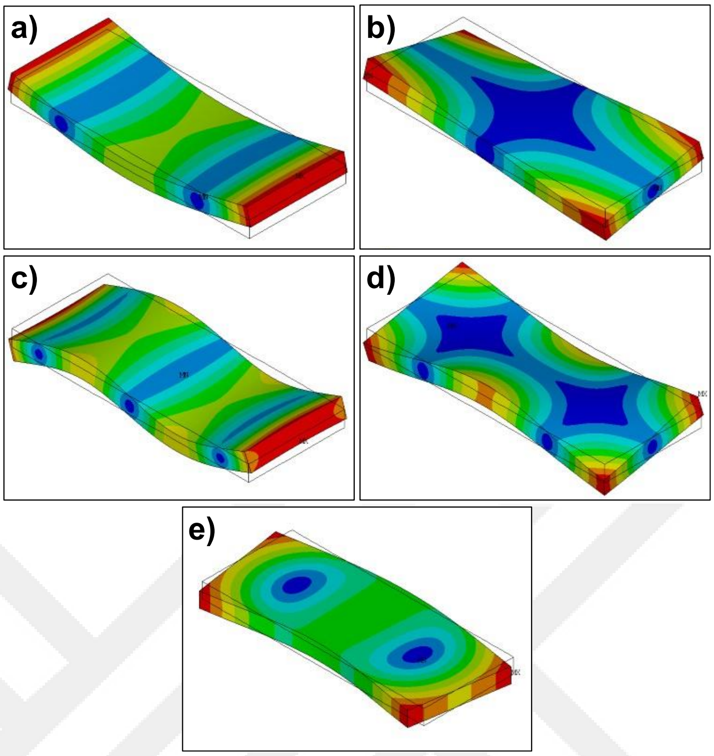

Figure C.1 : First 5 mode shape of fully fused specimen (a) 1st Mode (b) 2nd Mode (c) 3rd Mode (d) 4th Mode (e) 5th Mode.

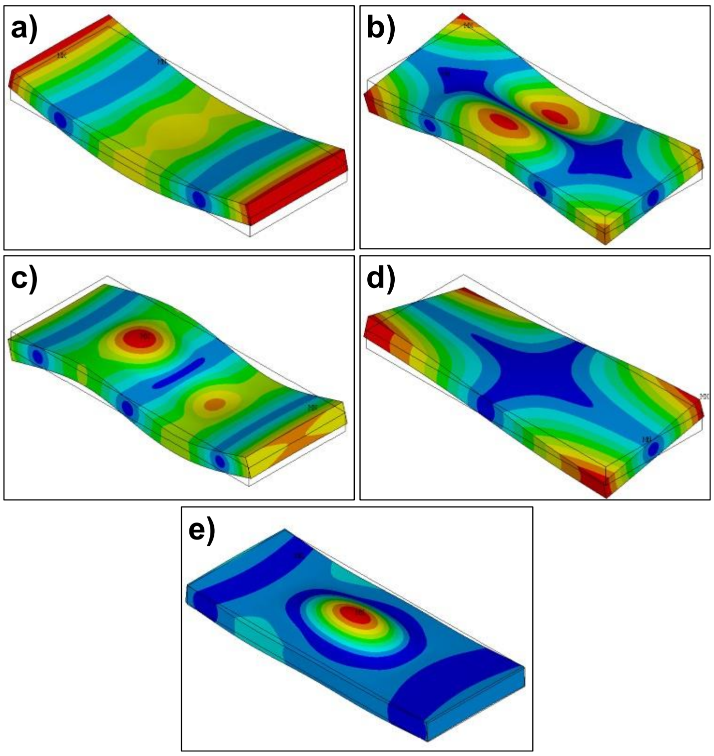

Figure C.2 : First 5 mode shape of Specimen 1 (a) 1st Mode (b) 2nd Mode (c) 3rd Mode (d) 4th Mode (e) 5th Mode.

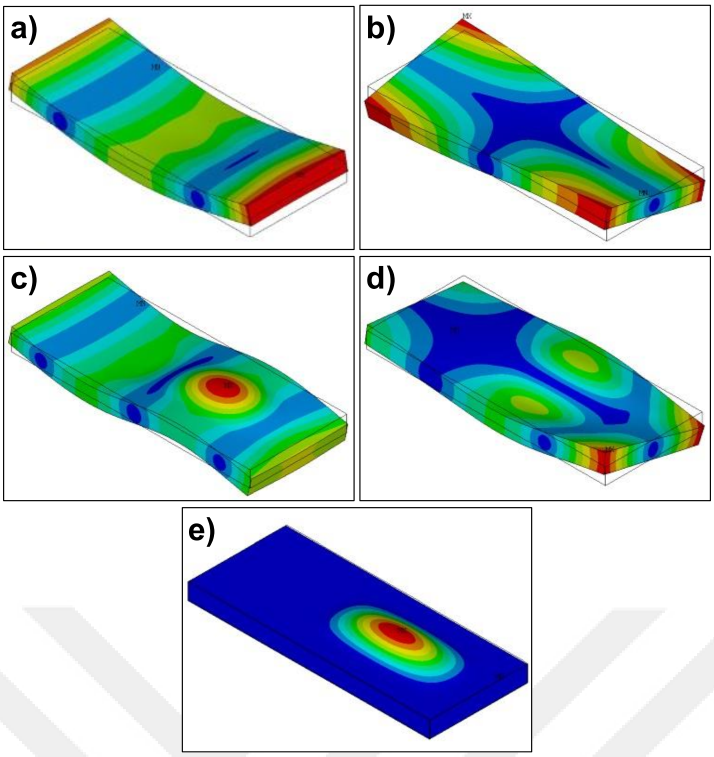

Figure C.3 : First 5 mode shape of Specimen 2 (a) 1st Mode (b) 2nd Mode (c) 3rd Mode (d) 4th Mode (e) 5th Mode.

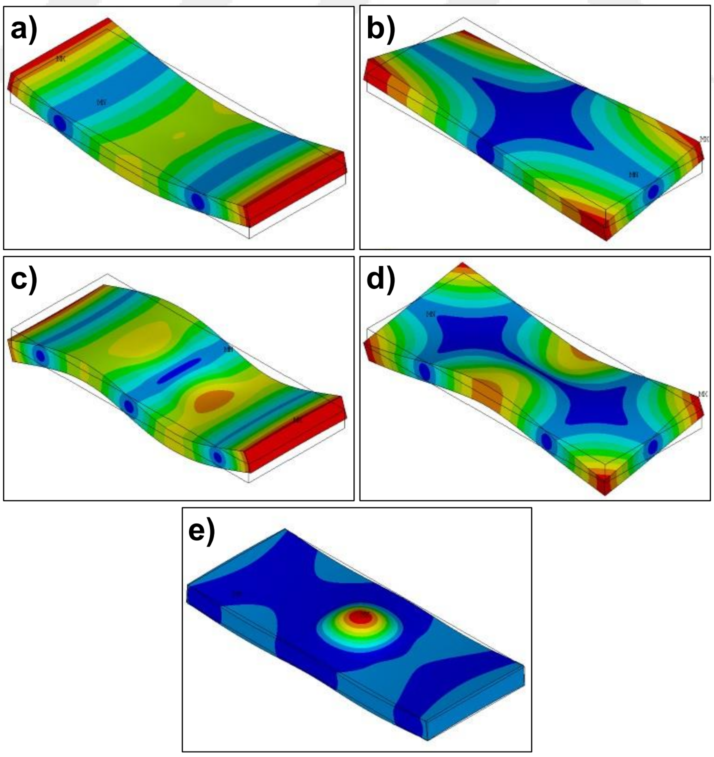

Figure C.4 : First 5 mode shape of Specimen 3 (a) 1st Mode (b) 2nd Mode (c) 3rd Mode (d) 4th Mode (e) 5th Mode.

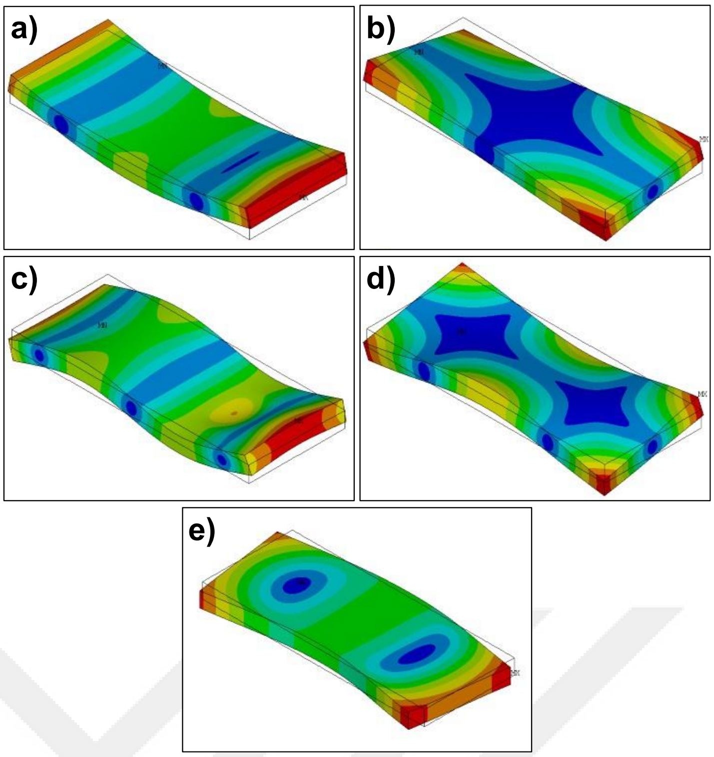

Figure C.5 : First 5 mode shape of Specimen 4 (a) 1st Mode (b) 2nd Mode (c) 3rd Mode (d) 4th Mode (e) 5th Mode.

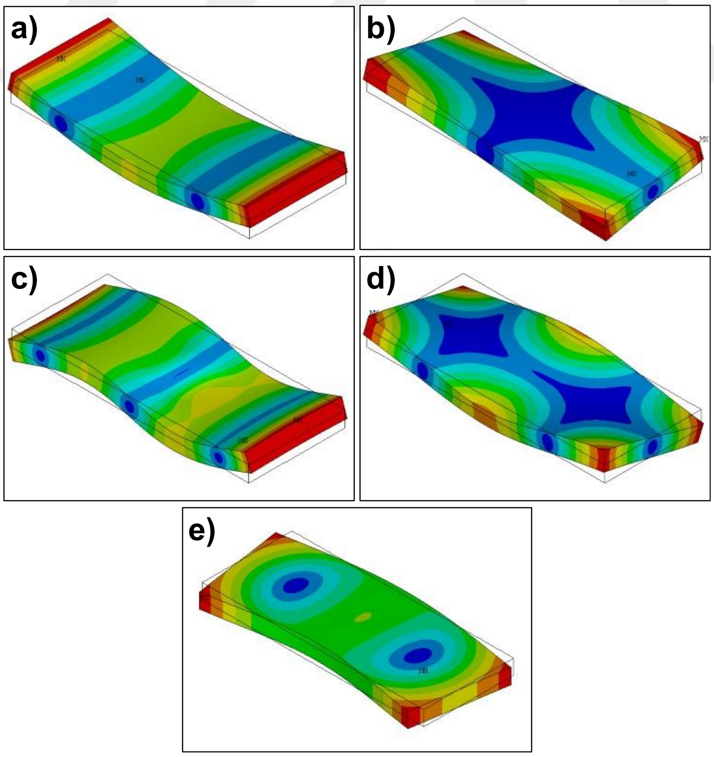

Figure C.6 : First 5 mode shape of Specimen 5 (a) 1st Mode (b) 2nd Mode (c) 3rd Mode (d) 4th Mode (e) 5th Mode.

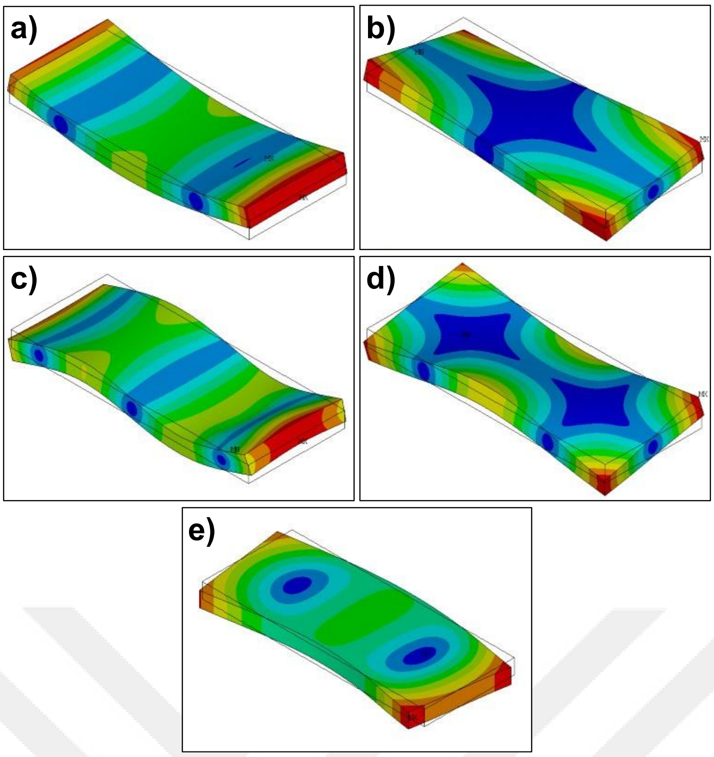

Figure C.7 : First 5 mode shape of Specimen 6 (a) 1st Mode (b) 2nd Mode (c) 3rd Mode (d) 4th Mode (e) 5th Mode.

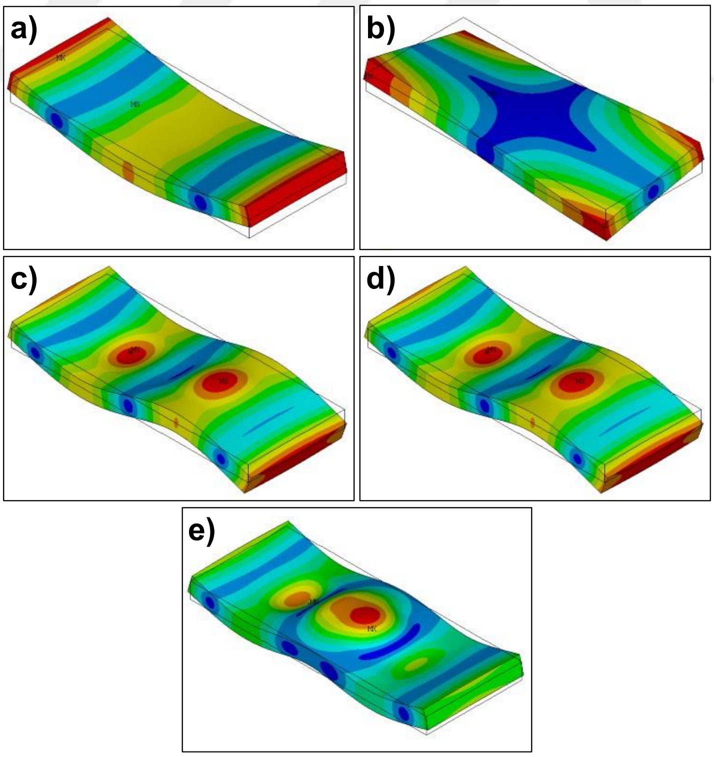

Figure C.8 : First 5 mode shape of Specimen 7 (a) 1st Mode (b) 2nd Mode (c) 3rd Mode (d) 4th Mode (e) 5th Mode.

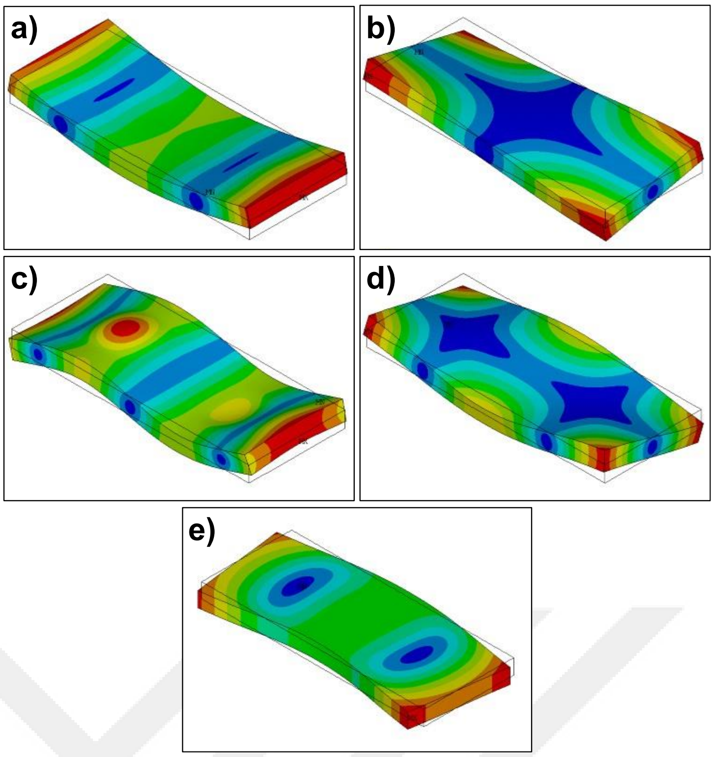

Figure C.9 : First 5 mode shape of Specimen 8 (a) 1st Mode (b) 2nd Mode (c) 3rd Mode (d) 4th Mode (e) 5th Mode.

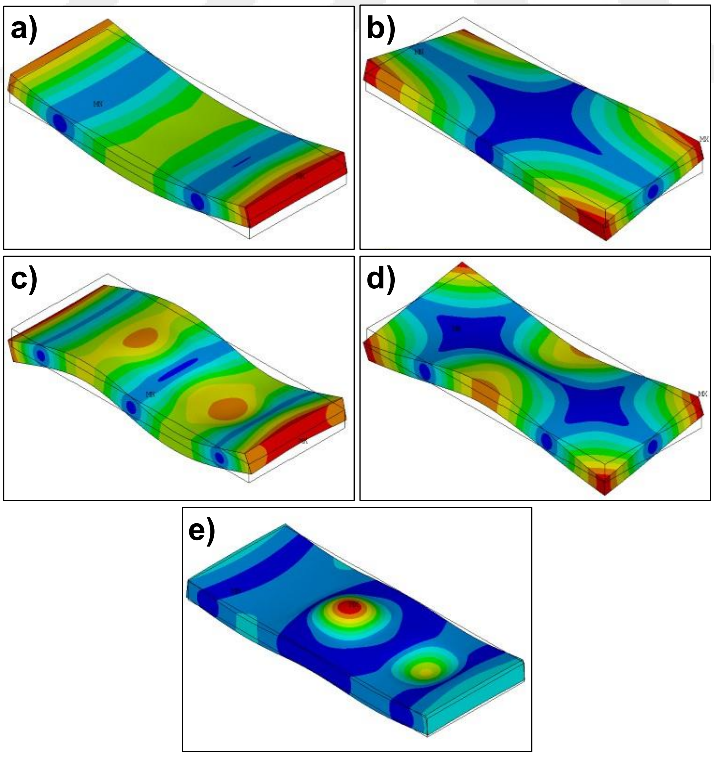

Figure C.10 : First 5 mode shape of Specimen 9 (a) 1st Mode (b) 2nd Mode (c) 3rd Mode (d) 4th Mode (e) 5th Mode.

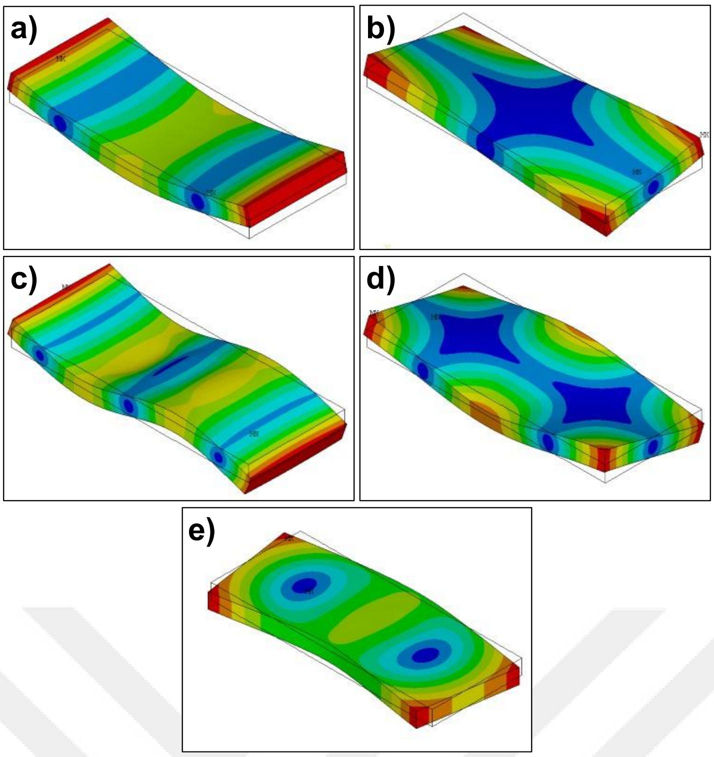

Figure C.11 : First 5 mode shape of Specimen 10 (a) 1st Mode (b) 2nd Mode (c) 3rd Mode (d) 4th Mode (e) 5th Mode.

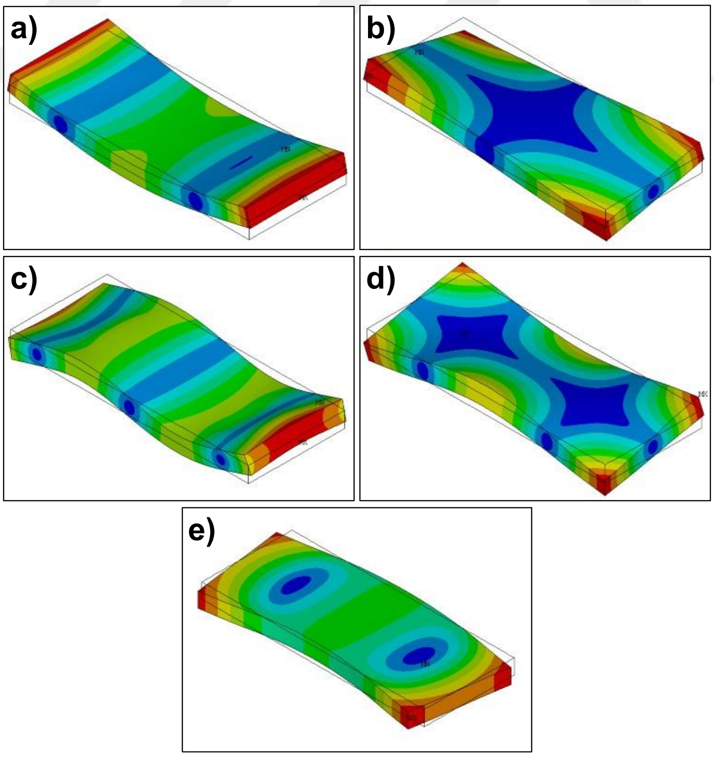

Figure C.12 : First 5 mode shape of Specimen 11 (a) 1st Mode (b) 2nd Mode (c) 3rd Mode (d) 4th Mode (e) 5th Mode.

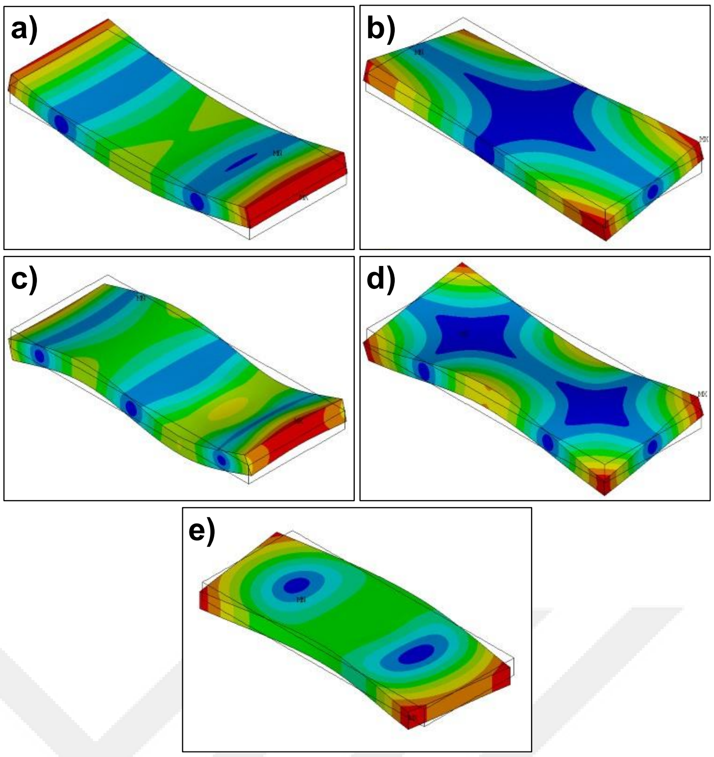

Figure C.13 : First 5 mode shape of Specimen 12 (a) 1st Mode (b) 2nd Mode (c) 3rd Mode (d) 4th Mode (e) 5th Mode.

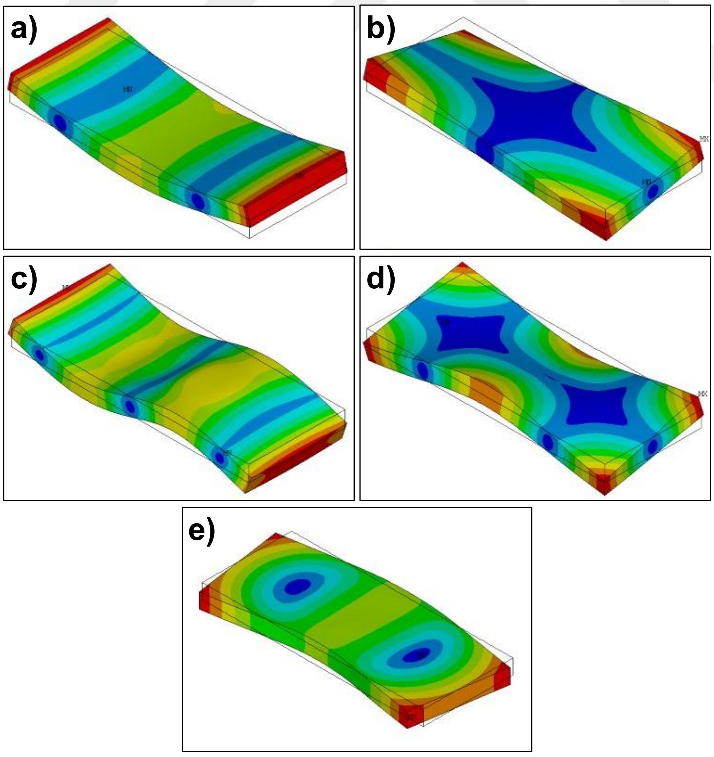

Figure C.14 : First 5 mode shape of Specimen 13 (a) 1st Mode (b) 2nd Mode (c) 3rd Mode (d) 4th Mode (e) 5th Mode.

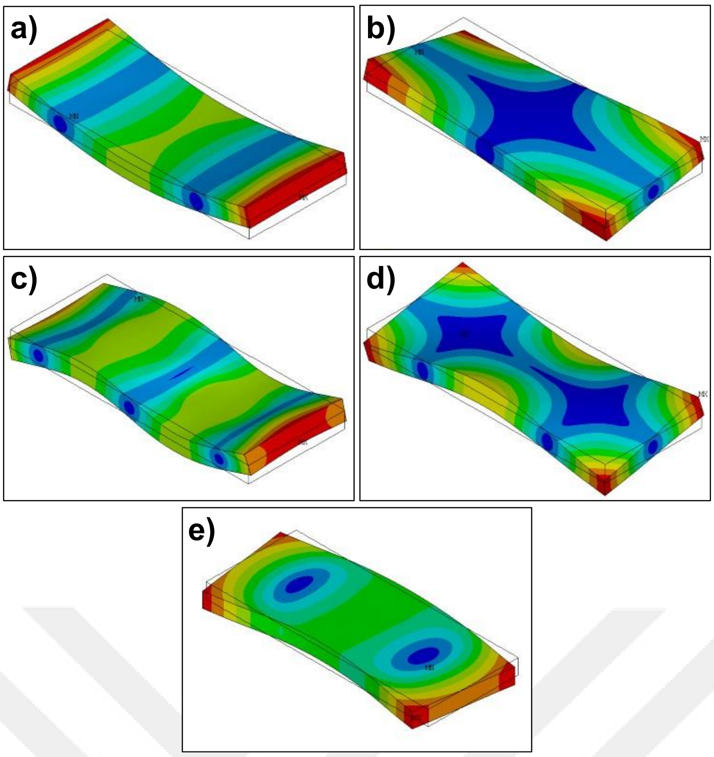

Figure C.15 : First 5 mode shape of Specimen 14 (a) 1st Mode (b) 2nd Mode (c) 3rd Mode (d) 4th Mode (e) 5th Mode.

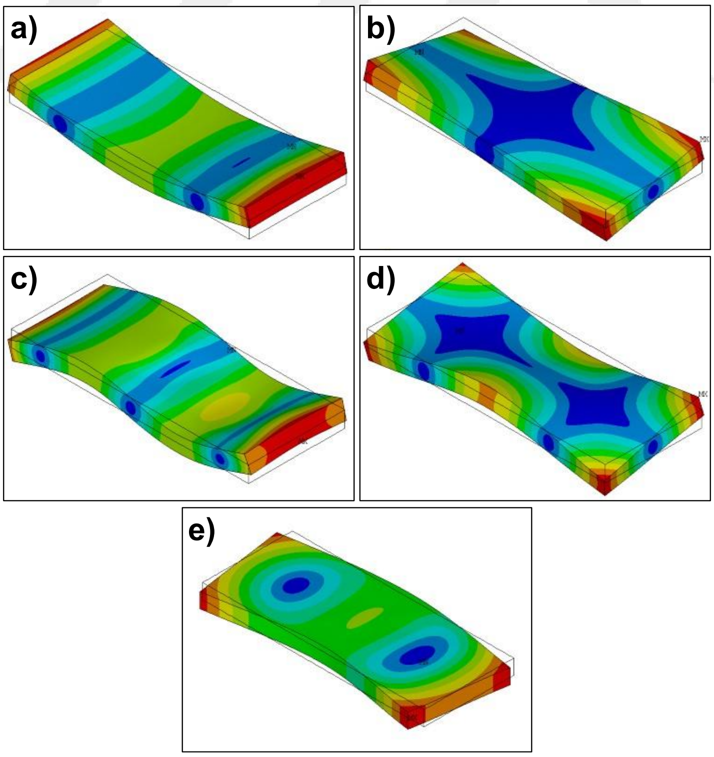

Figure C.16 : First 5 mode shape of Specimen 15 (a) 1st Mode (b) 2nd Mode (c) 3rd Mode (d) 4th Mode (e) 5th Mode.

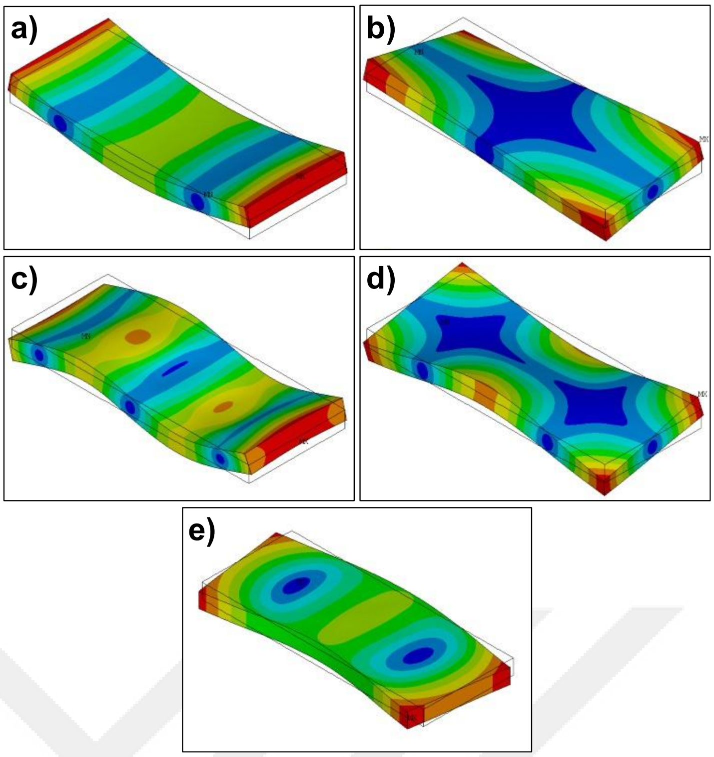

Figure C.17 : First 5 mode shape of Specimen 16 (a) 1st Mode (b) 2nd Mode (c) 3rd Mode (d) 4th Mode (e) 5th Mode.

APPENDIX D: Used MATLAB code for obtaining the damping ratios.

First orthogonal polynomials are created for the RFP method [81].

```
function [P,coeff]=orthogonal(rec,omega,phitheta,kmax)
%ORTHOGONAL Orthogonal polynomials required for rational fraction
% polynomials method. (This code was written to be used with rfp.m)
%
% Syntax: [P,coeff]=orthogonal(rec,omega,phitheta,kmax)
%
% rec      = FRF measurement (receptance).
% omega    = frequency range vector (rad/sec).
% phitheta = weighting function (must be 1 for phi matrix or 2 for
%            theta matrix).
% kmax     = degree of the polynomial.
% P        = matrix of the orthogonal polynomials evaluated at the
%            frequencies.
% coeff    = matrix used to transform between the orthogonal polynomial
%            coefficients and the standard polynomial.
%
% Reference: Mark H.Richardson & David L.Formenti "Parameter Estimation
%           from Frequency Response Measurements Using Rational
Fraction
%           Polynomials", 1ºIMAC Conference, Orlando, FL. November,
1982.
%**********************************************************************
%Chile, March 2002, Cristian Andrés Gutiérrez Acuña, crguti@icqmail.com
%**********************************************************************
if phitheta==1
      q=ones(size(omega)); %weighting function for phi matrix
elseif phitheta==2
      q=(abs(rec)).^2;     %weighting function for theta matrix
else
      error('phitheta must be 1 or 2.')
end
R_minus1=zeros(size(omega));
R_0=1/sqrt(2*sum(q)).*ones(size(omega));
R=[R_minus1,R_0];    %polynomials -1 and 0.
coeff=zeros(kmax+1,kmax+2);
coeff(1,2)=1/sqrt(2*sum(q));
%generating orthogonal polynomials matrix and transform matrix
for k=1:kmax,
      Vkm1=2*sum(omega.*R(:,k+1).*R(:,k).*q);
      Sk=omega.*R(:,k+1)-Vkm1*R(:,k);
      Dk=sqrt(2*sum((Sk.^2).*q));
      R=[R,(Sk/Dk)];
      coeff(:,k+2)=-Vkm1*coeff(:,k);
      coeff(2:k+1,k+2)=coeff(2:k+1,k+2)+coeff(1:k,k+1);
    coeff(:,k+2)=coeff(:,k+2)/Dk;
end
R=R(:,2:kmax+2);         %orthogonal polynomials matrix
coeff=coeff(:,2:kmax+2); %transform matrix
%make complex by multiplying by i^k
i=sqrt(-1);
for k=0:kmax,
   P(:,k+1)=R(:,k+1)*i^k; %complex orthogonal polynomials matrix
```

```
   jk(1,k+1)=i^k;
end
coeff=(jk'*jk).*coeff;    %complex transform matrix
%%%%%%%%%%%%%%%%%%%%%%%%%%%%%%%%%%%%%%%%%%%%%%%%%%%%%%%%%%%%%%%%%%%%%%%
%%%
```

Then, the RFP method is started [81].

```
function [alpha,modal_par]=rfp(rec,omega,N)

%RFP Modal parameter estimation from frequency response function using
% rational fraction polynomial method.
%
% Syntax: [alpha,modal_par]=rfp(rec,omega,N)
%
% rec   = FRF measurement (receptance)
% omega = frequency range vector (rad/sec).
% N     = number of degrees of freedom.
% alpha = FRF generated (receptance).
% modal_par = Modal Parameters [freq,damp,Ci,Oi]:
%             freq = Natural frequencies (rad/sec)
%             damp = Damping ratio
%             Ci   = Amplitude modal constant
%             Oi   = Phase modal constant (degrees)
%
% Reference: Mark H.Richardson & David L.Formenti "Parameter Estimation
%           from Frequency Response Measurements Using Rational
Fraction
%           Polynomials", 1ºIMAC Conference, Orlando, FL. November,
1982.
%**********************************************************************
%Chile, March 2002, Cristian Andrés Gutiérrez Acuña, crguti@icqmail.com
%**********************************************************************
[r,c]=size(omega);
if r<c
      omega=omega.'; %omega is now a column
end
[r,c]=size(rec);
if r<c
      rec=rec.';     %rec is now a column
end
nom_omega=max(omega);
omega=omega./nom_omega; %omega normalization
m=2*N-1; %number of polynomial terms in numerator
n=2*N;   %number of polynomial terms in denominator
%orthogonal function that calculates the orthogonal polynomials
[phimatrix,coeff_A]=orthogonal(rec,omega,1,m);
[thetamatrix,coeff_B]=orthogonal(rec,omega,2,n);
[r,c]=size(phimatrix);
Phi=phimatrix(:,1:c);    %phi matrix
[r,c]=size(thetamatrix);
Theta=thetamatrix(:,1:c); %theta matrix
T=sparse(diag(rec))*thetamatrix(:,1:c-1);
W=rec.*thetamatrix(:,c);
X=-2*real(Phi'*T);
G=2*real(Phi'*W);
d=-inv(eye(size(X))-X.'*X)*X.'*G;
```

```
C=G-X*d;   %{C} orthogonal numerator  polynomial coefficients
D=[d;1];   %{D} orthogonal denominator  polynomial coefficients
%calculation of FRF (alpha)
for n=1:length(omega),
   numer=sum(C.'.*Phi(n,:));
   denom=sum(D.'.*Theta(n,:));
   alpha(n)=numer/denom;
end
A=coeff_A*C;
[r,c]=size(A);
A=A(r:-1:1).'; %{A} standard numerator polynomial coefficients
B=coeff_B*D;
[r,c]=size(B);
B=B(r:-1:1).'; %{B} standard denominator polynomial coefficients
%calculation of the poles and residues
[R,P,K]=residue(A,B);
[r,c]=size(R);
for n=1:(r/2),
   Residuos(n,1)=R(2*n-1);
   Polos(n,1)=P(2*n-1);
end
[r,c]=size(Residuos);
Residuos=Residuos(r:-1:1)*nom_omega; %residues
Polos=Polos(r:-1:1)*nom_omega;       %poles
    freq=abs(Polos);                 %Natural frequencies (rad/sec)
    damp=-real(Polos)./abs(Polos);   %Damping ratios
Ai=-2*(real(Residuos).*real(Polos)+imag(Residuos).*imag(Polos));
Bi=2*real(Residuos);
const_modal=complex(Ai,abs(Polos).*Bi);
      Ci=abs(const_modal);             %Magnitude modal constant
      Oi=angle(const_modal).*(180/pi);   %Phase modal constant
(degrees)

modal_par=[freq, damp, Ci, Oi];    %Modal Parameters
%%%%%%%%%%%%%%%%%%%%%%%%%%%%%%%%%%%%%%%%%%%%%%%%%%%%%%%%%%%%%%%%%%%%%%%%%
```

APPENDIX E: 1st DoE raw FRF data.

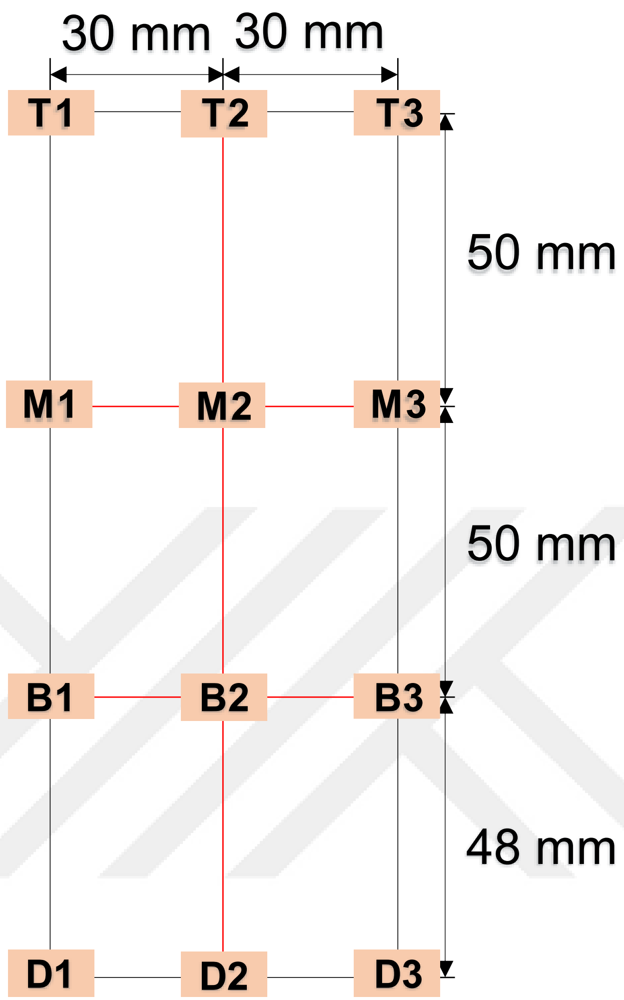

Figure E.1 : 1st DoE Impact Location Naming.

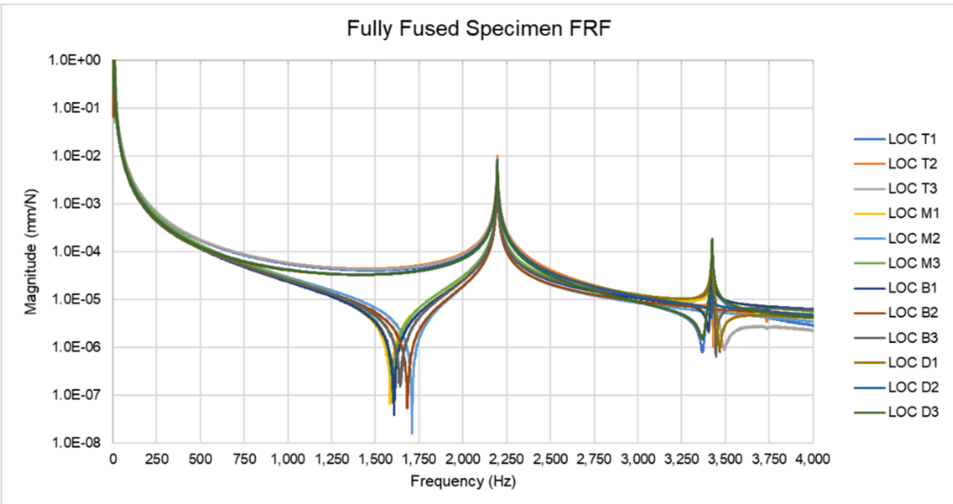

Figure E.2 : 1st DoE Fully Fused Specimen Raw FRF Results.

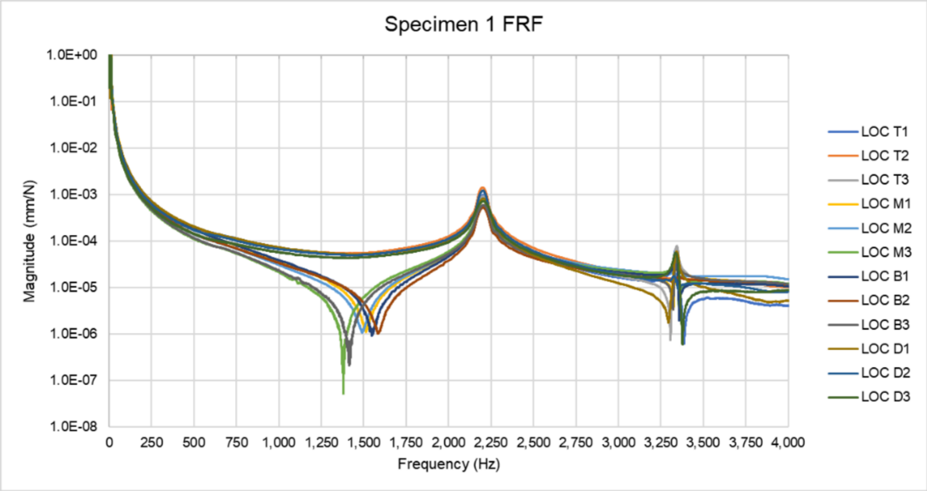

Figure E.3 : 1st DoE Specimen 1 Raw FRF Results.

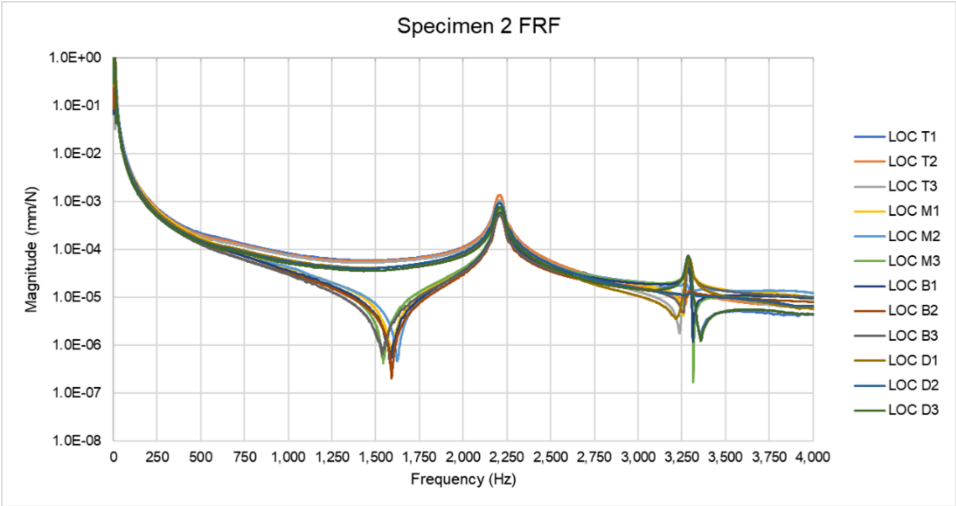

Figure E.4 : 1st DoE Specimen 2 Raw FRF Results.

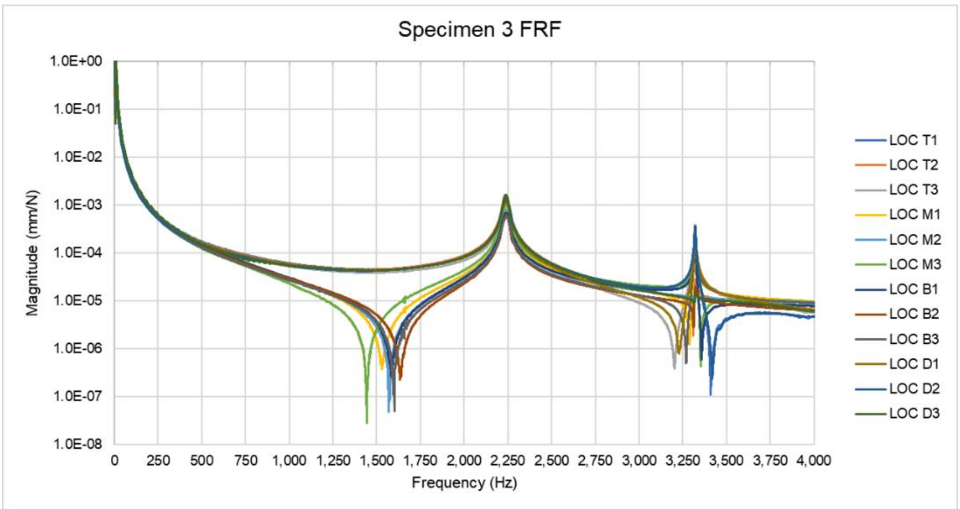

Figure E.5 : 1st DoE Specimen 3 Raw FRF Results.

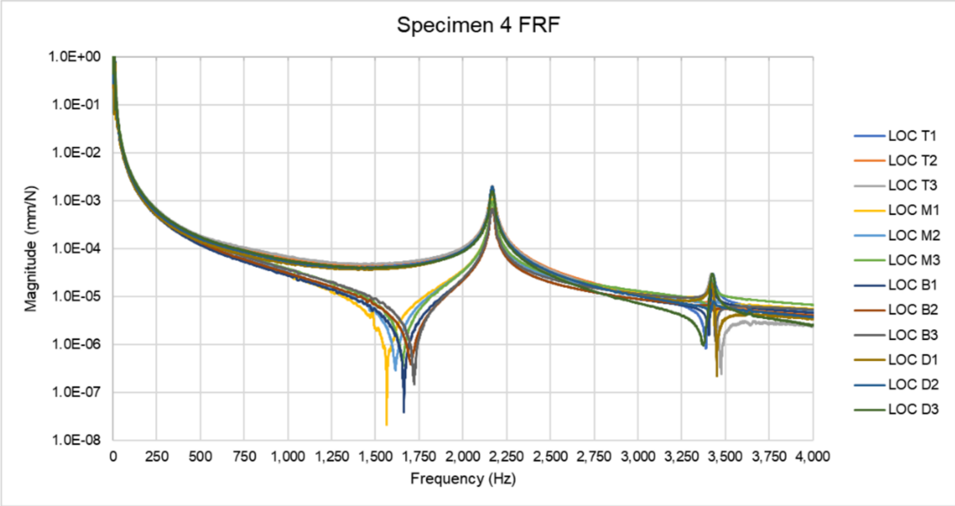

Figure E.6 : 1st DoE Specimen 4 Raw FRF Results.

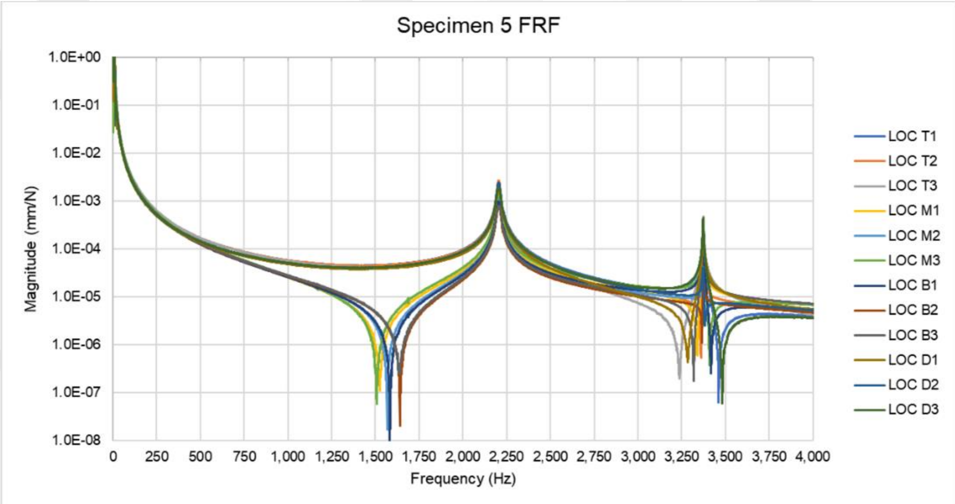

Figure E.7 : 1st DoE Specimen 5 Raw FRF Results.

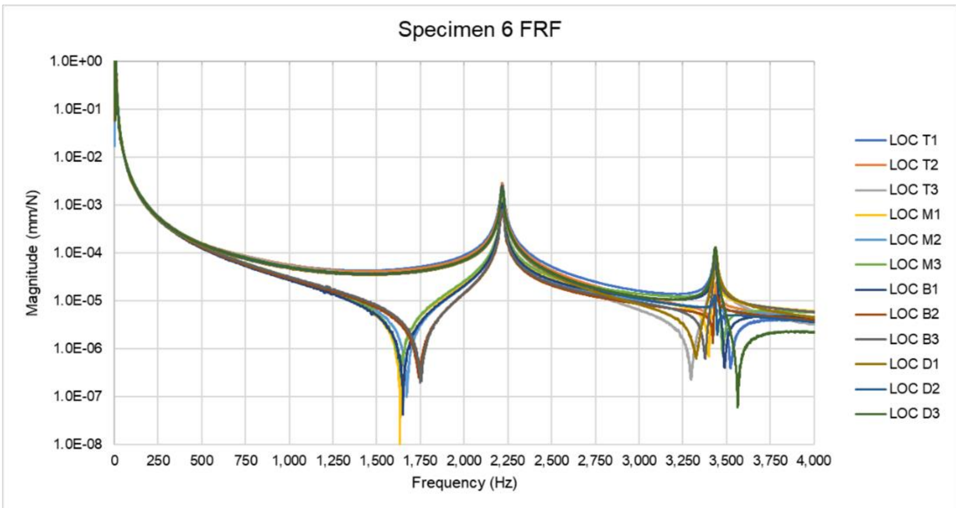

Figure E.8 : 1st DoE Specimen 6 Raw FRF Results.

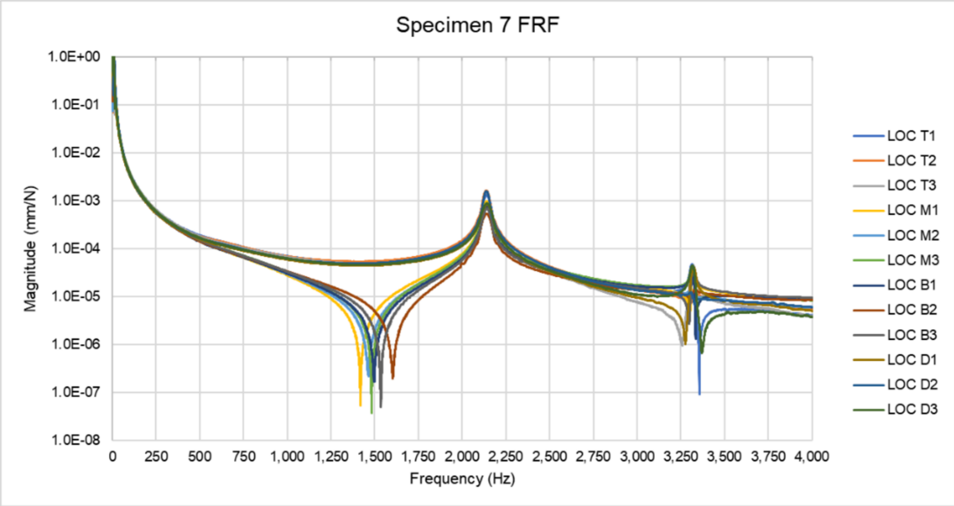

Figure E.9 : 1st DoE Specimen 7 Raw FRF Results.

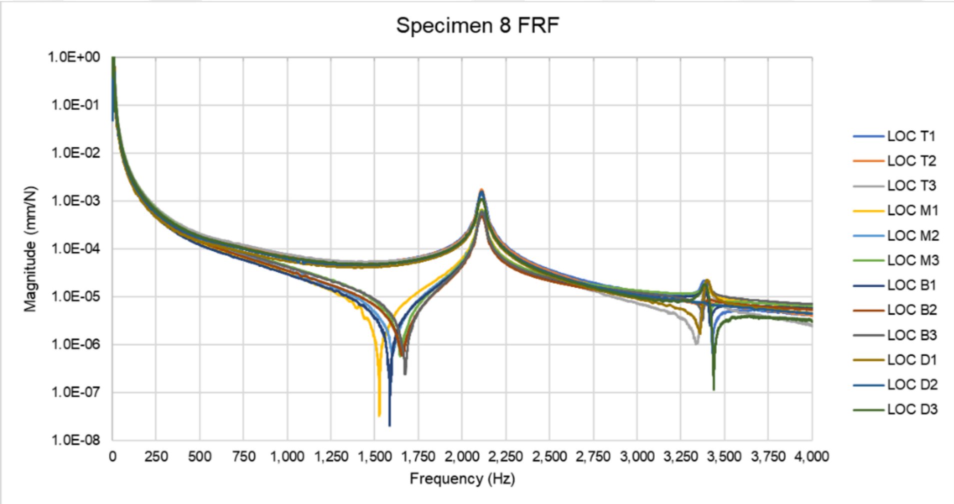

Figure E.10 : 1st DoE Specimen 8 Raw FRF Results.

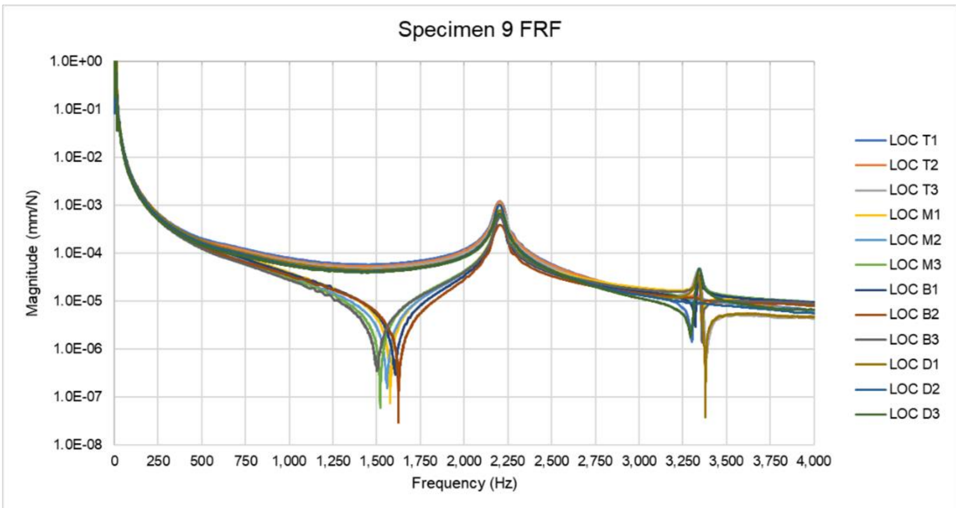

Figure E.11 : 1st DoE Specimen 9 Raw FRF Results.

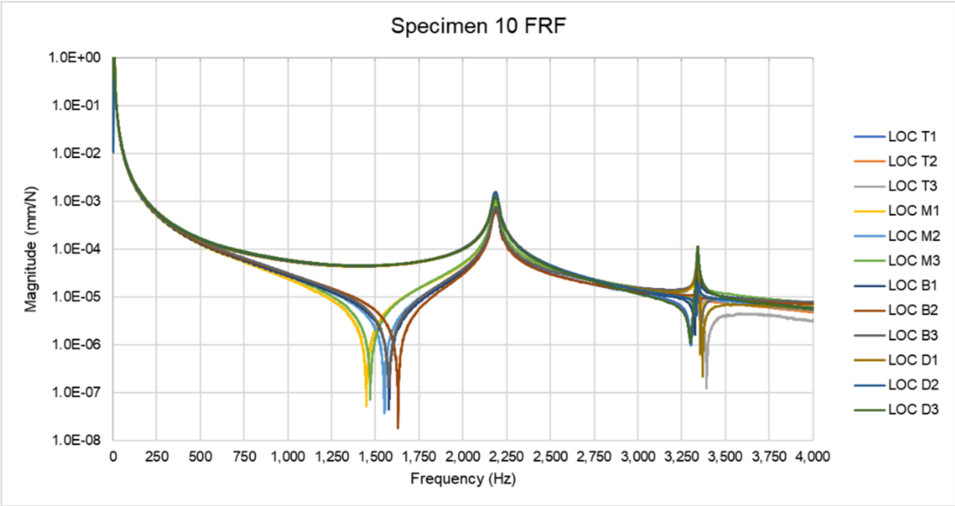

Figure E.12 : 1st DoE Specimen 10 Raw FRF Results.

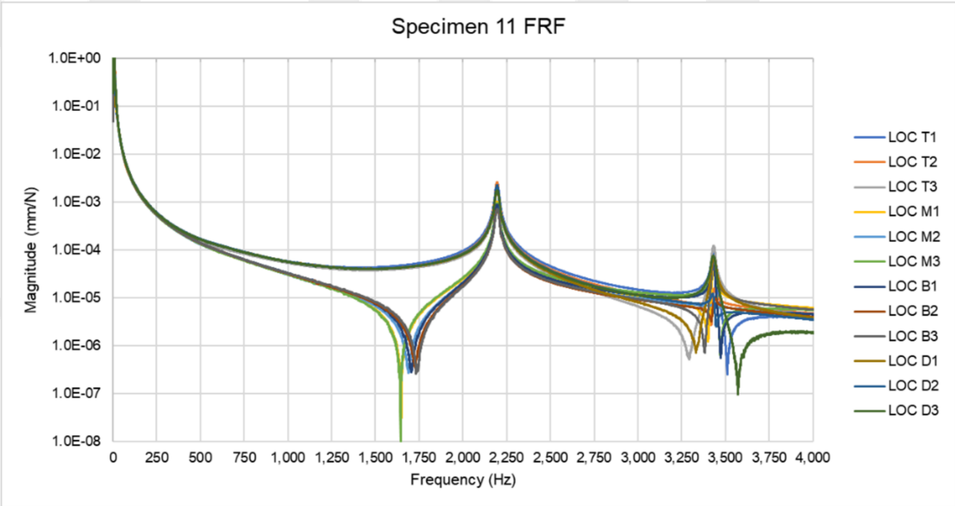

Figure E.13 : 1st DoE Specimen 11 Raw FRF Results.

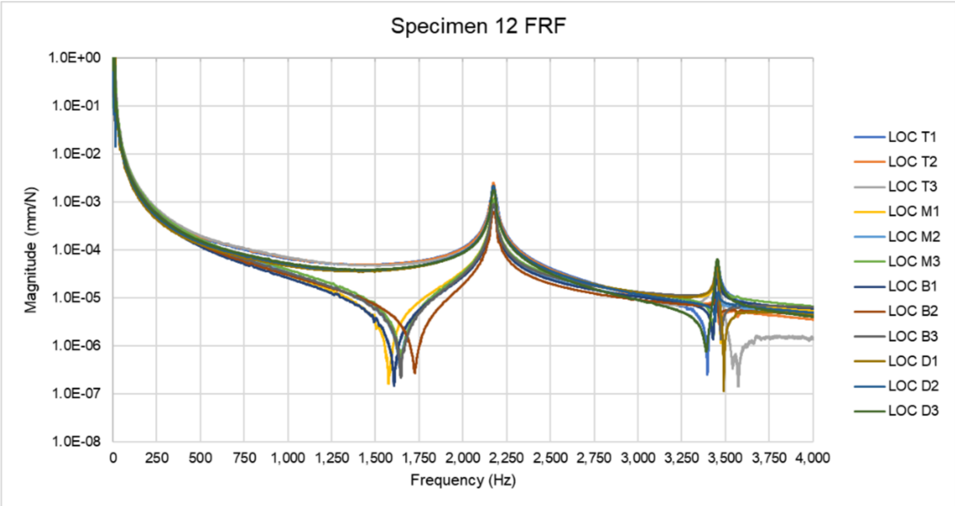

Figure E.14 : 1st DoE Specimen 12 Raw FRF Results.

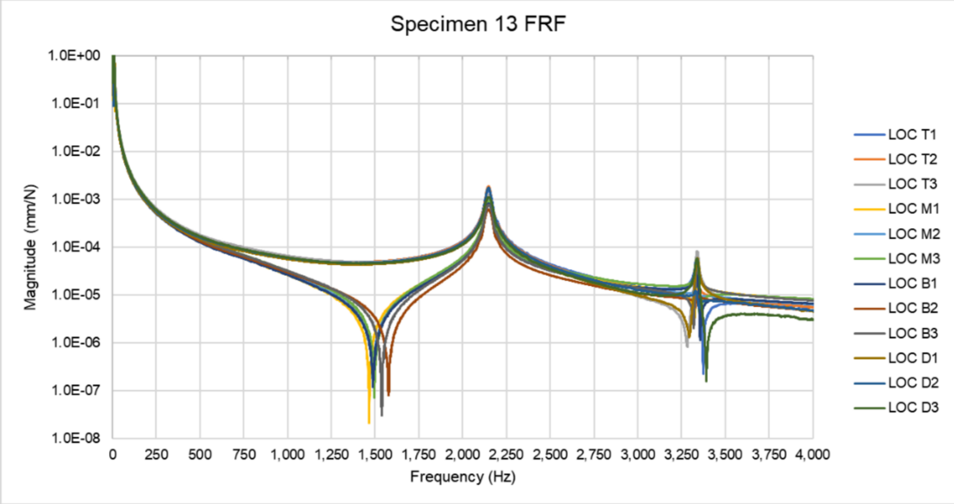

Figure E.15 : 1st DoE Specimen 13 Raw FRF Results.

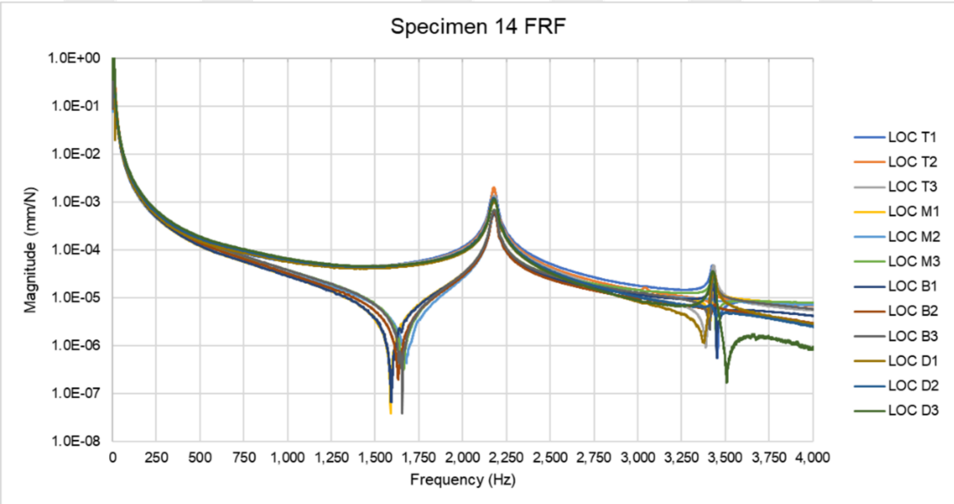

Figure E.16 : 1st DoE Specimen 14 Raw FRF Results.

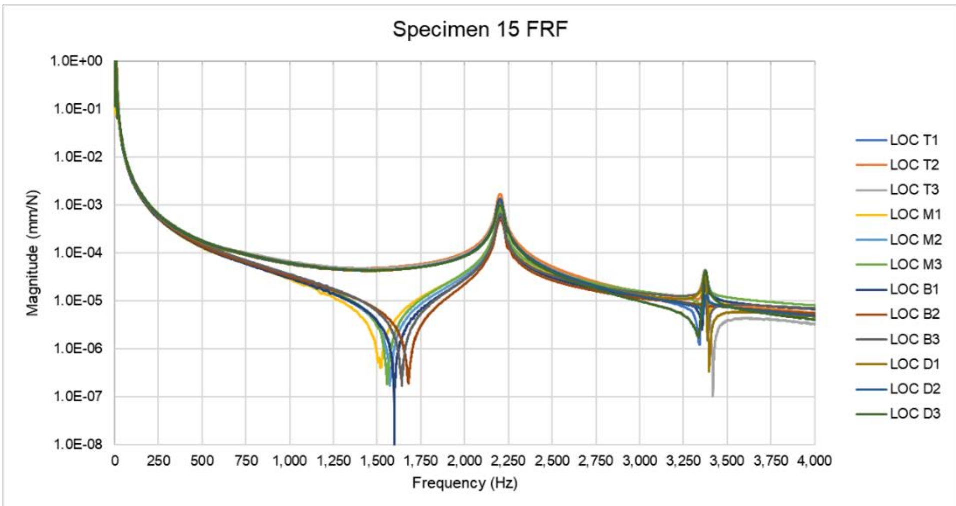

Figure E.17 : 1st DoE Specimen 15 Raw FRF Results.

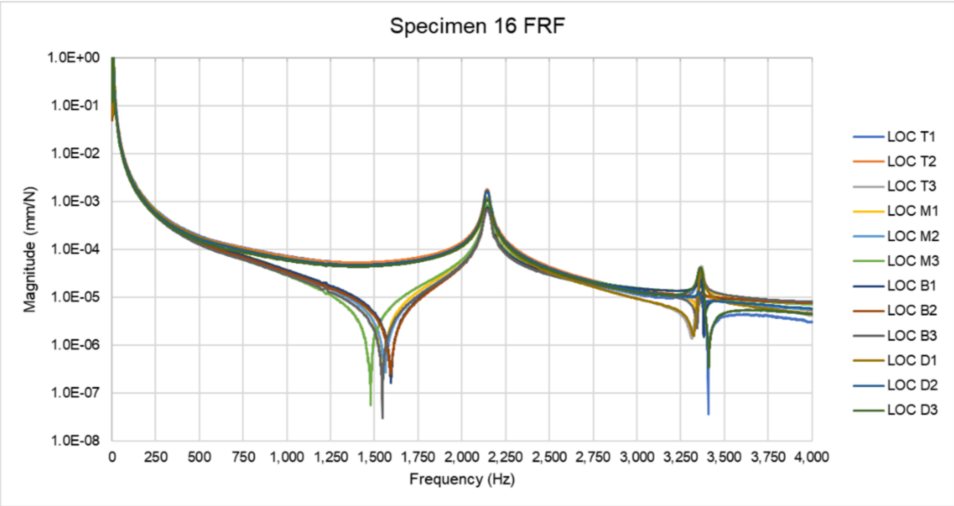

Figure E.18 : 1st DoE Specimen 16 Raw FRF Results.

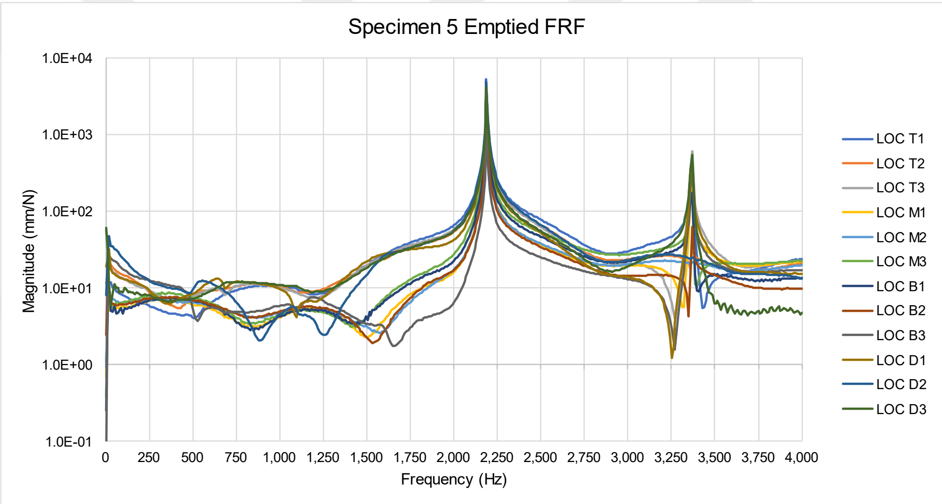

Figure E.19 : 1st DoE Specimen 5 (Emptied) Raw FRF Results.

APPENDIX F: 2nd DoE raw FRF data.

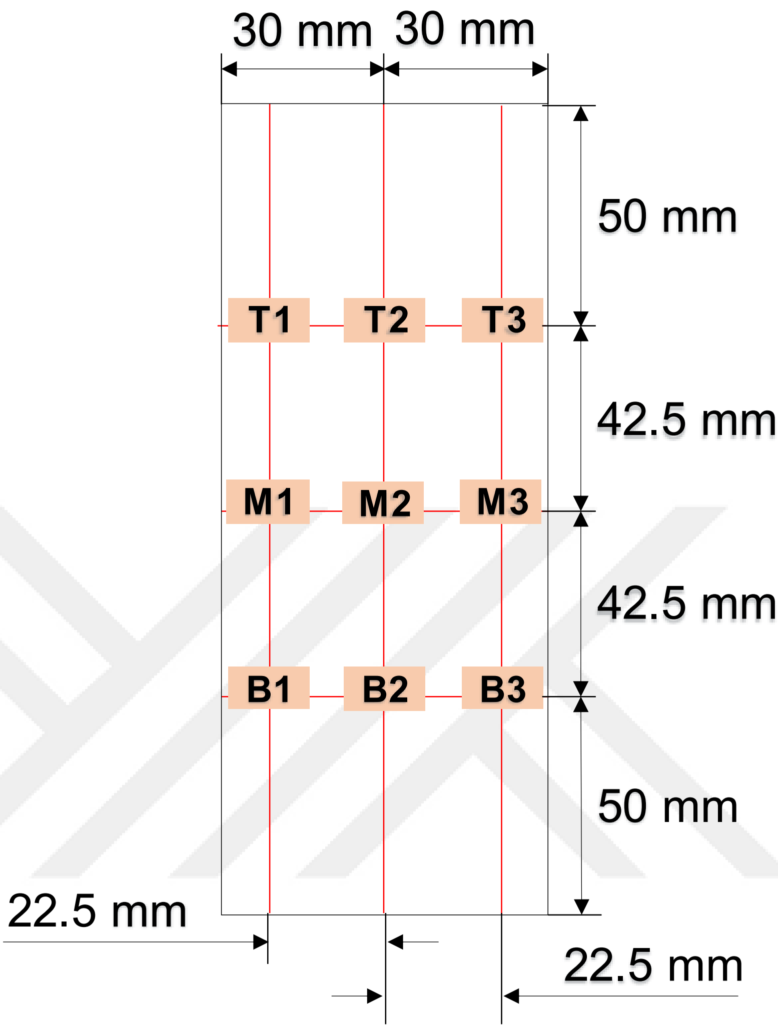

Figure F.1 : 2nd DoE Impact Location Naming.

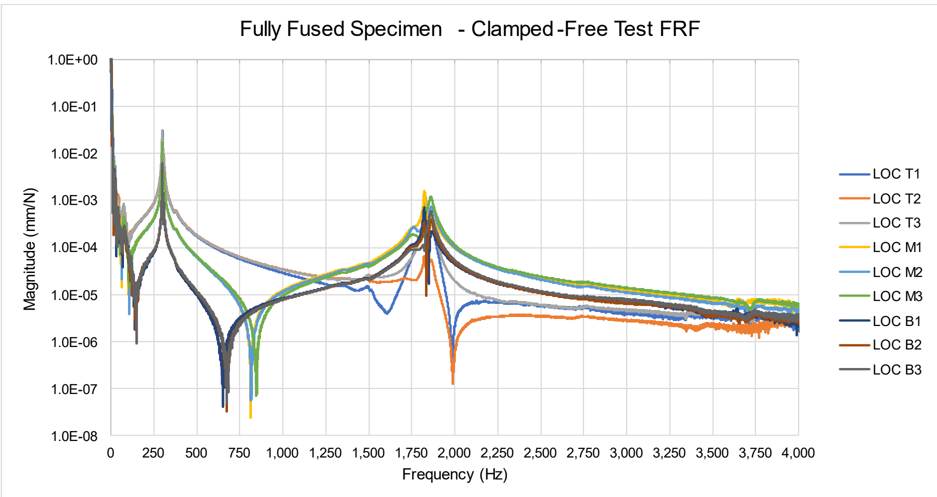

Figure F.2 : 2nd DoE Fully Fused Specimen Clamped-Free Test Raw FRF Results.

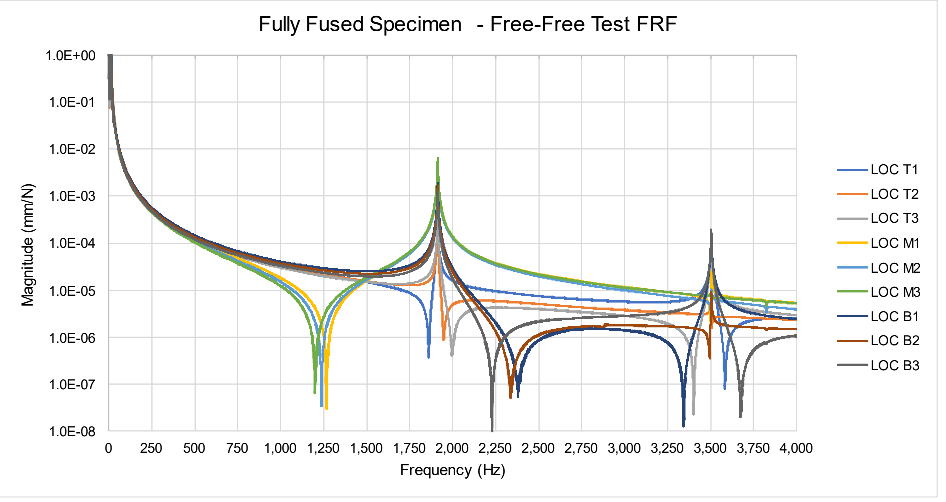

Figure F.3 : 2nd DoE Fully Fused Specimen Free-Free Test Raw FRF Results.

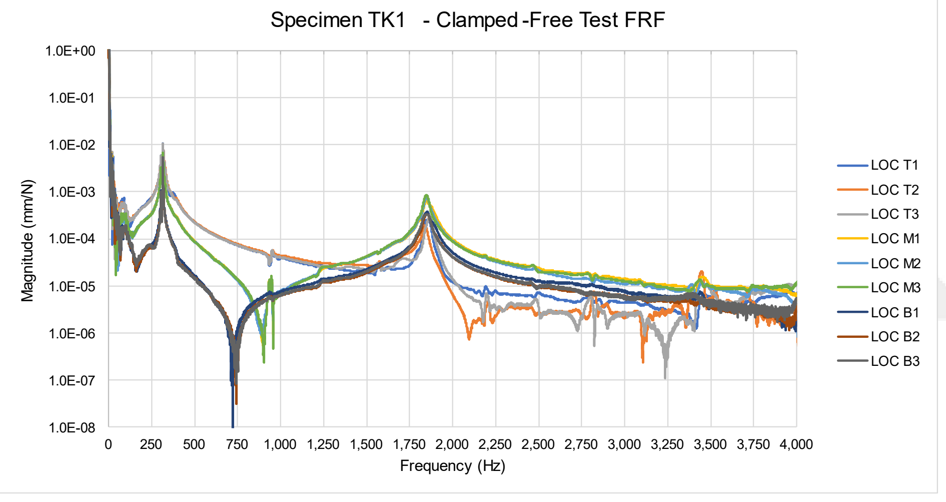

Figure F.4 : 2nd DoE Specimen TK1 Clamped-Free Test Raw FRF Results.

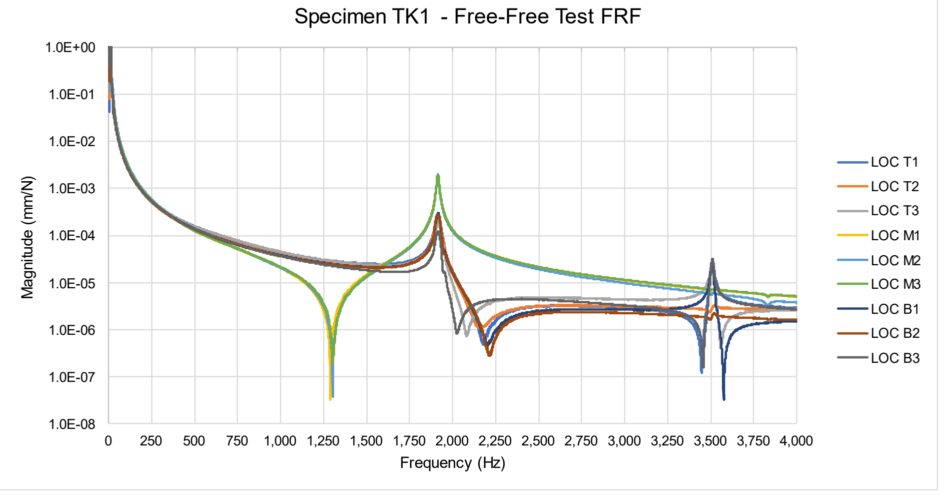

Figure F.5 : 2nd DoE Specimen TK1 Free-Free Test Raw FRF Results.

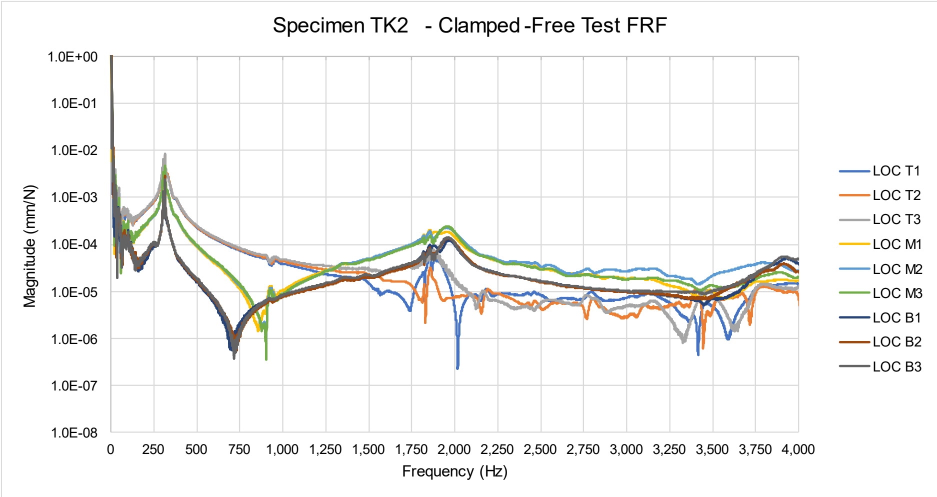

Figure F.6 : 2nd DoE Specimen TK2 Clamped-Free Test Raw FRF Results.

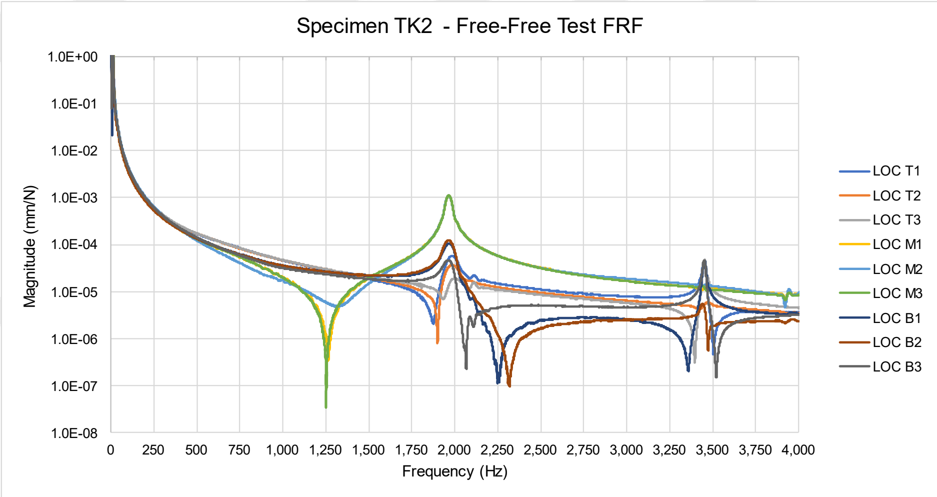

Figure F.7 : 2nd DoE Specimen TK2 Free-Free Test Raw FRF Results.

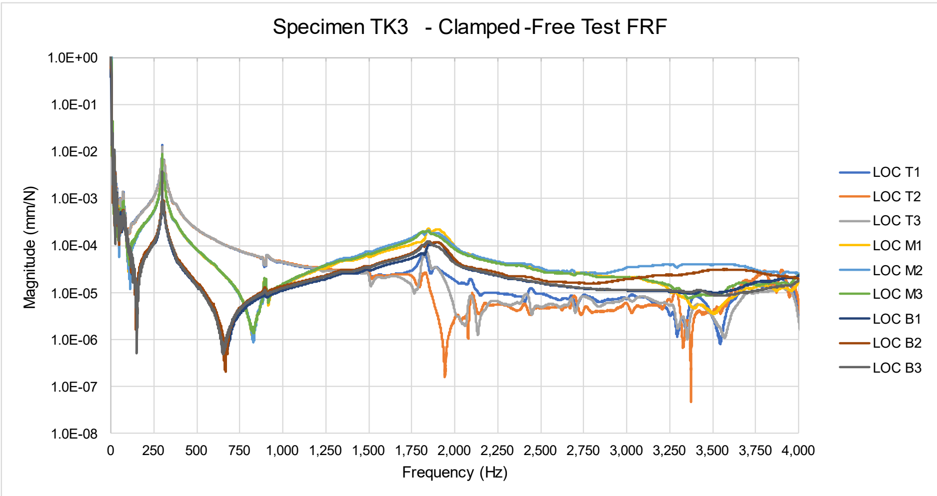

Figure F.8 : 2nd DoE Specimen TK3 Clamped-Free Test Raw FRF Results.

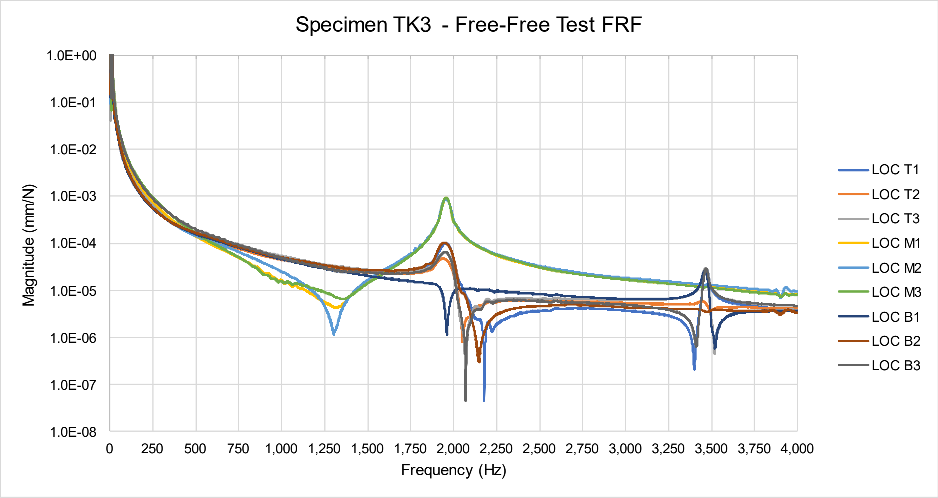

Figure F.9 : 2nd DoE Specimen TK3 Free-Free Test Raw FRF Results.

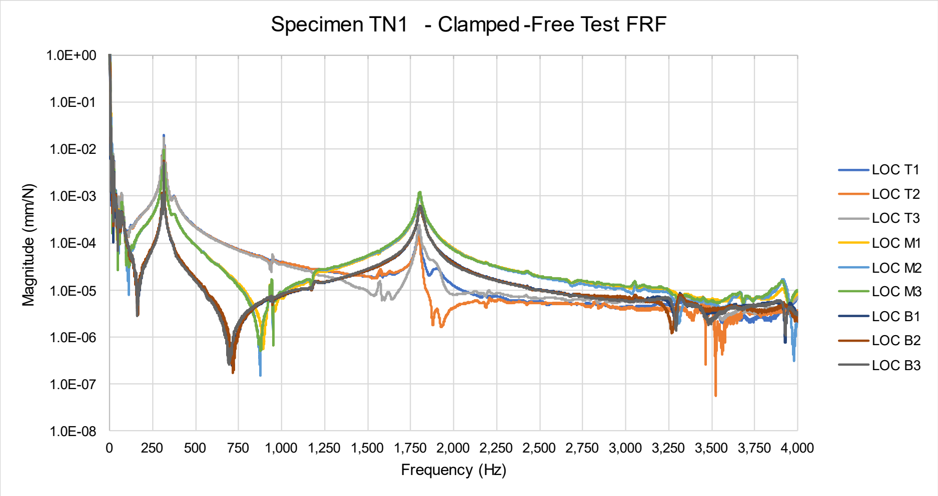

Figure F.10 : 2nd DoE Specimen TN1 Clamped-Free Test Raw FRF Results.

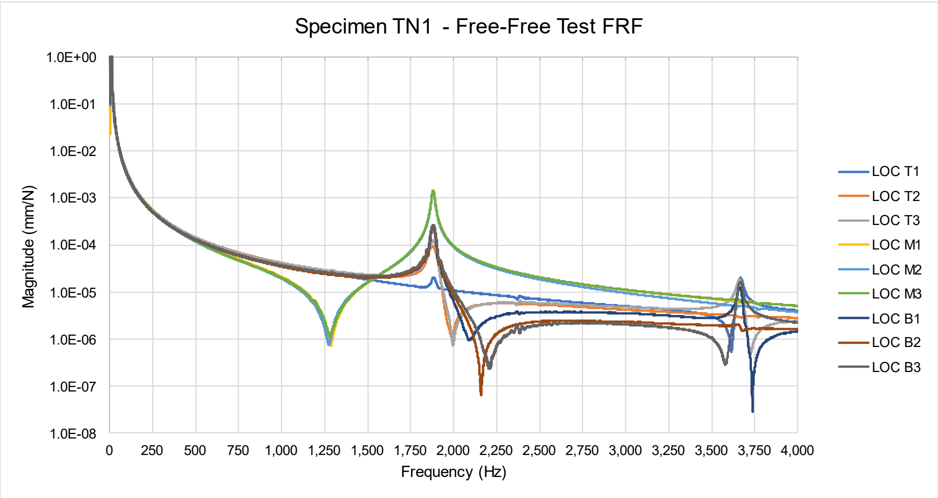

Figure F.11 : 2nd DoE Specimen TN1 Free-Free Test Raw FRF Results.

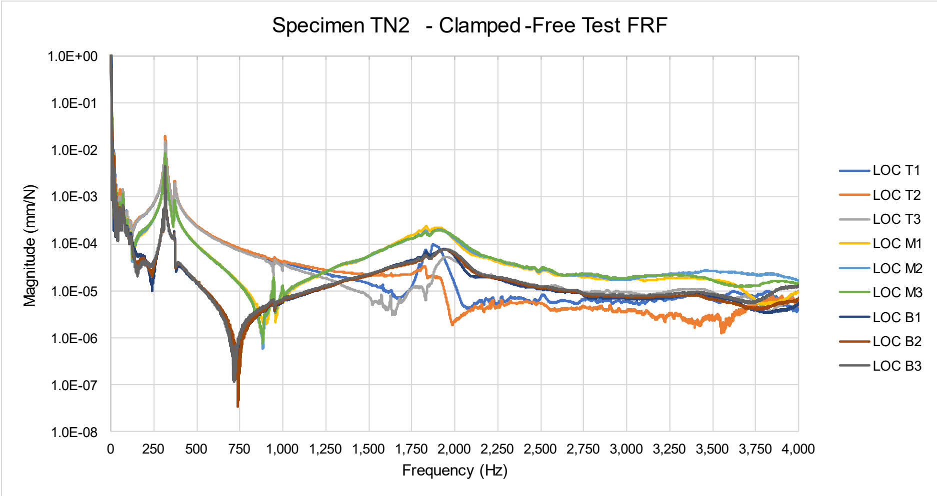

Figure F.12 : 2nd DoE Specimen TN2 Clamped-Free Test Raw FRF Results.

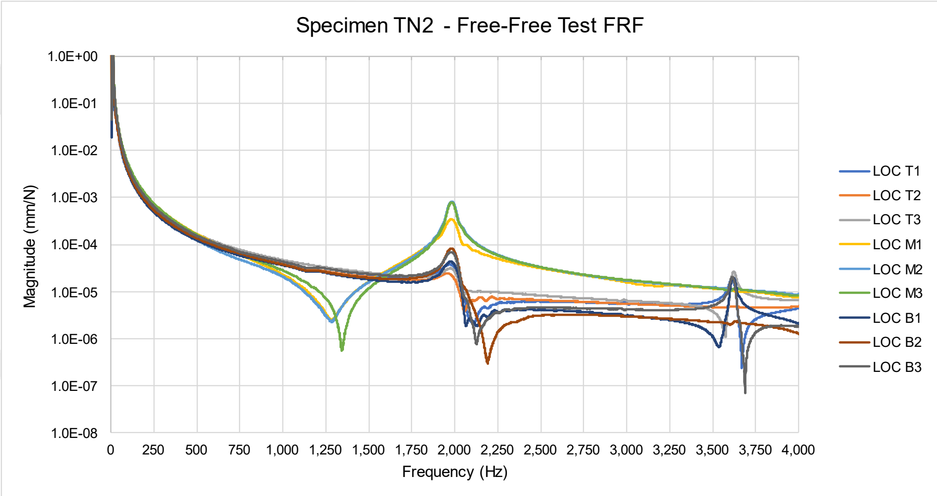

Figure F.13 : 2nd DoE Specimen TN2 Free-Free Test Raw FRF Results.

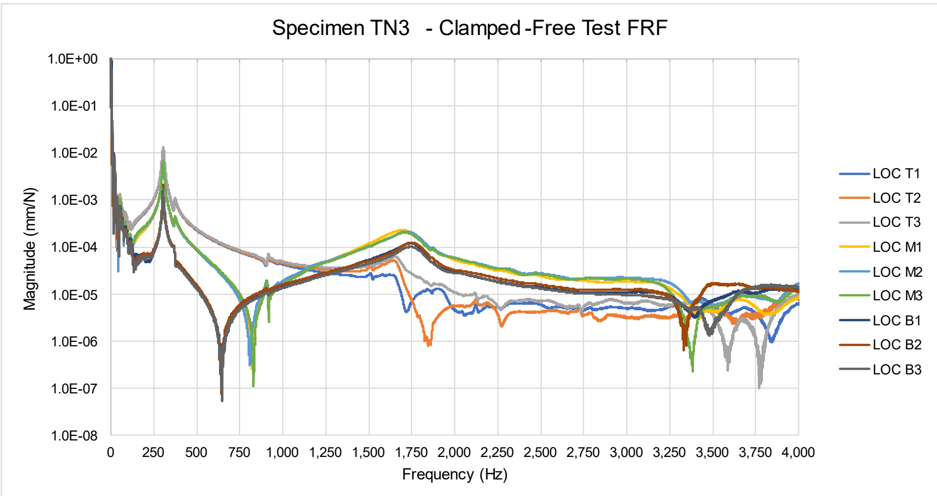

Figure F.14 : 2nd DoE Specimen TN3 Clamped-Free Test Raw FRF Results.

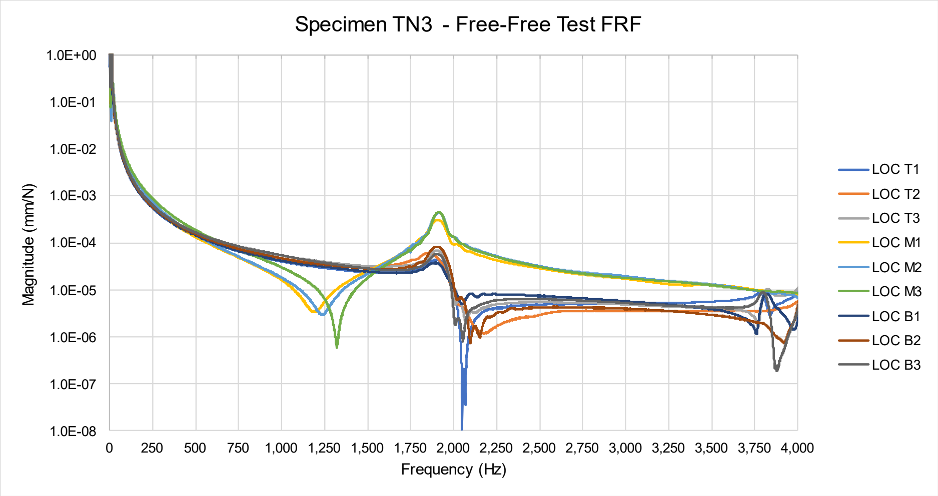

Figure F.15 : 2nd DoE Specimen TN3 Free-Free Test Raw FRF Results.

CURRICULUM VITAE

Name Surname : **Birol ÖZÇEVİK**

EDUCATION :

- **B.Sc.** **:** 2019, Yildiz Technical University, Faculty of Mechanical Engineering, Mechanical Engineering Department

PROFESSIONAL EXPERIENCE AND REWARDS:

- 2019 – Present : GE Aerospace